

REPORT DOCUMENTATION PAGE

AFRL-SR-BL-TR-01-

Public reporting burden for this collection of information is estimated to average 1 hour per response, including gathering and maintaining the data needed, and completing and reviewing the collection of information. Send collection of information, including suggestions for reducing this burden, to Washington Headquarters Service, Paperwork Project, Room 1010, 1215 Jefferson Davis Highway, Suite 1204, Arlington, VA 22202-4302, and to the Office of Management and Budget, Paperwork Project, Room 1010, 1215 Jefferson Davis Highway, Suite 1204, Arlington, VA 22202-4302.

Source,
of this
person

0019

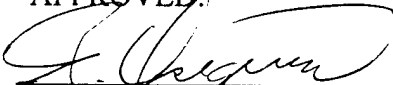
1. AGENCY USE ONLY (Leave blank)		2. REPORT DATE	3. REPORT TYPE AND DATES COVERED 01 October 1997 - 31 August 2000	
4. TITLE AND SUBTITLE Constitutive-Microdamage Modeling of Target-Missile Damage Caused by Hypervelocity Impact			5. FUNDING NUMBERS F49620-97-10356	
6. AUTHOR(S) Professor Eftis				
7. PERFORMING ORGANIZATION NAME(S) AND ADDRESS(ES) University of Texas, El Paso FAST Center for Structural Integrity of Aerospace Systems College of Engineering El Paso, TX 79968-0516			8. PERFORMING ORGANIZATION REPORT NUMBER	
9. SPONSORING/MONITORING AGENCY NAME(S) AND ADDRESS(ES) AFOSR 801 North Randolph Street, Room 732 Arlington, VA 22203-1977			10. SPONSORING/MONITORING AGENCY REPORT NUMBER F49620-97-1-0356	
11. SUPPLEMENTARY NOTES				
12a. DISTRIBUTION AVAILABILITY STATEMENT Approved for Public Release.			<p>DTIC QUALITY INSPECTED 4</p> <p>20010129 007</p>	
13. ABSTRACT (Maximum 200 words) A constitutive microdamage model is developed capable of simulating high shock compression, release, dilatation (tension), and microdamage evolution leading possibly to fracture and penetration of targets after hypervelocity impact. The microdamage constitutive model is applicable to polycrystalline metals and is appropriate in the lower range of hypervelocity impact velocity, i.e. approximately 2-7 Km/s, over which the projectile and target materials remain in the solid state. The model implements the Mie-Gruneisen equation of state coupled with the Hugoniot relations along with expressions of non-linear elastic moduli (bulk and shear) as functions of volume strain, temperature and microdamage. The viscoplastic material response includes strain and strain rate hardening and temperature and microdamage softening. The microdamage evolution model is based on the micromechanics of an expanding void, and is capable of modeling void compaction and expansion that leads to spall-fracture as an evolutionary time dependent process. The constitutive microdamage model was implemented in the Autodyn™ software and a series of computer simulations of hypervelocity impact experiments on Al/Al ₂ O ₃ plates with soda-lime glass spherical projectiles were conducted. The results of the simulations are compared with the laboratory experimental results in terms of crater, penetration hole and back-wall spallation geometry of the target plate.				
14. SUBJECT TERMS			15. NUMBER OF PAGES 136	
			16. PRICE CODE	
17. SECURITY CLASSIFICATION OF REPORT	18. SECURITY CLASSIFICATION OF THIS PAGE	19. SECURITY CLASSIFICATION OF ABSTRACT	20. LIMITATION OF ABSTRACT	

DEVELOPMENT OF A CONSTITUTIVE MICRODAMAGE MODEL FOR
SIMULATION OF DAMAGE AND FRACTURE OF METALLIC PLATES
CAUSED BY HYPERVELOCITY IMPACT

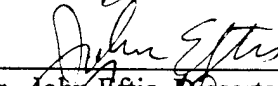
CESAR J. CARRASCO TREJO

Materials Research Institute

APPROVED:



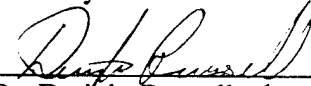
Dr. Roberto Osegueda, Chair



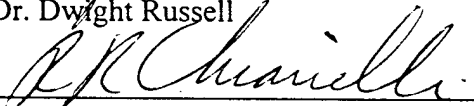
Dr. John Eftis, Dissertation director



Dr. Roy M. Arrowood



Dr. Dwight Russell



Dr. Russell R. Chianelli

Associate Vice President
For Graduate Studies

**This Dissertation is dedicated to *Rebeca Carrasco* and
Joel A. Carrasco my beloved daughter and son.**

**My hope is that this work may some day serve as
inspiration for you to study and learn, and surpass me
in what I have accomplished.**

**DEVELOPMENT OF A CONSTITUTIVE MICRODAMAGE MODEL FOR
SIMULATION OF DAMAGE AND FRACTURE OF METALLIC PLATES
CAUSED BY HYPERVELOCITY IMPACT**

by

Cesar J. Carrasco Trejo, B.Sc., M.Sc.

DISSERTATION

Presented to the Faculty of the Graduate School of

The University of Texas at El Paso

In partial Fulfillment

of the Requirements for the Degree of

DOCTOR OF PHILOSOPHY

In Materials Science and Engineering

Materials Research Institute

THE UNIVERSITY OF TEXAS AT ELPASO

July 2000

ACKNOWLEDGEMENTS

This dissertation was directed by Dr. John Eftis, D.Sci. Emeritus Professor of Engineering and Applied Science at The George Washington University, Washington, D.C. Without his support, interest in teaching and tutoring, it would have been impossible to accomplish the work presented in this dissertation.

I wish to thank Dr. Roberto Osegueda for his support and encouragement during the course of my graduate studies.

Special appreciation is expressed to the FAST Center for Structural Integrity of Aerospace Systems sponsored by the U.S. Air Force Office of Scientific Research (Grant No. F49620-95-0518) and to NASA JSC (Grant No. NAG9-1099) for the financial support provided during my doctoral studies.

I would also like to thank the other members of the dissertation committee, Dr. Roy M. Arrowood, Dr. Dwight Russell and Dr. Russell R. Chianelli, for reviewing this dissertation and their commentaries and suggestions.

The technical assistance from Bence Gerber and Malcolm S. Cowler from Century Dynamics is greatly appreciated.

I would also like to thank my parents, Ariel Carrasco and Socorro Trejo, for their support and for being a source of inspiration for me to study and learn. Also, I wish to thank my brothers and sisters specially my brother Ariel Carrasco for all his support and help.

Finally, I would like to express my deepest and special gratitude to my wife for her unconditional support and encouragement throughout all the years of my graduate studies. Thank you Blanca.

This research was sponsored by the Ballistic Missile Defense Organization, administered by the U.S. Air Force Office of Scientific Research, Small Business Administration, Grant No. F49620-97-1-0536. Special appreciation to Dr. Arje Nachman and Dr. Pohlman of AFOSR, for all their help and encouragement.

Cesar J. Carrasco Trejo

This dissertation was submitted to the reviewing committee on June 6, 2000.

ABSTRACT

A constitutive microdamage model is developed capable of simulating high shock compression, release, dilatation (tension), and microdamage evolution leading possibly to fracture and penetration of targets after hypervelocity impact. The microdamage constitutive model is applicable to polycrystalline metals and is appropriate in the lower range of hypervelocity impact velocity, i.e. approximately 2-7 Km/s, over which the projectile and target materials remain in the solid state. The model implements the Mie-Gruneisen equation of state coupled with the Hugoniot relations along with expressions of non-linear elastic moduli (bulk and shear) as functions of volume strain, temperature and microdamage. The viscoplastic material response includes strain and strain rate hardening and temperature and microdamage softening. The microdamage evolution model is based on the micromechanics of an expanding void, and is capable of modeling void compaction and expansion that leads to spall-fracture as an evolutionary time dependent process. The constitutive microdamage model was implemented in the Autodyn™ software and a series of computer simulations of hypervelocity impact experiments on Al₁₁₀₀ plates with soda-lime glass spherical projectiles were conducted. The results of the simulations are compared with the laboratory experimental results in terms of crater, penetration hole and back-wall spallation geometry of the target plate.

STATEMENT OF PROBLEM

The importance of a reliable constitutive model to describe the deformation process and the eventual material degradation and fracture after hypervelocity impact has become of primary interest in the last decade. The deployment of low earth orbit satellites capable of surviving high velocity impacts by micro-meteoroids and small orbital space debris has been and continues to be the subject of extensive research. In addition, the eventual construction of the International Space Station will put to test the extensive experimental and theoretical research being developed in the area of hypervelocity impact phenomena. Furthermore, the importance of this area of research is not limited to the aerospace industry. The US Defense Department has always recognized the relevance of an in-depth understanding of the armor penetration process to aid in the design of armor structures and armor penetration devices.

In recent years there have been significant research efforts directed towards the development of constitutive models that simulate crater formation, spall fracture and penetration as a result of a hypervelocity impact. Many of these models have been implemented and built into several public domain and commercial software packages that are available today (Steinberg *et al.* 1980 and 1989, Johnson *et al.* 1983, Zerilli *et al.* 1987). However, these constitutive models have known limitations. The most important limitation has to do with the modeling of the dynamic failure process where, in most cases, fracture is assumed to take place instantaneously without prior accumulation of material micro-degradation. The development of more sophisticated constitutive models

that can describe failure is crucial for the problem of modeling the physical processes associated with hypervelocity impact events, especially in relation to the design of armor, armor penetrators, debris-shield design and other applications where the lethality of the impact is a design-controlling factor (e.g., hypervelocity impact destruction of incoming ballistic warhead).

It is the goal of this dissertation to develop a constitutive-microdamage model that can describe the thermo-mechanical deformation associated with high shock compression, release, dilatation and shear, and the progressive microdamage that leads to fracture of ductile polycrystalline materials.

TABLE OF CONTENTS

ACKNOWLEDGEMENTS	iv
ABSTRACT.....	vi
STATEMENT OF PROBLEM.....	vii
TABLE OF CONTENTS	ix
LIST OF TABLES	xi
LIST OF FIGURES	xii
CHAPTER 1. INTRODUCTION.....	1
1.1 Background.....	3
1.1.1 Constitutive Models.....	3
1.1.2 Fracture Models	6
1.1.3 Computer Codes.....	15
1.1.4 Microstructural Studies.....	16
1.2 Objective.....	18
CHAPTER 2. RANKINE-HUGONOT EQUATIONS.....	21
CHAPTER 3. GRUNEISEN EQUATION OF STATE	27
CHAPTER 4. CONSTITUTIVE-MICRODAMAGE MODEL.....	33
4.1 Introduction.....	33
4.2 Elastic Rate of Deformation.....	34
4.3 Viscoplastic Rate of Deformation.....	40
4.4 Microdamage Evolution.....	44
4.4.1 Microvoid Nucleation Rate.....	47
4.4.2 Microvoid Growth Rate	49
4.4.3 Estimate of the Temperature at the Microvoid Wall	59
4.5 Equations for Internal Energy and Temperature Rates.....	61
CHAPTER 5. NUMERICAL IMPLEMENTATION OF THE CONSTITUTIVE MODEL	63

5.1	Numerical Simplifications	65
5.1.1	Modifications to the Viscoplastic Constitutive Model	65
5.1.2	Modifications to the Void Growth Model	67
5.1.3	Modifications to the Temperature Rate Equation	68
CHAPTER 6.	NUMERICAL SIMULATIONS OF HYPERVELOCITY	
	IMPACT	70
6.1	Shock Pressure and Temperature Calculation	70
6.2	Hypervelocity Impact of Soda-Lime Glass Projectiles on Al ₁₁₀₀ Target Plates	72
6.2.1	Computer Simulations Description	74
6.2.2	Simulation Results	78
CHAPTER 7	CONCLUSIONS AND RECOMMENDATIONS.....	101
7.1	Introduction.....	101
7.2	Summary	101
7.3	Conclusions.....	103
7.4	Recommendations.....	104
REFERENCES.....		107
CURRICULUM VITAE.....		119

LIST OF TABLES

Table 6.1	Dimensional characteristics of hypervelocity impact cases.....	74
Table 6.2	Material parameters for Al ₁₁₀₀	77

LIST OF FIGURES

Figure 2.1	High-pressure Hugoniot data for Copper obtained by several investigators. The numerals along the curve indicate pressures in GPa. The line on the small inset represents the entire range of the larger figure, while the three points represent the results of Soviet ultrahigh pressure experiments (Davison <i>et al.</i> 1979).....	22
Figure 2.2	Depiction of the state of the material ahead and behind the Shock-Front.....	23
Figure 2.3	Shock Hugoniot pressure curve and Rayleigh line for a given pressure P_1	26
Figure 3.1	Mie-Gruneisen, Hugoniot, 0°K and 300°K Isothermal Pressure-Volume Strain Curves.....	31
Figure 4.1	Viscosity as a function of temperature for Aluminum ($\eta_0=10^4$ P, $\eta_m=10^{-2}$ P and $T_m=923$ °K).....	43
Figure 4.2	Ductile cracks. (a) Ductile crack propagation by void coalescence; (b) Tip of ductile crack shown in (a) at higher magnification (Curran <i>et al.</i> 1987).....	46
Figure 4.3	Fracture surface of ETP Copper (Zurek <i>et al.</i> 1996).	47
Figure 4.4	Element of the solid with microvoids replaced by idealized spherical voids.....	49
Figure 4.5	Idealized spherical void with average mean stress.	51
Figure 6.1	Calculated and experimental (open circles) pressure versus volume strain curves for Copper.....	71
Figure 6.2	Calculations of temperature versus shock pressure using thermal energy rate balance (solid line) and classical thermodynamics (circles).....	72
Figure 6.3	Cratering and penetration events in Al ₁₁₀₀ targets of three different thickness (a=12.5 mm, b=7.61 mm and c=1.59 mm) using 3.175 mm diameter soda-lime glass projectiles at 6 km/s (Horz <i>et al.</i> 1995).....	73

Figure 6.4	Grid configuration for simulation (a) corresponding to a target plate thickness of 12.5mm.	75
Figure 6.5	Grid configuration for simulation (b) corresponding to a target plate thickness of 7.61mm.	75
Figure 6.6	Grid configuration for simulation (c) corresponding to a target plate thickness of 1.59mm.	76
Figure 6.7	Microfailure features observed on a section taken through a steel plate and embedded steel rod after impact (Shockey <i>et al.</i> 1979).	82
Figure 6.8(1)	Pressure contour plots for 12.5mm thick Al ₁₁₀₀ target plate at 0 μ s, 0.5 μ s, 1.0 μ s, 1.5 μ s (a, b, c, d respectively) after impact.	83
Figure 6.8(2)	Pressure contour plots for 12.5mm thick Al ₁₁₀₀ target plate at 2 μ s, 2.5 μ s, 5 μ s and 20 μ s (e, f, g, h respectively) after impact.	84
Figure 6.9(1)	Temperature contour plots for 12.5mm thick Al ₁₁₀₀ target plate at 0 μ s, 0.5 μ s, 1.0 μ s, 1.5 μ s (a, b, c, d respectively) after impact.	85
Figure 6.9(2)	Temperature contour plots for 12.5mm thick Al ₁₁₀₀ target plate at 2 μ s, 2.5 μ s, 5 μ s and 20 μ s (e, f, g, h respectively) after impact.	86
Figure 6.10(1)	Void-volume fraction contour plots for 12.5mm thick Al ₁₁₀₀ target plate at 0 μ s, 0.5 μ s, 1.0 μ s, 1.5 μ s (a, b, c, d respectively) after impact.	87
Figure 6.10(2)	Void-volume fraction contour plots for 12.5mm thick Al ₁₁₀₀ target plate at 2 μ s, 2.5 μ s, 5 μ s and 20 μ s (e, f, g, h respectively) after impact.	88
Figure 6.11(1)	Pressure contour plots for 7.61mm thick Al ₁₁₀₀ target plate at 0 μ s, 0.5 μ s, 1.0 μ s, 1.5 μ s (a, b, c, d respectively) after impact.	89
Figure 6.11(2)	Pressure contour plots for 7.61mm thick Al ₁₁₀₀ target plate at 2 μ s, 2.5 μ s, 5 μ s and 20 μ s (e, f, g, h respectively) after impact.	90
Figure 6.12(1)	Temperature contour plots for 7.61mm thick Al ₁₁₀₀ target plate at 0 μ s, 0.5 μ s, 1.0 μ s, 1.5 μ s (a, b, c, d respectively) after impact.	91
Figure 6.12(2)	Temperature contour plots for 7.61mm thick Al ₁₁₀₀ target plate at 2 μ s, 2.5 μ s, 5 μ s and 20 μ s (e, f, g, h respectively) after impact.	92

Figure 6.13(1)	Void-volume fraction contour plots for 7.61mm thick Al ₁₁₀₀ target plate at 0 μ s, 0.5 μ s, 1.0 μ s, 1.5 μ s (a, b, c, d respectively) after impact.	93
Figure 6.13(2)	Void-volume fraction contour plots for 7.61mm thick Al ₁₁₀₀ target plate at 2 μ s, 2.5 μ s, 5 μ s and 20 μ s (e, f, g, h respectively) after impact.	94
Figure 6.14(1)	Pressure contour plots for 1.59mm thick Al ₁₁₀₀ target plate at 0 μ s, 0.5 μ s, 1.0 μ s, 1.5 μ s (a, b, c, d respectively) after impact.	95
Figure 6.14(2)	Pressure contour plots for 1.59mm thick Al ₁₁₀₀ target plate at 2 μ s, 2.5 μ s, 5 μ s and 20 μ s (e, f, g, h respectively) after impact.	96
Figure 6.15(1)	Temperature contour plots for 1.59mm thick Al ₁₁₀₀ target plate at 0 μ s, 0.5 μ s, 1.0 μ s, 1.5 μ s (a, b, c, d respectively) after impact.	97
Figure 6.15(2)	Temperature contour plots for 1.59mm thick Al ₁₁₀₀ target plate at 2 μ s, 2.5 μ s, 5 μ s and 20 μ s (e, f, g, h respectively) after impact.	98
Figure 6.16(1)	Void-volume fraction contour plots for 1.59mm thick Al ₁₁₀₀ target plate at 0 μ s, 0.5 μ s, 1.0 μ s, 1.5 μ s (a, b, c, d respectively) after impact.	99
Figure 6.16(2)	Void-volume fraction contour plots for 1.59mm thick Al ₁₁₀₀ target plate at 2 μ s, 2.5 μ s, 5 μ s and 20 μ s (e, f, g, h respectively) after impact.	100

CHAPTER 1

INTRODUCTION

The physical features of projectile-target collisions at very high velocities are varied and depend upon the interplay of major controlling geometric and physical parameters such as the velocity of impact, the relative dimensions of the target thickness and the projectile diameter, and the material properties of the target and the projectile. There are many damage scenarios that can be identified, ranging from target crater formation to target perforation, where for the latter situation at very high projectile velocities it is possible to have target and projectile fragmentation and debris cloud formation, while for still higher velocities melting and vaporization of portions of the projectile and target materials are also possible (Anderson *et al.* 1993, Horz *et al.* 1995).

Spherical projectiles traveling at velocities varying from 2 to 7 km/s can, upon impact, produce spherical shock waves of compression and shear with pressures ranging from 10-150 GPa, that propagate into both the target and projectile at very high strain rates of the order of 10^6 - 10^8 s⁻¹. Transmission electron microscopy has shown evidence of varied arrays of deformation-induced defects and, in some cases, dynamic recrystallization immediately below the impact surface of several metallic targets at the higher end of the impact velocity range, indicating substantial temperature increases in both the target and projectile (Rivas *et al.* 1995, Quiñones *et al.* 1998). The transit time of the wave propagation and thermomechanical material response across the target thickness is of the order a couple of microseconds (μ s), implying essentially adiabatic

deformation. Because of thermomechanical coupling associated with the substantial dilatational and shear deformations, the highly deformed thermally softened region beneath the contact surface of the target provides the displaced material that forms the surface crater ring and ejecta. For the target material below the crater, a competing effect develops between the strain hardening and thermal softening effects as evidenced by the measured vickers microhardness profiles (Quiñones *et al.* 1998). Further across the target thickness, the attenuated shock wave produces a reflected tensile wave traveling back from the rear surface of the target. If the tensile mean stress reaches a threshold value the growth and/or nucleation of voids can begin, producing mechanical softening of the material and possibly coalescence of voids leading to fracture (Curran *et al.* 1987).

The development of computer codes capable of predicting the deformation and damage processes produced by hypervelocity impact have evolved from being very rudimentary in the 50's and 60's, to very sophisticated at this time. One of the initial limitations of these codes was the absence of shear deformation considerations in the simulation algorithms. The development of more sophisticated instrumentation for the experimental characterization of the deformation process under shock loading (Meyers 1994) has improved our understanding of the hypervelocity impact problem, and with the advent of high speed computers that use more sophisticated material models and numerical algorithms, the applicability of the computer codes has been extended. Now, computer simulations of high-rate deformation processes are being used in industry as well as in military and aerospace applications as part of the design process. Unfortunately, one of the limitations that still lingers in high shock compression

computer codes is the poor constitutive modeling of the dynamic fracture process, where it is often assumed that fracture occurs instantaneously without prior evolution of the material degradation.

1.1 Background

The following is a brief discussion of the research articles that form the base for the research work presented in this dissertation. The literature review is presented in chronological order.

1.1.1 Constitutive Models

The articles discussed in this section deal specifically with two topics: pressure-volume relations and yield models (in the Von Mises sense) of polycrystalline metals. The pressure-volume relations discussed are for pressures up to 10 TPa. The dynamic yield models varied in complexity from perfectly plastic rate-independent to viscoplastic with strain hardening and thermal softening.

Walsh *et al.* (1957) presented an extensive compilation of material parameters that describe the Hugoniot curves, Mie-Gruneisen pressure volume relations and the volume strain dependence of the Gruneisen coefficient for shock pressures of up to 400 kbars (40GPa).

Kratochvil *et al.* (1969,1970) proposed an elastic-viscoplastic constitutive model that described strain and strain rate hardening as thermodynamic functions that described the movement and interaction of microstructural defects.

Davison *et al.* (1979) presented a very thorough exposition of the then status of investigations concerning the response of solids to shock compression. They described the mechanical and structural behavior of materials under shock loading beginning with the elastic response, the pressure-volume relations, hydrodynamic approximation to the response of solids, plastic response and finally spall fracture. They also described the electrical, magnetic and optical properties of solids under shock loading.

Steinberg *et al.* (1980) proposed a constitutive model applicable at high strain rates. The constitutive equation models viscoplastic deformation including descriptions of the shear modulus and yield stress that incorporate dependence on pressure, temperature and plastic strain. However, they restricted the model to high strain rate ($>10^5\text{s}^{-1}$) deformation by assuming a rate independent model. Steinberg *et al.* (1988) developed an addition to the Steinberg-Guinan model to extend its validity to plastic strain rates as low as 10^{-4}s^{-1} .

Godwal *et al.* (1983) presented a review of pressure-volume relation of condensed matter at up to 10 TPa. They described many pressure-volume relations for a wide range of densities and temperatures, obtained by empirical and quantum mechanical calculations, where a variety of physical phenomena such as lattice and electronic thermal excitation, phase transition, etc. are encountered.

Johnson *et al.* (1983) developed an empirical yield model for metals under high strain, high strain rate and high temperature. They also presented a database of material parameters fitted to their model based on torsion, Hopkinson bar and quasi-static tensile experiments. This model, known as the Johnson-Cook model, is widely used in high-

shock computer codes. Rule *et al.* (1998) presented a modification to the Johnson-Cook model to account for the sudden jump in magnitude of the strain rate effect that many metals exhibit at rates greater than 10^4s^{-1} . Follansbee *et al.* (1988) concluded that the increased strain rate sensitivity was due to a dramatic increase in dislocation accumulation at strain rates exceeding $\sim 10^3\text{s}^{-1}$, and proposed a model that used the dislocation density as the only state variable to describe the plastic behavior of f.c.c. (Face center cubic) metals.

Doraivelu *et al.* (1984) proposed a yield function model for porous materials. In their model the yield function was explicitly coupled to the first and second invariants of the stress tensor.

Asay *et al.* (1987) presented a very brief discussion of the basic theoretical concepts that form the basis for the development of material models. They also discussed some experimental techniques used in the characterization of the shock response of materials and a basic discussion of the pressure-volume response of materials in the solid, liquid and gaseous states. Finally they gave a very basic discussion of the viscoplastic behavior of materials and some fracture considerations.

Zerilli *et al.* (1987) presented a viscoplastic constitutive model that is based on dislocation mechanics. Their model applies to fcc polycrystalline metals and incorporates the effects of thermally activated mechanisms of dislocation movement and the influence of solute and grain size. They also presented material parameters for OFHC Copper and Armco Iron based on the data presented by Johnson *et al.* (1983).

Wang *et al.* (1997) presented a study of the applicability of three viscoplastic

models to the modeling of instabilities due to strain and strain rate softening. They considered the Perzyna, Duvaut-Lions models and a new model proposed by them. They also presented a finite difference formulation of the models for inclusion in an implicit or explicit finite element code.

Fossum (1998) presented an optimization technique to fit experimental data to a viscoplastic constitutive model. The proposed method considered the rate form of the constitutive model to be fitted to time-differentiated stress-strain data. He concluded that there is a definite advantage in using the time-differentiated stress-strain data to fit the model since this form of data tends to reduce the correlation between the parameters that define the model.

Zhou *et al.* (1998) proposed a model to account for the softening effect on the yield stress produced by dynamic recovery and heat generation. Their viscoplastic model consisted of a hyperbolic-sine strain hardening law with saturation and a softening term that accounted for the thermally activated effects of dislocation motion. The model was validated with torsional tests under a range of temperatures

1.1.2 Fracture Models

The papers discussed in this section deal with the modeling of dynamic fracture. Most of the articles deal with ductile fracture in the form of void nucleation and growth, but there are some review papers that deal with the dynamic fracture problem in general, including brittle fracture. The first research papers that are discussed do not deal with fracture but with the deformation of porous solids. The reason for presenting a

discussion of these papers in this section is that they form the basis for the latter development of void growth models in fracture micro-mechanics.

Mackenzie (1949) presented a model to calculate the effective bulk and shear modulus of a solid containing spherical holes, i.e. material micro-damage. The effective elastic moduli were calculated by applying a stress to the outer spherical boundary of a sphere with a spherical void and comparing the strains produced in the actual solid with the strains produced by the same stress in a homogeneous isotropic voidless solid.

McClintock (1968) presented a simple fracture criterion for metals driven by the growth of existing holes in the material. His model was based on the growth of cylindrical holes of elliptical cross section with axes parallel to the principal directions of the applied stress.

Herrmann (1969) proposed a constitutive model to describe the compaction of a porous solid under shock loading. The theory behind the model was phenomenological and the functions that define the model had to be fitted to empirical data. He made a series of simplifications, including the assumption that there is no plastic shear deformation and that the compaction process is insensitive to changes in temperature deviations from the Hugoniot. The model compared well with experimental data obtained from plate impact experiments.

Carroll *et al.* (1972) derived pore collapse relations by analysis of a hollow sphere under an external pressure, with a pressure-volume relation of the porous material similar to the one proposed by Herrmann (1969). They did a study of the initial elastic-void-volume change, the transition to an elastic-plastic phase and the final plastic phase. They

concluded that the first two phases do not have a big effect on the compressibility of the porous material. The plasticity model was simplified to an elastic-perfectly-plastic material without rate effects, and thermal effects were neglected.

Butcher *et al.* (1974) presented some improvements to the original model proposed by Carrol *et al.* (1972). The improvements included the addition of work hardening and rate dependence through a viscosity term. The predictions of this improved model were compared with experimental data on 2024 Aluminum with good agreement.

Shima *et al.* (1976) proposed a yield criterion for porous materials that coupled the onset of yield of the matrix material due to deviatoric stresses and the onset of yield on the pore wall.

Seaman *et al.* (1976) developed models of ductile and brittle fracture. The models included the nucleation and growth of voids or cracks and the coalescence of cracks. The nucleation and growth models were phenomenological and included a threshold stress and material viscosity in the growth model. They also proposed a modification to the pressure-volume relation based in the MacKenzie (1949) model for the bulk modulus, and a dependence of the yield stress on the current void volume and density.

Gurson (1977) proposed a yield function for porous materials and a void nucleation model. The yield function was used as a plastic potential to define a flow rule that is independent of rate and thermal effects, but considers the void volume fraction in the damage material. The nucleation model is based on the statistical distribution of solid

particles in the matrix. Thus, a void is nucleated when a critical mean stress is reached and the particle surface is debonded from the matrix material. In his model he considered spherical and cylindrical geometries to describe the shape of the voids.

Norris *et al.* (1978) proposed a phenomenological model that describes the onset of fracture as a function of plastic-strain and mean-stress. Fracture occurs when a critical value of a cumulative-damage parameter is reached over a length that is characteristic of the material. They tested their model using simulations of tests that included simple tension, circumferentially notched tension, Charpy V-notched, and pre-cracked compact tension.

Wilkins *et al.* (1980) also proposed a cumulative-strain–damage model for ductile fracture. The damage parameter was defined to be a function of the equivalent plastic strain, the mean stress and the stress deviator. In this model fracture begins when the cumulative damage parameter exceeds a critical damage value over a critical distance. The model was calibrated and tested with simple tensile, cylinder impact, torsional and notched bar tensile tests.

Johnson (1981) presented the complete derivation of the void collapse model presented by Carroll *et al.* (1972) with significant additions. The first improvement proposed by Johnson was the generalization of the model to include not only void collapse but also void distension. He expanded on the work by MacKenzie (1949) to describe the elastic moduli dependence on void volume fraction by modifying it to make the shear modulus go to zero as the void volume fraction approached unity. In addition, he included rate effects in the yield function through a viscosity term, but left out thermal

softening and strain hardening effects. Even though he did not include thermal softening effects, he inferred that they were important since he had to reduce the viscosity of the material to 10P from room temperature values of approximately $\sim 10^5$ P to obtain results comparable to experiments. The inertial effect of the pore wall motion was neglected. He also addressed the problem of fragmentation of an expanding ring through the inclusion of a heterogeneous initial-void-volume-fraction distribution across the ring.

Tvergaard *et al.* (1982, 1984, 1986 and 1987) and Becker *et al.* (1988) presented a constitutive model to describe ductile fracture in polycrystalline metals by nucleation, growth and coalescence of voids. They considered a material with voids of different orders of magnitude in which the material has an initial array of large cylindrical voids and the material between these voids is modeled through a constitutive model for porous materials. Thus, fracture occurs when the large voids are linked by micro-cracks, which are a result of small-scale nucleation, growth and coalescence of micro-voids. Tvergaard (1982) proposed a yield condition for a porous solid that was based on the work of Gurson (1977), with modifications to improve the modeling of shear band localization. Tvergaard and Needleman (1984) also proposed a modification to the yield condition to account for failure through the introduction of a critical and ultimate void-volume-fraction. They also proposed phenomenological nucleation and growth models that are strain and stress driven. Tvergaard (1996) used his model to study the effect of void size distribution in the matrix material on the fracture process. He concluded that for large void volume fraction the small voids grow at a higher rate and conversely, for small void volume fraction the large voids grow at a higher rate.

Hancock *et al.* (1985) discussed the results of a finite element solution for a spherical elastic inclusion in a plastically deforming matrix. These results were used in conjunction with some experimental work using notched tensile specimens to generate multiaxial states of stress from which the local conditions leading to decohesion (void nucleation) of the inclusion/matrix interface were determined. One important feature of this study was the conclusion that there is a statistical distribution of interfacial strength. Some of the voids had a growth-threshold mean-stress approximately seven times the yield stress and some weakly bonded particles behave as pre-existing voids.

Carroll (1985) and Kim and Carroll (1987) presented an extension to his work of (Carroll 1972) to include a study of different strain hardening laws that allowed for a closed-form solution to the variable mean stress threshold for void volume fraction growth. The strain hardening laws included an elastic response, two saturation hardening laws, a pseudo-exponential hardening and a power-exponential hardening law. He also included some discussion on the behavior of these response laws in terms of the shape of the threshold mean stress as a function of void volume fraction. In addition, Carroll *et al.* (1986) presented a study of the effect of temperature on the viscoplastic response of a single void under compressive mean stress, concluding that the viscoplastic response is better modeled when the temperature effect is included. This was done by introducing a temperature dependent yield stress and viscosity model, and an energy rate balance equation.

Perzyna (1986) presented a model for dynamic fracture that was based in part on the work of Carroll (1972, 1985) and Johnson (1981). Perzyna simplified the void

growth model by also excluding the inertial effects, which transformed the second order nonlinear differential equation for void growth to a first order differential equation. He also proposed a viscoplastic model with linear work hardening for the void growth model but left out all temperature effects. The most important contribution by Perzyna was the formulation of an elastic-viscoplastic model of the voided solid that inherently described the dilatational effects and fracture generated by the nucleation, growth and coalescence of microvoids. His formulation was simpler than the one proposed by Tvergaard and Needleman (1984).

Curran *et al.* (1987) presented a thorough review of proposed models that describe the dynamic failure mechanisms in polycrystalline solids from micro and macroscopic points of view. In addition, they also presented a brief discussion of the experimental techniques used to characterize the dynamic fracture process. They presented a discussion of the models for void and crack nucleation, a discussion of the different models used to describe the growth of microvoids or shear bands and their interaction leading to the coalescence of microvoids or cracks.

Grady (1988) discussed the spall strength of solids in terms of its fracture energy. His study had the objective of identifying which properties of the material influence the damage process in both, brittle and ductile failure. He defined the spall strength for brittle fracture to be controlled by the fracture toughness, and for ductile fracture by the yield stress. Due to the simplifications and assumptions in the modeling, he reached conclusions that have been proven to be inaccurate, such as the conclusion that ductile spall strength is rate independent.

Rajendran *et al.* (1989) presented a dynamic failure model based on phenomenological observations. They modeled the plastic response of the matrix material with the Bodner and Partom model, which does not consider a yield condition, and the aggregate with voids with a model similar in form to Gurson's (1977) yield model. They tested their model with plate impact experiments of OFHC Copper at relatively low velocities ($<200\text{m/s}$).

In a series of papers from 1989 to 1996 Eftis and Nemes generalized Perzyna's viscoplastic-damage constitutive model and calculation of the microvoid growth rate, by incorporating nonlinear strain hardening that saturates for the viscoplastic material behavior. This elastic-viscoplastic microdamage constitutive model, appropriate for isothermal ductile fracture of polycrystalline materials, was used to successfully describe the main features of plate impact-induced spall fracture for: (i) Rectangular plates, (ii) oblique impact of rectangular plates, (iii) circular plates with the flyer having smaller diameter than the target, and (iv) very high strain rate fracture of unnotched round tensile bars. The constitutive-microdamage equations have also been employed to analytically demonstrate the known experimental fact that elasto-viscoplastic waves can be propagated through damaged softened (i.e. unstable) polycrystalline materials.

Cortes (1992) presented a pore growth model that was based on the model proposed by Carroll (1972, 1985) and Johnson (1981) with the inclusion of linear hardening and viscous and thermal effects but with a simplified definition of strain. He also proposed a modification to the original model to include the effects of deviatoric stresses on the growth of microvoids. He concluded that the thermal effect on the void

volume fraction evolution was negligible, which contradicts the findings of Johnson (1981) and Carroll and Kim (1986). Cortes *et al.* (1995) modified his model to include void nucleation and modified the growth threshold-mean-stress using Gurson's (1977) yield model. He used his new model to simulate spall fracture in plate impacts and explosive loading of plates with good agreement between experiment and simulation results in terms of the velocity profile of the target rear surface.

Benson (1993) presented a study of the effect of void distribution on the dynamic growth and coalescence of voids. Computer simulations were made of different patterns of cylindrical voids in OFHC Copper and 4340 Steel. The Johnson-Cook model was used to describe the viscoplastic behavior of the material and a simple limit-strain fracture model was implemented. The most important conclusion from his work was that the fracture path for the two materials was different. While for OFHC Copper fracture was reached when the voids grew until they connected, 4340 fractured by failure of the material between the voids. Benson concluded that the difference in fracture paths was due to the large difference in the strain-threshold for fracture.

Tong *et al.* (1993) presented a study of the inertial, thermal and viscous effects on the void collapse obtained through a model similar to the Carroll and Johnson models and presented comparative results with Carroll's model. In 1995 Tong did a similar study of the inertial effects on the void collapse predicted by the Gurson yield model. In all cases, he concluded that inertial and dynamic effects in general have a significant effect on the pore collapse predictions.

Addressio *et al.* (1993), Lee *et al.* (1994, 1996) presented studies of some of the

models already mentioned in this review for specific applications (i.e. compaction of cylinders, formability, etc) and proposed small improvements with suggested shortcomings and strengths of the models.

Kanel *et al.* (1996) presented the results of a series of experiments done on Aluminum AD1 and Magnesium Mg95 plates to investigate the effect of temperature on the spall strength of these materials. The conclusion was that a higher initial temperature of the specimens caused the spall strength to decrease, which again, contradicts the conclusion of Cortes and supports the conclusions by Carroll and Kim (1986) and Johnson (1981).

1.1.3 Computer Codes

The literature review in terms of the numerical algorithms and computer codes was not as extensive as in the areas of constitutive models and fracture, and in the following section on materials characterization of after shock specimens. The objective of the review on computer codes is directed towards providing an overview of the numerical algorithms used in the commercial and public domain codes used to simulate hypervelocity impacts, and not to give a detailed exposition of the evolution of every component and algorithm that compose current computer codes. The reason for this is that the research work emphasized the development of an elastic-viscoplastic micro-damage constitutive model appropriate for hypervelocity impact and its implementation as separate subroutines in an existing computer code.

Current computer codes and their algorithms are based on the work by Wilkins *et*

al. (1974) where they described the details for the development of a three-dimensional finite element/finite difference computer program to solve high-shock and high non-linear deformation problems in a Lagrangian grid.

Liu *et al.* (1986) and Benson (1989) presented the conservation laws, the constitutive relations, and the pressure-volume relations for the modeling of path-dependent materials in an arbitrary Lagrangian-Eulerian finite element method.

Johnson *et al.* (1987) introduced an eroding algorithm to be incorporated in a Lagrangian finite element code to simulate projectile penetration/perforation of thick plates. The objective of this eroding algorithm is to eliminate computational cells when they reach a limit strain.

McGlaun *et al.* (1990) gave a brief description of the models and features available in the CTH Eulerian code. Trucano *et al.* (1990) showed the results of CTH simulations of hypervelocity impacts. They reported on the effect of grid density, advection and interface tracking algorithms and other factors on the simulation errors.

Anderson (1987) provides an extensive review of the evolution of "Hydrocodes". He discusses Lagrangian and Eulerian formulations, including advantages and disadvantages, the concept of artificial viscosity to deal with discontinuities of shocks, and finally the treatment of constitutive models, pressure-volume relations, eroding algorithms and fracture.

1.1.4 Microstructural Studies

This section of the review will briefly discuss microstructural studies as they

relate to hypervelocity impact specimens. The papers discussed in this section concentrate on the effects of pre-impact microstructure and the microstructural features observed in after-impact specimens.

Meyers *et al.* (1981) presented a short review of the mechanisms that lead to defect generation under shock deformation. They discussed the formation of point, line and planar defects, and phase transformations.

Gray III (1993) gives a review of the effects of shock deformation on material response. He discusses the techniques and design parameters used in shock recovery experiments, and the influence of shock parameters, including peak pressure, pulse duration and loading rate on post-shock structure or properties of the material.

Ferreya *et al.* (1995) provided a study of the effects of target microstructure on crater depth, diameter and depth to diameter ratios in a Copper plate impacted by a spherical projectile at high velocity. They conclude that there is a profound effect of target microstructure on cratering characteristics.

Rivas *et al.* (1995) gave a brief discussion of the different after-shock microstructural characteristics observed in OFHC Copper, 1100 and 6061-T6 Aluminum targets.

Murr *et al.* (1996) discussed the deformation processes and microstructures associated with different high deformation configurations. They discussed the microstructural features and deformation mechanisms associated with plate impact experiments, shaped charges, explosively formed penetrators, spherical projectile hypervelocity impacts and long rod penetration of thick targets.

Quiñones (1996) provided a very thorough study of the microstructural features observed in post impact OFHC Copper plates. The study included the discussion of microstructural-features and hardness profiles across the thickness of the target plate after impact at different velocities. She also simulated the impacts on a computer code and correlated the hardness profile with residual yield stress as defined by the Johnson-Cook yield model. Quiñones *et al.* (1998) extended the simulation study to include the simulation of spall fracture using a limit stress fracture model.

Murr *et al.* (1997) and Ferreyra *et al.* (1997) provided a study of microstructure after high velocity and hypervelocity impact cratering of Copper targets. They conclude that the target microstructure has a strong effect on the geometrical characteristics of the craters, especially the dislocation structure while grain size seems to have an insignificant effect.

1.2 Objective

The research presented in this dissertation seeks to expand the capability of current constitutive models for the simulation of hypervelocity impact problems. This is accomplished through the development of a more general constitutive-microdamage model that can describe high shock compression, dilatation, shear and material microdamage evolution leading to fracture, assuming thermoelastic-thermoviscoplastic material behavior. The microdamage model presented here incorporates a non-linear pressure volume relation for shock compression and dilatation, along with expressions for the elastic moduli that include volume strain dependence as well as thermal and

microdamage softening. The viscoplastic response equations incorporate nonlinear strain and strain rate hardening as well as thermal and microdamage softening with temperature dependent viscosity, and include plastic compressibility due to microvoid volume fraction change. The melt temperature is assumed to be volume strain dependant. The microdamage evolution model includes microvoid void nucleation with a variable mean stress threshold and microvoid growth with void interaction effects. The microvoid growth model incorporates a viscoplastic material model with nonlinear strain and strain rate hardening as well as thermal softening, and a temperature dependant viscosity.

The work presented in this dissertation improves upon previous works, related to hypervelocity impact modeling and simulation, in several key issues.

- 1) The constitutive model presented here is the most extensive in the sense that it incorporates more of the known polycrystalline material behavior issues, which were described in this section.
- 2) In the constitutive model presented here, the softening effect of microdamage is incorporated into the Johnson-Cook model for the yield function, as well as in the equations for the elastic moduli.
- 3) In the microvoid nucleation rate equation, the threshold mean-stress is not assumed constant but is expressed as a function of equivalent plastic strain and strain rate.
- 4) A temperature rate equation local to the wall of a growing microvoid is formulated. The temperature calculated with this equation is substituted in the expressions for the temperature dependent material viscosity and threshold mean-

stress for microvoid growth. This provides analytical justification for the reduced temperature-independent viscosity used by Johnson (1981) and Eftis *et al.* (1991), and represents an important improvement over previous models.

- 5) In the expression for the viscoplastic rate of deformation tensor, the volumetric component (due to microvoid volume change) is not explicitly coupled to the deviatoric component. This corrects the problems associated with the Perzyna's model (Perzyna, 1986) that give a non-zero value to the volumetric contribution from microvoid growth even when the microvoid volume rate of change is zero.
- 6) Most of the constitutive models for the simulation of hypervelocity impact problems presented in the literature are tested with only one computer simulation, while the simulations reported in this dissertation (see Chapter 6) cover a wide range of plate target thickness that result in widely varied levels of damage. These simulations provide a measure of the capability and performance of the microdamage constitutive model in the simulation of hypervelocity impact problems under varied geometrical configurations.

CHAPTER 2

RANKINE-HUGONIOT RELATIONS

Extensive experimental characterizations of the pressure-volume (P-V) relations for various materials for a wide range of shock pressures have been developed since the 1950's (Walsh *et al.* 1957). Most of the data compiled has been produced through contact explosive detonation, or the "flyer plate" experiment where a projectile plate is explosively accelerated towards a target plate in a configuration that produces planar shock waves across the projectile and target plates. The data is usually presented as P-V curves or curves that relate the shock wave speed U_S to the particle velocity U_P behind the shock front. It has been discovered experimentally that for polycrystalline metals under a wide range of shock pressures the U_S - U_P curve can be expressed as a linear equation,

$$U_S = c_0 + sU_P \quad (2.1)$$

where c_0 is the sound speed in the material at atmospheric pressure and room temperature ($\sim 300^\circ\text{K}$), s is the slope of the U_S - U_P linear relation and U_P is the particle speed behind the shock front. It is important to note that the experimental setup produces planar shock waves where the deviatoric stresses are non-zero and thus some plastic deformation and "residual" temperature is to be expected if the dynamic yield stress is exceeded. Figure 2.1 shows experimental data points for Copper in the U_S - U_P plane with a linear fit through the points.

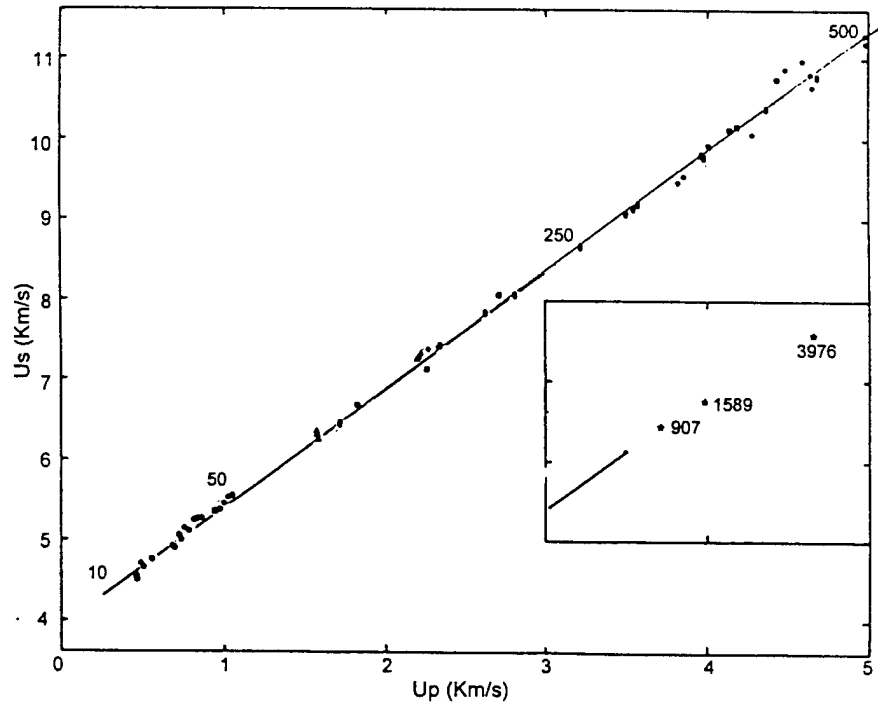


Figure 2.1 High-pressure Hugoniot data for Copper obtained by several investigators. The numerals along the curve indicate pressures in GPa. The line on the small inset represents the entire range of the larger figure, while the three points represent the results of Soviet ultrahigh pressure experiments (Davison *et al.* 1979).

The development of a P-V equation for shock loading requires the implementation of the “jump conditions” across the shock wave coupled with the U_S-U_P linear relation. The “jump conditions” are determined by the conservation of mass, linear momentum and energy that relate the density, particle velocity and stresses across the discontinuity produced by the moving shock wave, and can be stated at first in general terms by the well known jump relations (Figure 2.2),

$$\rho^+(u_n - v_n^+) = \rho^-(u_n - v_n^-), \text{ conservation of mass} \quad (2.2)$$

$$\begin{aligned} & \rho^+ v^+ (u_n - v_n^+) + \mathbf{T}^+ \cdot \mathbf{n} \\ & = \rho^- v^- (u_n - v_n^-) + \mathbf{T}^- \cdot \mathbf{n} \end{aligned}, \text{ conservation of momentum} \quad (2.3)$$

$$\begin{aligned} & \rho^+ \left(\frac{1}{2} \mathbf{v}^+ \cdot \mathbf{v}^+ + E^+ \right) (u_n - v_n^+) + \mathbf{t}^+ \cdot \mathbf{v}^+ - \mathbf{q} \cdot \mathbf{n} \\ & = \rho^- \left(\frac{1}{2} \mathbf{v}^- \cdot \mathbf{v}^- + E^- \right) (u_n - v_n^-) + \mathbf{t}^- \cdot \mathbf{v}^- - \mathbf{q} \cdot \mathbf{n} \end{aligned} \quad , \text{ conservation of energy} \quad (2.4)$$

where ρ is the density, u_n is the speed of the shock wave along a unit vector normal to the shock front (\mathbf{n}), v_n is the particle speed along vector \mathbf{n} , \mathbf{v} is the particle velocity vector, \mathbf{T} is the Cauchy stress tensor, \mathbf{t} is equal to $\mathbf{T} \cdot \mathbf{n}$, which is the traction vector across the wave front, E is the internal energy per unit mass and \mathbf{q} is the heat flux. In these equations, the functions (ϕ^+) and (ϕ^-) indicate the limits of the function ϕ as the shock wave is approached from the front (material into which the wave is advancing) and from the back, respectively.

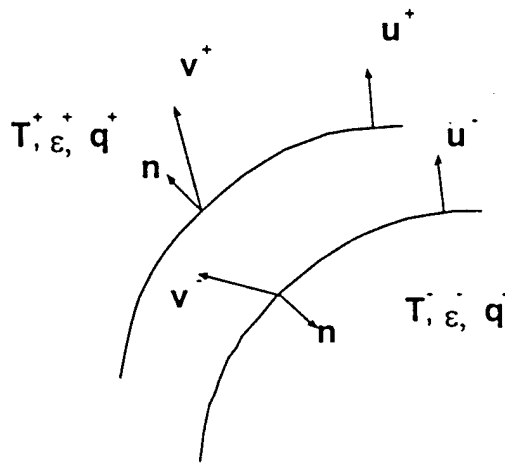


Figure 2.2 Depiction of the state of the material ahead and behind the Shock-Front.

If we make the shock front a planar surface moving in the x_1 direction of a rectangular Cartesian coordinate system so that $|\mathbf{n}| = n_1 = 1$, $\mathbf{q} = \mathbf{0}$ (adiabatic conditions), and denote $u_n = u_1$ then Equations (2.2) - (2.4) can be expressed as,

$$\rho^+(u - v_1^+) = \rho^-(u - v_1^-) \quad (2.5)$$

$$\rho^+ v_1^+(u - v_1^+) + T_{11}^+ = \rho^- v_1^-(u - v_1^-) + T_{11}^- \quad (2.6a)$$

$$T_{12}^+ = T_{12}^- \quad (2.6b)$$

$$T_{13}^+ = T_{13}^- \quad (2.6c)$$

$$\rho^+ \left(\frac{1}{2} (v_1^+)^2 + E^+ \right) (u - v_1^+) + T_{11}^+ v_1^+ = \rho^- \left(\frac{1}{2} (v_1^-)^2 + E^- \right) (u - v_1^-) + T_{11}^- v_1^- \quad (2.7)$$

Equations (2.6b) and (2.6c) state that the shear stress fields T_{12} and T_{13} are continuous across the planar shock wave. If we now let $v^+ = 0$ and make $u = U_s$, $v_1^- = U_p$, $\rho^+ = \rho^0$, $\rho^- = \rho$, making use of Equations (2.1) and (2.5) – (2.7) we can simplify the jump equations, and obtain the Rankine-Hugoniot equations

$$\rho_0 U_s = \rho (U_s - U_p) \quad (2.8)$$

$$T_{11}^+ - T_{11}^- = \rho_0 U_p U_s \quad (2.9)$$

$$E^- - E^+ = \frac{1}{2} \frac{(T_{11}^+ + T_{11}^-) \left(1 - \frac{\rho}{\rho_0} \right)}{\rho} \quad (2.10)$$

Combining Equations (2.1), (2.11) and (2.12) yields,

$$T_{11}^+ - T_{11}^- = \frac{\rho_0 c_0^2 \psi}{[1 - s\psi]^2} \quad (2.11)$$

where, $\psi = 1 - \frac{\rho_0}{\rho}$, is the volume strain. (2.12)

Equation (2.11) represents the change in stress T_{11} from an initial state to a shocked state. This equation can be modified and generalized to a shock wave front with

arbitrary orientation. Then the uniaxial stress can be replaced by the negative of the mean stress (denoted as a 'pressure') $P \equiv -\frac{1}{3} \text{tr} \mathbf{T}$ so that Equation (2.11) can be stated as,

$$P_H - P_0 = \frac{\rho_0 c_0 \Psi}{[1 - s\Psi]^2} = P_{H_0} \quad (2.13)$$

where P_H is the Hugoniot pressure above a zero pressure reference, P_0 is the pressure acting on the material ahead of the shock front above the zero pressure reference and P_{H_0} is the Hugoniot pressure above P_0 . When the volume strain ψ is positive signifying volume reduction, the 'pressure' P is positive, and conversely when the volume strain is negative signifying dilatation, P is negative.

Equation (2.13) is generally called the Hugoniot pressure and represents the locus of all the shocked states as depicted in Figure 2.3. When a material is shocked, the pressure does not follow the Hugoniot (P - ψ) pressure, but increases discontinuously from its initial state P_0 to P_1 following the Rayleigh line (Davison *et al.* 1979 and Boslough *et al.* 1993). Similarly, from Equation (2.10) the change in internal energy due to the shock compression can be shown to be,

$$E_H - E_0 = \frac{1}{2} \frac{(p + p_0)\psi}{\rho_0} = E_{H_0} \quad (2.14)$$

where E_H is the Hugoniot energy above a zero energy reference, E_0 is the energy of the material ahead of the shock front above the zero energy reference and E_{H_0} is the Hugoniot energy above E_0 . It should be noted that Equation (2.14) gives the area between the Rayleigh line and the zero reference pressure (Figure 2.3).

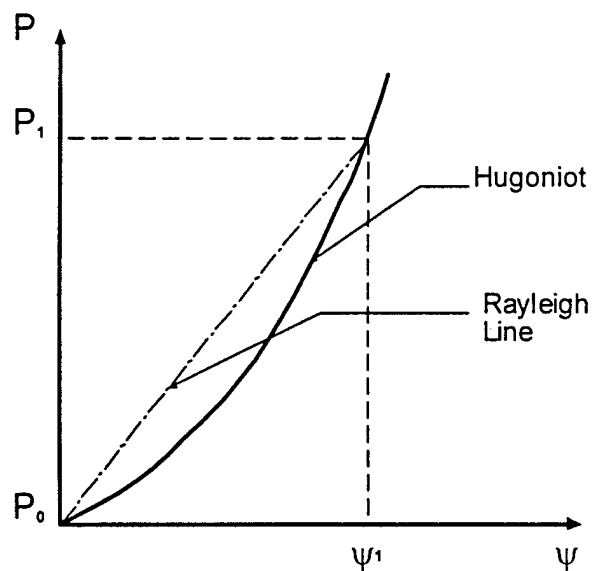


Figure 2.3 Shock Hugoniot pressure curve and Rayleigh line for a given pressure P_1 .

Equation (2.13) and (2.14) represent the pressure and energy increments associated with a change in volume strain (ψ), but do not include thermal contributions from plastic work associated with the deviatoric stresses.

CHAPTER 3

GRUNEISEN EQUATION OF STATE

The thermal pressure within a material is associated with its thermal energy, which can be calculated approximately by assuming the ion cores of a crystal lattice as N -many simple harmonic oscillators (the oscillations of the free electron gas are not considered). The oscillators are vibrating in the normal modes of the three-dimensional system at frequencies $\nu_i(\nu)$ that are assumed to depend only upon the specific volume (Walsh *et al.* 1957). From quantum mechanical calculations of the energy of a system of $3N$ oscillators coupled with a statistical mechanics representation of the thermal energy of the lattice, for any temperature $T > 0^\circ\text{K}$ the total energy can be shown to be given by

$$E(\nu, T) = \Phi_0(\nu) + \frac{1}{2} \sum_i^{3N} \hbar \nu_i + \sum_i^{3N} \frac{\hbar \nu_i}{e^{\hbar \nu_i / \kappa T} - 1} \quad (3.1)$$

where, $\Phi_0(\nu)$ is the binding energy of the lattice at 0°K , $\frac{1}{2} \sum_i^{3N} \hbar \nu_i$ is the ground state energy of the 0°K oscillations at the lowest energy state and $\sum_i^{3N} \frac{\hbar \nu_i}{e^{\hbar \nu_i / \kappa T} - 1}$ is the thermal energy of the oscillating lattice, with the summation being over the $3N$ normal modes of the crystal. The constants \hbar and κ are the Planck and Boltzman constants respectively.

The Helmholtz free energy can be expressed as

$$H = E - TS. \quad (3.2)$$

S is the thermodynamic entropy defined from statistical mechanics as

$$S = \kappa \ln \sum_{n=0}^{\infty} e^{E(n)/\kappa T} + \frac{E}{T} \quad (3.3)$$

where

$$E(n) = \Phi_0 + \sum_i^{3N} \left(n + \frac{1}{2} \right) \hbar v_i . \quad (3.4)$$

and n is the occupation number of the phonon energy levels oscillating at the i^{th} frequencies. Substituting Equation (3.3) in (3.2) leads to,

$$H = -\kappa T \ln \sum_{n=0}^{\infty} e^{E(n)/\kappa T} \quad (3.5)$$

Then, substituting Equation (3.4) in (3.5) leads to the following expression for the Helmholtz free energy

$$H = \Phi_0 + \frac{1}{2} \sum_i^{3N} \hbar v_i + \kappa T \sum_i^{3N} \ln \left[1 - e^{-\hbar v_i / \kappa T} \right] \quad (3.6)$$

The external pressure is defined as the specific volume derivative of the free energy at constant temperature taken as negative for volume compression, giving the result

$$P = - \left(\frac{d\Phi_0}{dv} \right)_T + \frac{1}{2} \sum_i^{3N} \frac{\gamma_i(v)}{v} \hbar v_i + \sum_i^{3N} \frac{\gamma_i(v)}{v} \frac{\hbar v_i}{e^{\hbar v_i / \kappa T} - 1} \quad (3.7)$$

$$\text{where } \frac{\gamma_i(v)}{v} = - \frac{1}{v} \left(\frac{d \ln v_i}{d \ln v} \right)_T = - \frac{1}{v_i} \left(\frac{d v_i}{d v} \right)_T . \quad (3.8)$$

Equation (3.8) represents what is known as the Gruneisen ratio at the i^{th} frequency and is a function of the specific volume (v). A general assumption that is used to simplify Equation (3.7) is to take all the frequencies (v_i) for the $3N$ harmonic oscillators as being equal. This leads to the following simplification for the Gruneisen parameter

$$\gamma_i(v) = \gamma_i(v). \quad (3.9)$$

Substituting Equation (3.9) in (3.7) leads to the following simplified definition of the pressure,

$$P = -\left(\frac{d\Phi_0}{dv}\right)_T + \frac{1}{2} \frac{\gamma(v)}{v} \sum_i^{3N} \hbar v_i + \frac{\gamma(v)}{v} \sum_i^{3N} \frac{\hbar v_i}{e^{\hbar v_i/kT} - 1}. \quad (3.10)$$

If we now define

$$E(v)_{0^\circ K} = \Phi_0(v) + \frac{1}{2} \sum_i^{3N} \hbar v_i, \text{ as the cold energy} \quad (3.11)$$

and

$$E_{th}(v, T) = \sum_i^{3N} \frac{\hbar v_i}{e^{\hbar v_i/kT} - 1}, \text{ as the thermal energy,} \quad (3.12)$$

then

$$P(v)_{0^\circ K} = -\left(\frac{d\Phi_0}{dv}\right)_T + \frac{\gamma(v)}{v} E_0(v), \text{ represents the cold pressure.} \quad (3.13)$$

By combining Equations (3.10), (3.12) and (3.1) the pressure at specific volume (v) and temperature (T) can be expressed as

$$P(v, T) = P(v)_{0^\circ K} + \frac{\gamma(v)}{v} E_{th}(v, T). \quad (3.14)$$

This definition of the pressure can be traced, in Figure 3.1, by following the $0^\circ K$ isotherm up to specific volume (v) or volume-strain (ψ) at pressure $P(\psi, 0^\circ K)$ and then adding, at constant volume, the thermal contribution up to $P(\psi, T)$.

From Equations (3.1), (3.11) and (3.12) we can define the thermal energy as follows:

$$E_{th}(v, T) = E(v, T) - E(v)_{0^\circ K} \quad (3.15)$$

Substituting Equation (3.15) in (3.14) we reach the following result,

$$P(v, T) = P(v)_{0^\circ K} + \frac{\gamma(v)}{v} (E(v, T) - E(v)_{0^\circ K}) \quad (3.16a)$$

$$P(v, T) - P(v)_{0^\circ K} = \frac{\gamma(v)}{v} (E(v, T) - E(v)_{0^\circ K}). \quad (3.16b)$$

Equation (3.16a) is known as the general Mie-Gruneisen Equation of state (EOS). Equation (3.16b) represents the change in pressure above the 0°K isotherm (P-V-E) curve. This form of the Mie-Gruneisen EOS makes it easy to visualize the fact that it can be rewritten in terms of any other (P-V-E) curve. Rewriting Equation (3.16a) in terms of the Hugoniot curve taken as reference,

$$P(v, T) = P_H + \frac{\gamma(v)}{v} (E(v, T) - E_H). \quad (3.17)$$

This definition of the pressure can be traced, in Figure 3.1, by following the Hugoniot curve from the P_0 point up to P_H and then adding the partial thermal contribution by the difference between the total energy $E(\psi, T)$ and the Hugoniot energy E_H .

Then, substituting Equations (2.13) and (2.14) in Equation (3.17) and rearranging terms,

$$P(\psi, T) - P_0 = P_{H_0} + \gamma(\psi)\rho(E_{H_0}) + \gamma(\psi)\rho(E(v, T) - E_0) \quad (3.18a)$$

$$P(\psi, T) - P_0 = \frac{\rho_0 c_0^2 \psi}{[1 - s\psi]^2} \left(1 - \frac{1}{2} \gamma(\psi) \left(\frac{\psi}{1 - \psi} \right) \right) + \gamma(\psi)\rho(E(\psi, T) - E_0). \quad (3.18b)$$

Equation (3.18a) represents the change in pressure above the reference point (P_0, E_0) which has to be the room conditions of 300°K temperature and atmospheric pressure, since these are the conditions under which the U_S-U_P curves (Eq 2.1) that form the basis for the Hugoniot curve, are experimentally obtained. Thus the Mie-Gruneisen (P-V-E)

equation can be simplified as follows with the understanding that the pressures and energies represent changes with respect to the reference point previously mentioned,

$$P(\psi, T) = \frac{\rho_0 c_0^2 \psi}{[1 - s\psi]^2} \left(1 - \frac{1}{2} \gamma(\psi) \left(\frac{\psi}{1 - \psi} \right) \right) + \gamma(\psi) \rho E(\psi, T), \quad \psi > 0 \quad (3.19)$$

where $E(\psi, T)$ is the internal energy per unit mass that can be calculated by the energy rate balance equation appearing in Section 4.5.

Figure 3.1 presents a qualitative illustration of all the different terms that lead to the formulation of the Mie-Gruneisen (P - ψ) curve.

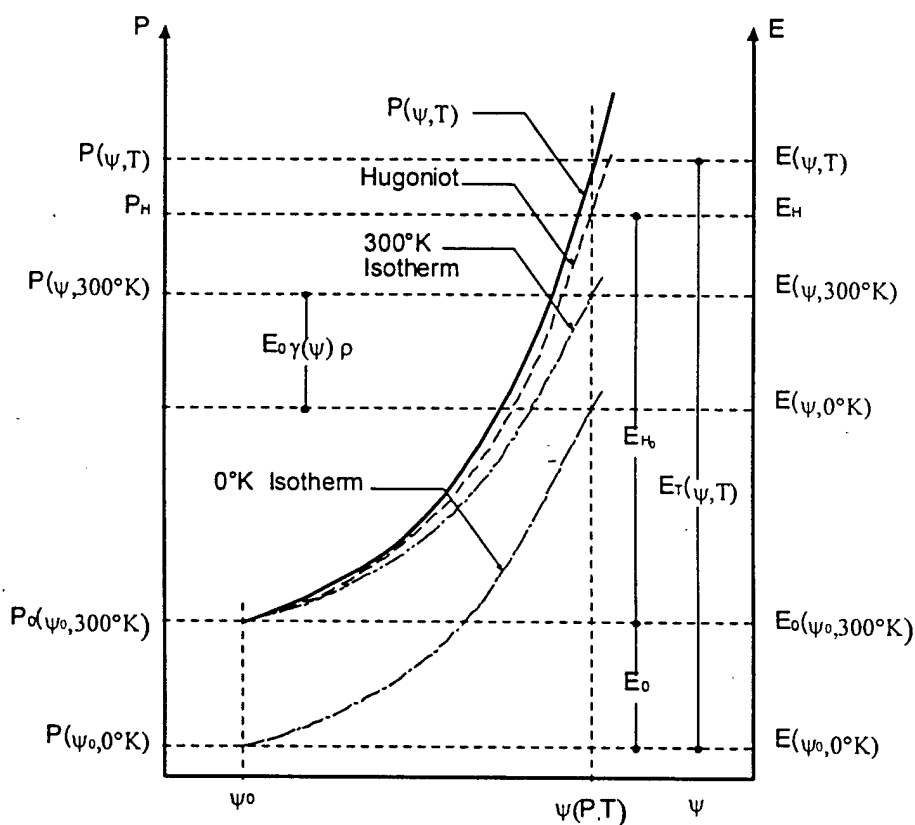


Figure 3.1 Mie-Gruneisen, Hugoniot, 0°K and 300°K Isothermal Pressure-Volume Strain Curves.

The volume strain dependence of the Gruneisen coefficient $\gamma(\psi)$ of Equation (3.19) can be expressed as a polynomial with empirically determined coefficients (Walsh *et al.* 1957). Then, to a first order approximation $\gamma(\psi)$ is expressed as

$$\gamma(\psi) = \gamma_0 + A \left(\frac{\psi}{1-\psi} \right) \quad (3.20)$$

where, for example the coefficients γ_0 and A have the values (2.04, -3.296), respectively for Copper and (2.13, -7.245) for Aluminum-24ST.

Insertion of (3.20) into (3.19) gives the nonlinear pressure-volume strain relation (equation of state) associated with shock compression of polycrystalline materials.

$$P(\psi, T) = \frac{\rho_0 c_0^2 \psi}{[1-s\psi]^2} \left(1 - \frac{1}{2} \left\{ \gamma_0 \left(\frac{\psi}{1-\psi} \right) + A \left(\frac{\psi}{1-\psi} \right)^2 \right\} \right) + \left[\gamma_0 + A \left(\frac{\psi}{1-\psi} \right) \right] \rho E(\psi, T), \quad \psi > 0 \quad (3.21)$$

It will be recalled that in the development of Equation (2.19) the 'pressure' term P actually represents the negative of the mean stress $P = -\frac{1}{3} \text{tr } \mathbf{T} = -\sigma_m$, as designated above, E is the internal energy per unit mass, ρ , ρ_0 are the mass densities in the current and reference states, (c_0) is the sound speed and (s) is the experimentally determined slope in the shock wave speed-particle speed relation (2.1)

CHAPTER 4

CONSTITUTIVE – MICRODAMAGE MODEL

4.1 Introduction

The governing balance Equations of continuum mechanics, expressed in local form, state that for any deforming material body the balance of mass, linear momentum, moment of momentum and energy, respectively, requires that the following Equations be satisfied at each point of the body

$$\frac{\partial \rho}{\partial t} + \text{grad } \rho \cdot \mathbf{v} + \rho \text{div } \mathbf{v} = 0 \quad (4.1)$$

$$\text{div } \mathbf{T} + \rho \mathbf{b} = \rho \frac{d\mathbf{v}}{dt} \quad (4.2)$$

$$\mathbf{T} = \mathbf{T}^T \quad (4.3)$$

$$\rho \frac{d\epsilon}{dt} = \text{tr}(\mathbf{T} \cdot \mathbf{D}) + \rho h - \text{div } \mathbf{q} \quad (4.4)$$

where ρ is the mass density, \mathbf{v} is the velocity vector, \mathbf{T} the Cauchy stress tensor where the superscript denotes transpose, \mathbf{b} is the body force per unit mass, \mathbf{D} is the rate of deformation tensor, h is the heat source per unit mass and \mathbf{q} is the heat conduction vector.

In the work that follows the material behavior involves polycrystalline solids that deform elastically and viscoplastically. Therefore, it is convenient to decompose the rate of deformation tensor additively into elastic and viscoplastic parts

$$\mathbf{D} = \mathbf{D}^e + \mathbf{D}^p \quad (4.5)$$

where

$$\mathbf{D} = \frac{1}{2}(\text{grad } \mathbf{v} + (\text{grad } \mathbf{v})^T). \quad (4.6)$$

4.2 Elastic Rate of Deformation

The previously described conservation equations represent the mathematical descriptions of stress, strain and rate of deformation and they apply to all continuous media. On the other hand, the constitutive equations characterize the individual materials and their specific reactions to applied loads. Due to the complexity of the material response of different materials it is not feasible to have a single constitutive relation that can be applied to all materials under all loading conditions. For this reason, the constitutive model developed as part of the current dissertation work is tailored to high shock compression, high strain, high strain rate and high temperature deformation problems.

In a general sense, a constitutive model is defined as the function or functions that relate the stress to the strain or strain rates. For the simulation of hypervelocity impacts, the most widely used form of the constitutive model is the one that relates stress to the rate of deformation. In addition, for the model presented in this dissertation, the constitutive model will be combined with thermoelastic, thermo-visco-plastic equations and a micro-damage model that will couple the elastic moduli and viscosity coefficients to temperature and micro-damage levels.

The high compression caused by hypervelocity impact produces large elastic volume strain. The elastic shear deformations however are small order because of

limitations imposed by onset of plastic yield in polycrystalline materials. It is advantageous therefore to decompose \mathbf{D}^e into volumetric and deviatoric components

$$\mathbf{D}^e = \frac{1}{3K} (\text{tr} \mathbf{D}^e) \mathbf{1} + \mathbf{D}'^e, \quad (4.7)$$

where the elastic rate of volume strain is related to the mean stress and the bulk modulus, K , while the elastic rate of small shear is determined by the stress deviator and the elastic shear modulus, μ . Since the shear strains must be small in the elastic range it follows from generalized Hooke's Law that

$$\mathbf{D}'^e = \frac{1}{2\mu} \overset{\nabla}{\mathbf{T}}' \quad (4.8)$$

where \mathbf{T}' is the deviator of the Cauchy stress \mathbf{T} , and $\left(\overset{\nabla}{\dots} \right)$ represents the frame indifferent Jaumann time rate, whereby for any tensor \mathbf{A} is given by

$$\overset{\nabla}{\mathbf{A}} = \frac{\partial \mathbf{A}}{\partial t} + \mathbf{A} \cdot \text{grad} \mathbf{v} + \mathbf{A} \cdot \mathbf{W} - \mathbf{W} \cdot \mathbf{A} \quad (4.9)$$

where \mathbf{W} is the rotation tensor

$$\mathbf{W} = \frac{1}{2} (\text{grad} \mathbf{v} - (\text{grad} \mathbf{v})^T). \quad (4.10)$$

During high shock compression and release, the large elastic compressive volume strain rate is related to the applied mean stress rate and the elastic bulk modulus K , such that

$$\frac{1}{3} (\text{tr} \mathbf{D}^e) \mathbf{1} = \frac{1}{3} \frac{\overset{\nabla}{\sigma}_m}{K} \mathbf{1} \quad (4.11)$$

where here and throughout what follows, σ_m signifies the mean stress $\frac{1}{3}(\text{tr } \mathbf{T})$. We note that in keeping with the notation and language commonly employed in discussions of the Rankine-Hugoniot equations introduced in Section 3, the mean stress there is referred to as 'pressure' - $P \equiv \frac{1}{3} \text{tr } \mathbf{T}$. From expressions (4.8) and (4.11)

$$\mathbf{D}^c = \frac{1}{3} \frac{\sigma_m}{K} \mathbf{1} + \frac{1}{2\mu} \mathbf{T}^v \quad (4.12)$$

The pressure associated with the large volume strains that accompany high shock compression is determined by the Gruneisen Equation (3.21), here reproduced again as Equ. (4.13)

$$P(\psi, T) = \frac{\rho_0 c_0^2 \psi}{[1-s\psi]^2} \left(1 - \frac{1}{2} \left\{ \gamma_0 \left(\frac{\psi}{1-\psi} \right) + A \left(\frac{\psi}{1-\psi} \right)^2 \right\} \right) + \left[\gamma_0 + A \left(\frac{\psi}{1-\psi} \right) \right] \rho E(\psi, T), \quad \psi > 0 \quad (4.13)$$

where it will be recalled that $\psi = 1 - \frac{v}{v_0} = 1 - \frac{\rho}{\rho_0}$ is the volume strain. The compression wave induced by the hypervelocity impact is followed by a reflected tensile wave from the target rear free surface, causing dilatation (negative volume strain). During the shock compression stage the shock wave speed is greater than the bulk sound speed (Figure 2.1) because of the large volume compression. During the dilatation however, the crystal lattice structure is expanding, thereby reducing the tensile wave speed (which is no longer a shock wave) to the bulk sound speed c_0 . This is equivalent to setting $s=0$ in Equation (2.1). Therefore, during dilatation the pressure has the value

$$P(\psi, T) = K \psi \left(1 - \frac{1}{2} \left\{ \gamma_0 \left(\frac{\psi}{1-\psi} \right) + A \left(\frac{\psi}{1-\psi} \right)^2 \right\} \right) + \left[\gamma_0 + A \left(\frac{\psi}{1-\psi} \right) \right] \rho E(\psi, T), \quad \psi \leq 0 \quad (4.14)$$

The tensile volume strains cannot assume values as large as the volume strains in compression (that can reach values as high as thirty to forty percent), because of impending fracture. It may turn out that terms of third order (and possibly of second order) in ψ , in expression (4.14) are small enough to be negligible.

All polycrystalline materials contain microvoids and microcracks. Since impact at hypervelocity can produce large adiabatic temperature increases, the corresponding dynamic fracture will be ductile, caused essentially by nucleation, growth and joining together of microvoids. The measure of ductile material microdamage can therefore be described by microvoid volume fraction $\xi = v_v/v$, where v_v is the void volume for a material element having volume v . The microdamage is viewed as a scalar-valued continuous point function of position and time, i.e., $\xi(\mathbf{x}, t)$ similar to the other field variables. For polycrystalline metals the average initial microvoid volume fraction ranges from $\xi_0 \approx 10^{-4} - 10^{-3}$ (Curran *et al.* 1987). The large volume strains of compression following impact will reduce them further to insignificant values. On the other hand the dilatation driven by the tensile mean stress wave, when high enough, induces microvoid nucleation and growth, i.e., material microdamage that is revealed in optical micrographs (Curran *et al.* 1987) and by the reduced values for the elastic moduli (Eftis 1996).

In circumstances that involve hypervelocity impact, formulation of constitutive relations for the elastic moduli requires consideration of high volume strain, large

temperature changes and microdamage softening. With this in mind, the elastic bulk and shear moduli can be represented initially by the following form.

$$K(\psi, \xi, T) = K_0 f_{K1}(\psi) f_{K2}(\xi) f_{K3}(T) \quad (4.15)$$

$$\mu(\psi, \xi, T) = \mu_0 f_{\mu1}(\psi) f_{\mu2}(\xi) f_{\mu3}(T) \quad (4.16)$$

Where $K_0 = \rho_0 c_0^2$ and μ_0 are the elastic bulk and shear moduli in the reference state: $\psi=0$, $T=T_0=300^\circ\text{K}$ and $\xi=\xi_0$, and where f_{K1}, \dots, f_{K3} , and $f_{\mu1}, \dots, f_{\mu3}$ are initially undetermined functions of their respective arguments.

The bulk modulus is defined as (Malvern 1969),

$$K = \frac{1}{\rho} \left. \frac{\partial \sigma_m}{\partial v} \right|_T \quad (4.17)$$

In calculating this derivative the frequently used approximation $\rho\gamma(\psi) = \rho_0\gamma_0$ is employed (Herrmann 1969), which is equivalent to taking $A=0$ in Equations (3.20) and (4.13). With this simplification, the derivative (4.17) yields:

$$\rho_0 c_0 \left[\frac{(1-\psi)[1+(s-\gamma_0)\psi]}{(1-s\psi)^3} \right] = K_0 f_{K1}(\psi), \quad \psi > 0 \quad (4.18a)$$

$$\rho_0 c_0 (1-\psi)(1-\gamma_0\psi) = K_0 f_{K1}(\psi), \quad \psi \leq 0 \quad (4.18b)$$

Highly different constitutive models for the shear modulus for highly compressed solids have been proposed by Steinberg *et al.* (1980), and Rubin (1987). Alternatively, considering the lack of experimental data it is reasonable to assume that the shear modulus changes with respect to volume strain in the same manner as the bulk modulus (Johnson *et al.* 1991 and Lipkin *et al.* 1977), i.e.,

$$f_{\mu 1}(\psi) = f_{k 1}(\psi), \quad (4.19)$$

where

$$\mu_0 = \frac{3(1-2\nu)}{2(1+\nu)} K_0 \quad (4.20)$$

and ν is the Poisson ration.

The effect of microvoid damage in degrading the elastic moduli can be described by the well known hollow sphere proposed Mackenzie (1957), and subsequently modified by Johnson (1981), according to which

$$f_{k 2}(\xi) = \left[\frac{4\mu_0(1-\xi)}{4\mu_0 + 3K_0\xi} \right] \quad (4.21)$$

$$f_{\nu 2}(\xi) = \left[(1-\xi) \left(1 - \frac{6K_0 + 12\mu_0}{9K_0 + 8\mu_0} \xi \right) \right] \quad (4.22)$$

When $\xi=0$, Eqs. (4.21) and (4.22) reduce to unity, and for $\xi=1$, (i.e. $\nu_v = \nu$) they reduce to zero.

The temperature variation of the bulk and shear moduli at temperatures above room temperature are known to be linear, or near linear, respectively, with the shear modulus reducing to zero at melt temperature (Steinberg et al. 1980, Huntington 1958 and Lakkad 1971). Thus

$$f_{3K} = \left[1 - a_2 \left(\frac{T}{T_0} - 1 \right) \right] \quad (4.23)$$

$$f_{\mu} = \left[1 - \left(\frac{T - T_0}{T_m - T_0} \right)^b \right] \quad (4.24)$$

where a_2 and β are material constants, T_0 is the temperature at which the modulus K_0 or μ_0 are measured and T_m is the melt temperature of the material. The variation of the melt temperature with large volume reduction can be calculated according to the model proposed by Steinberg *et al.* (1980),

$$T_m = T_{m0} \exp(2a_1\psi) \left(\frac{1}{1-\psi}\right)^{\beta(\gamma_0 - a_1 - \chi)} \quad , \psi > 0. \quad (4.25)$$

where T_{m0} is the melt temperature at zero volume strain and a_1 is a material parameter.

The elastic moduli expressions (4.15) and (4.16) can now be given in explicit form, where for volume compression, $\psi > 0$

$$K = K_0 \left[\frac{(1-\psi)[1+(s-\gamma_0)\psi]}{(1-s\psi)^3} \right] \left[1 - a_2 \left(\frac{T}{T_0} - 1 \right) \right] \left[\frac{4\mu_0(1-\xi)}{4\mu_0 + 3K_0\xi} \right], \quad (4.26)$$

$$\mu = \mu_0 \left[\frac{(1-\psi)[1+(s-\gamma_0)\psi]}{(1-s\psi)^3} \right] \left[1 - \left(\frac{T-T_0}{T_m-T_0} \right)^\beta \right] \left[(1-\xi) \left(1 - \frac{6K_0 + 12\mu_0}{9K_0 + 8\mu_0} \xi \right) \right], \quad (4.27)$$

whereas for zero volume strain and dilatation, $\psi \leq 0$, the parameter s is set equal to zero in Equations (4.26) and (4.27). For high shock compression the microdamage contribution reduces essentially to unity, while for small dilatation the volume strain makes no significant contribution.

4.3 Viscoplastic Rate of Deformation

The plastic rate of deformation tensor can be decomposed in terms of its volumetric and deviatoric components,

$$D^p = \frac{1}{3} (\text{tr } D^p) \mathbf{1} + D'^p \quad (4.28)$$

where $\frac{1}{3}(\text{tr} \mathbf{D}^p) \mathbf{1}$ represents the dilatational rate of deformation tensor associated with void volume change, $\mathbf{1}$ is the identity tensor, \mathbf{D}^p is the deviatoric rate of plastic deformation tensor.

To define the volumetric plastic rate of deformation an increment of dilatational microvoid volume strain defined by $-dv_v = (1/v_v)dv$ leads to the logarithmic expression,

$$\psi_v = -\ln\left(\frac{1-\xi_0}{1-\xi}\right); \quad (4.29)$$

where ψ_v represents the volume strain associated with void volume fraction change and

$\xi = v_v/v$ represents void volume fraction.

It can be shown by using the continuity Equation (4.1) and Equation (4.29) that,

$$\frac{1}{3}(\text{tr} \mathbf{D}^p) \mathbf{1} = \frac{1}{3} \left(\frac{\dot{\psi}_v}{1-\psi_v} \right) \mathbf{1} = \left\{ \frac{\dot{\xi}}{3(1-\xi)[1 + \ln(1-\xi_0/1-\xi)]} \right\} \mathbf{1}. \quad (4.30)$$

The constitutive model that describes the deviatoric viscoplastic response of the material at high strain rate is based on the work by Perzyna (1986),

$$\mathbf{D}^p = \frac{1}{\eta} \Phi(\hat{F}) \frac{\partial J'_2}{\partial \mathbf{T}} = \frac{1}{\eta} \left(\frac{J'_2}{\kappa} - 1 \right)^{m_1} \mathbf{T}', \quad (4.31)$$

where the yield condition requires that

$$\hat{F} = \frac{J'_2}{\kappa} - 1 > 0. \quad (4.32)$$

The stress deviator invariant $J'_2 = \frac{1}{2} \text{tr}(\mathbf{T}' \cdot \mathbf{T}')$, η is the material viscosity and κ is a yield function based on the Johnson-Cook model (Johnson *et al.* 1983), but with the addition of

a damage softening term to reflect the deterioration of the yield stress as the void volume fraction increases,

$$\kappa(\epsilon^p, \dot{\epsilon}^p, T, \xi) = \left\{ \left[C_1 + C_2 (\epsilon^p)^n \right] \left[1 + C_3 \ln \left(\frac{\dot{\epsilon}^p}{\dot{\epsilon}_0} \right) \right] \left[1 - \left(\frac{T - T_0}{T_m - T_0} \right)^\beta \right] \left[1 - \left(\frac{\xi - \xi_0}{\xi_F - \xi_0} \right) \right] \right\}^2 \quad (4.33)$$

ϵ^p is the equivalent plastic strain, $\dot{\epsilon}^p$ the equivalent plastic strain rate, $\dot{\epsilon}_0 = 1.0 \text{ s}^{-1}$, T_m is the melt temperature, ξ the current void volume fraction, ξ_0 the initial void volume fraction, ξ_F the critical void volume fraction at which the material locally fractures, and C_1 , C_2 , C_3 , n and β are material parameters. The term $\left[C_1 + C_2 (\epsilon^p)^n \right]$ describes the nonlinear isotropic strain hardening characteristics of the material; term $\left[1 + C_3 \ln \left(\frac{\dot{\epsilon}^p}{\dot{\epsilon}_0} \right) \right]$ incorporates strain rate effect; and term $\left[1 - \left(\frac{T - T_0}{T_m - T_0} \right)^\beta \right]$ defines the thermal softening characteristics of the material. When $T = T_m$ the thermal softening effect reduces the equivalent yield stress to zero. The last term, $\left[1 - \left(\frac{\xi - \xi_0}{\xi_F - \xi_0} \right) \right]$ defines the damage softening effects associated with the presence of microvoids. When $\xi = \xi_F$, the damage softening effect reduces the equivalent yield stress to zero.

Experimental data is limited and considerable discrepancy exists in the reported values of material viscosity. Various shock experiments have shown that material viscosity can be influenced by temperature (Carroll *et al.* 1986), strain rate (Sweogle *et al.* 1985) and mean stress. A model proposed by Carroll *et al.* (1986) assumed an exponential form of the temperature variation of viscosity for high strain rates.

Chhabildas *et al.* (1979) extracted material viscosity values for various materials under high shock compression and elevated temperature from measurements of shock rise time. The model used in the present work assumes that the lower bound value for the viscosity at melt temperature remains constant at $\eta \approx 10^{-2}$ Poise (Carroll *et al.* 1986),

$$\eta = \eta_0 \exp\left(-\ln\left(\frac{\eta_0}{\eta_m}\right)\left(\frac{T - T_0}{T_m(\psi) - T_0}\right)\right), \quad \psi > 0, T \leq T_m \quad (4.34a)$$

$$\eta = \eta_0 \exp\left(-\ln\left(\frac{\eta_0}{\eta_m}\right)\left(\frac{T - T_0}{T_{m0} - T_0}\right)\right), \quad \psi \leq 0, T \leq T_m \quad (4.34b)$$

where η_0 is the viscosity at the reference temperature (room temperature) and high strain rate of deformation i.e. 10^6 - 10^8 s^{-1} , η_m is the viscosity at melt temperature (Figure 4.1).

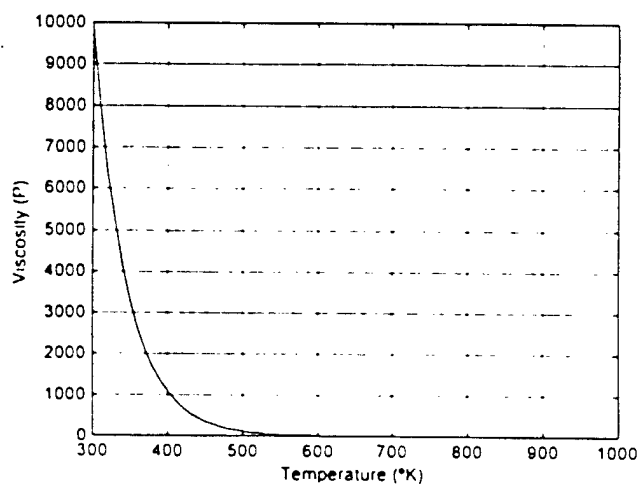


Figure 4.1 Viscosity as a function of temperature for Aluminum applicable to high strain rates ($\eta_0=10^4$ P, $\eta_m=10^{-2}$ P and $T_m=923$ °K) (Mineev *et al.* 1997).

Combining Equations (4.28), (4.30) and (4.31), the plastic rate of deformation tensor can be expressed as,

$$\mathbf{D}^p = \frac{1}{\eta(T)} \left\{ \frac{J_2'}{\kappa(\varepsilon^p, \dot{\varepsilon}^p, T, \xi)} - 1 \right\}^{m_1} \mathbf{T}' + \left\{ \frac{\xi}{3(1-\xi)[1 + \ln(1-\xi_0/1-\xi)]} \right\} \mathbf{1}. \quad (4.35)$$

This equation differs from the one proposed by Perzyna (1986) in that the volumetric and deviatoric components are not explicitly coupled. In the form proposed by Perzyna the constitutive model gives a non-zero value to the volumetric contribution from microvoid growth even when the microvoid volume rate of change is zero. This problem is corrected by using the form presented in Equation (4.35). It should be noted that Equation (4.35) applies only for temperatures below the melt temperature. The equivalent plastic strain is defined as (Malvern 1969),

$$\varepsilon^p = \int_0^t 2/\sqrt{3} \left| (\text{II}_{\mathbf{D}^p})^{1/2} \right| dt, \quad \text{II}_{\mathbf{D}} = \frac{1}{2} \left[(\text{tr } \mathbf{D}^p)^2 - \text{tr}(\mathbf{D}^p \cdot \mathbf{D}^p) \right] \quad (4.36)$$

At melt temperature $T=T_m$ and/or at the critical void volume fraction $\xi=\xi_F$, it follows from (4.33) that $\kappa \rightarrow 0$ so that

$$\mathbf{D}^p \Big|_{\substack{T=T_m \\ \xi=\xi_F}} \rightarrow \infty \quad (4.37)$$

represents the condition for local failure, i.e., the material loses its capacity to resist load.

4.4 Microdamage Evolution

At the microstructural level, all polycrystalline solids fracture by the nucleation, growth, and coalescence of voids (pores) and cracks (Curran *et al.* 1987). Because of the elevated temperatures associated with hypervelocity impact only the ductile failure mode

associated with nucleation, growth and coalescence of voids (Johnson 1981) is considered.

Some of the first models developed to predict porosity changes of a material subjected to high shock compression were developed by Carroll *et al.* (1972). Their development included the idealization of a void as a spherical hole inside a matrix of solid material. From this initial study, the model has been improved by several authors (Johnson 1981, Carroll 1985 and 1986, Perzyna 1986, and Eftis 1991, 1992 and 1996 amongst others). The development of the micro-damage model presented in this dissertation improves upon the previous models in several ways that will be discussed as the model is presented.

The presence of microvoids in polycrystalline materials in the as-produced state has been documented in many research and review articles (Curran *et al.* 1987). These microvoids can vary in size from 10^{-2} -to 10^{-5} cm, with an average density of the order of 10^6 per cm^3 and an average initial void volume fraction between 10^{-3} - 10^{-4} (Eftis 1996). In addition, it has been demonstrated experimentally that it is the growth of this initial density of microvoids in combination with the nucleation and growth of new microvoids that eventually leads to the formation of ductile cracks and spallation or fracture of the material. Figure 4.2 illustrates the final effect of this microdamage process. The nucleation process is dependent on the number and character of the nucleation sites that are available in the crystalline material. In general, the nucleation of voids occur at microscopic heterogeneities in the material like preexisting flaws, inclusions and second phase particles, grain boundaries and subgrain structures (Curran *et al.* 1987). Figure 4.3

is evidence that inclusions in the material can serve as nucleation sites. In this figure the inclusions are still observable inside the voids that have grown to many times their initial diameters.

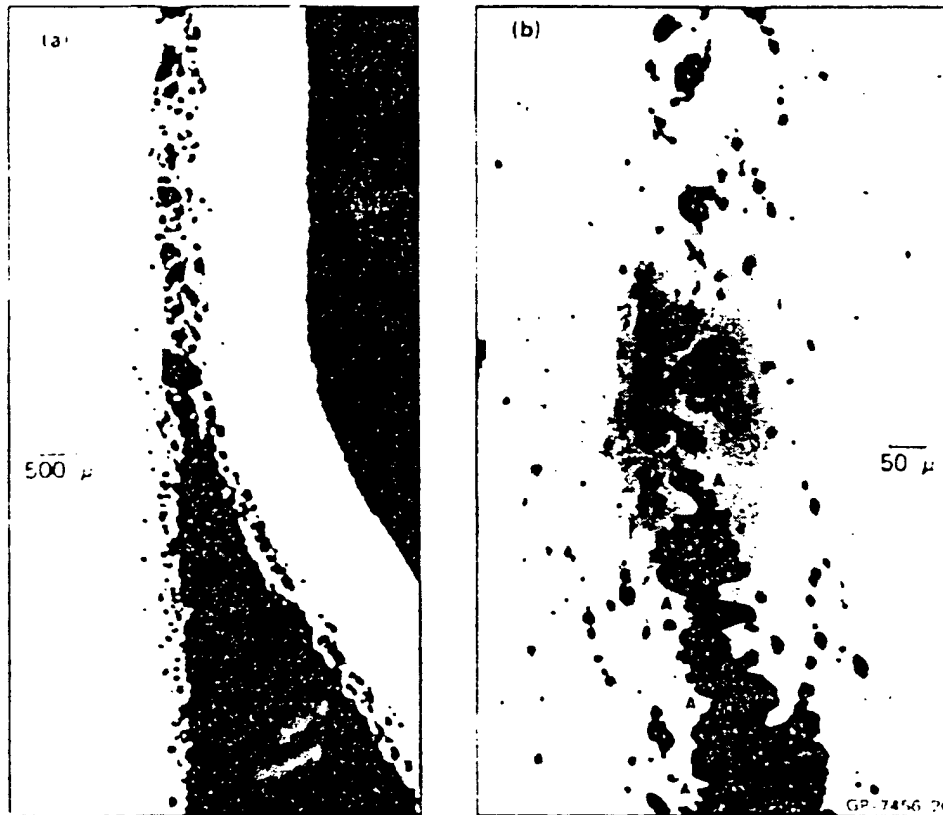


Figure 4.2 Ductile cracks. (a) Ductile crack propagation by void coalescence; (b) Tip of ductile crack shown in (a) at higher magnification (Curran *et al.* 1987).

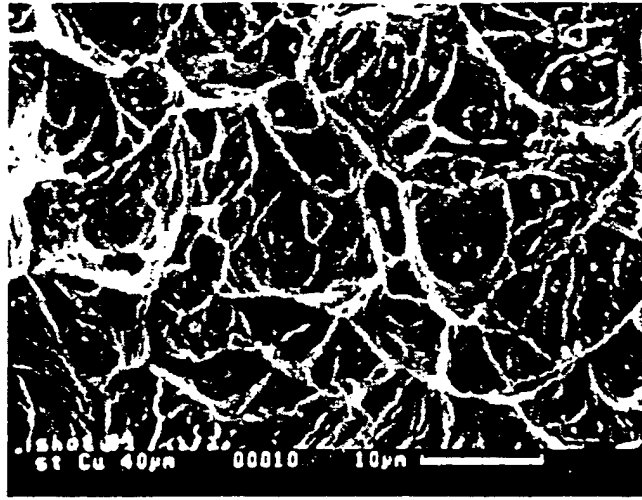


Figure 4.3 Fracture surface of ETP Copper (Zurek *et al.* 1996).

4.4.1 Microvoid Nucleation Rate

The model used for the simulation of void nucleation has its origin in the form proposed by Seaman *et al.* (1976). Perzyna (1986) further modified this model to an activation-rate form, which also makes provision for the effect of void interaction during the nucleation process, so that the void nucleation rate model has the form

$$\dot{\xi}_n = \frac{h}{1 - \xi} \left[\exp\left(\frac{m_2 |\sigma_m - \sigma_n|}{kT}\right) - 1 \right], \quad \sigma < \sigma_n. \quad (4.38)$$

In the above, $m_2 |\sigma - \sigma_n|$ is the nucleation activation energy, σ_m is the mean stress, σ_n is the threshold mean stress for nucleation, T is the temperature, k is the Boltzmann constant and m_2 are material parameters and h simulates the effect of void interaction. The void nucleation contribution to the total void volume fraction, given by the time integration of Equation (4.38), has a limiting value, i.e., $\xi_n \leq \xi_{nm}$. This limit is controlled by the number of nucleation sites available in the material in the form of heterogeneities (Curran

et al. 1987). The values for the nucleation threshold stress found in high velocity impact literature are mostly obtained from high velocity plate impact tests (Curran *et al.* 1987). The high shock compression associated with impact at hypervelocities can cause substantial strain hardening of the material, particularly at the impact sides of the target and projectile. This effect is indirectly exhibited by the higher nucleation thresholds for the harder metals, e.g., Ni-Cr-Steel, as compared to softer materials such as Copper or Aluminum, and may be expressed by assuming the microvoid threshold nucleation stress to be proportional to the current yield stress,

$$\sigma_n = \frac{\sigma_{n0}}{C_1} \left[C_1 + C_2 (\epsilon^p)^n \right] \left[1 + C_3 \ln \left(\frac{\dot{\epsilon}^p}{\dot{\epsilon}_0} \right) \right] \quad (4.39)$$

where σ_{n0} is the nucleation threshold determined by plate impact tests and the rest of the parameters are as defined in Equation (4.33). The nucleation threshold has the same functional form as the Johnson-Cook model for the equivalent yield stress, except that the temperature factor is excluded since the temperature dependence is already included in the void nucleation rate equation above. Several authors have implemented this model for nucleation but have used a constant nucleation threshold (Perzyna 1986, Eftis *et al.* 1991 and 1992, and Eftis 1996). Since most of the validation of the model was done with simulations of high velocity plate impact tests, the results that were obtained were acceptable. However, when a constant value for the threshold is used to simulate hypervelocity impact the nucleation model with constant nucleation threshold stress no longer gives acceptable results, and a variable threshold as described by Equation (4.39), is necessary.

4.4.2 Micro Void Growth Rate

The rate of change of the void volume fraction model is based on the idealized spherical hole described by Carroll *et al.* (1972). In their model they assumed that the yield stress of the material was constant (perfectly plastic material) and ignored thermal effects. The spherical void model was further developed by Johnson (1981) to include strain rate effects in the constitutive model of the material and was the first to infer that thermal effects might be important. The model was later improved by Carroll by studying the effects of several material isotropic hardening laws. Perzyna (1986) included linear strain hardening in addition to the rate effect. The linear hardening model proposed by Perzyna was proved unsatisfactory by Eftis *et al.* (1991, 1992) and was replaced by a saturation hardening model. Thermal effects were not included.

The development of the spherical void model is presented and includes several improvements over the models presented before. The derivation of the model begins by replacing the microvoids embedded in the material by a random distribution of spherical voids (Figure 4.4).

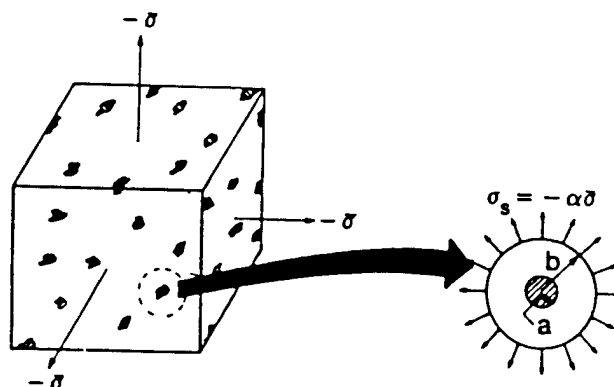


Figure 4.4 Element of the solid with microvoids replaced by idealized spherical voids (Eftis 1996).

If the rectangular volume of Figure 4.4 is subjected to the actions of mean stress $\bar{\sigma}(t)$ that varies with time, only the solid cross-sectional area will support the applied stress. The sectional area occupied by the voids does not support any stress. Thus, mechanical equilibrium requires that (from this point on the time dependence of the variables is implicit),

$$\bar{A}\bar{\sigma} = A\sigma \quad (4.40)$$

where \bar{A} is the total cross-sectional area (i.e., including the area of the microvoids), $\bar{\sigma}$ is the mean stress acting on \bar{A} , A is the solid portion of the cross-sectional and σ is the mean stress acting on the solid material with sectional area A . For a random distribution of voids shapes and sizes the following holds,

$$\frac{A}{\bar{A}} = \frac{v}{\bar{v}} \quad (4.41)$$

where v is the volume of solid material and \bar{v} is the total volume of material.

Substituting Equation (4.41) in (4.40),

$$\sigma = \alpha\bar{\sigma} \quad (4.42)$$

where, $\alpha = \frac{\bar{v}}{v}$ is defined as the void distension.

Considering an idealized void with spherical shape and radius a in a sphere of radius b where the outer boundary is subjected to mean stress σ (figure 4.5).

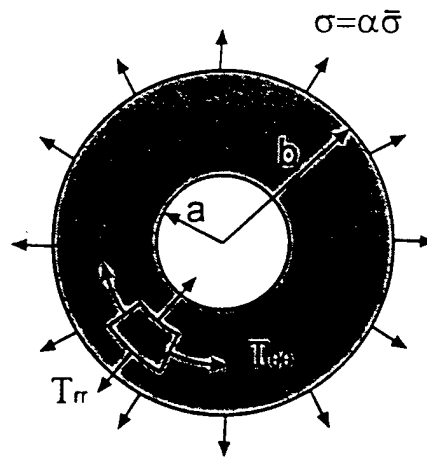


Figure 4.5 Idealized spherical void with average mean stress.

The equation of motion for the configuration shown in Figure 4.5 can be defined in spherical coordinates. Taking account of spherical symmetry,

$$\frac{\partial T_{rr}}{\partial r} + \frac{2}{r}(T_{rr} - T_{\theta\theta}) = \rho \ddot{r} \quad (4.43a)$$

The boundary conditions require

$$\begin{aligned} T_{rr}(a, t) &= 0 \\ T_{rr}(b, t) &= -\alpha \bar{\sigma} \end{aligned} \quad (4.43b)$$

where T_{rr} is the radial stress acting on a spherical differential element (Figure 4.5), $T_{\theta\theta}$ is the tangential stress, ρ is the density of the solid material, and \ddot{r} is the material radial acceleration. Making the assumption that nearly all the volume change is associated with void growth and very little with volume strain in the solid material surrounding the void,

$$r^3 = r_0^3 - B(t) \quad (4.44)$$

$$\alpha = \frac{b^3}{b^3 - a^3} \quad (4.45)$$

where $B(t)$ is a function related to the rate of void growth.

By means of Equation (4.44) the radius of any point that initially had radius r_0 can be determined. Differentiating Equation (4.44) twice with respect to time,

$$\ddot{r} = -\frac{\ddot{B}(t)}{3r^2} - \frac{2\dot{B}(t)^2}{9r^3} \quad (4.46)$$

Integrating Equation (4.43) from a to b (inner to outer current radius) and substituting Equation (4.46),

$$\rho[\Psi(b, t) - \Psi(a, t)] = \alpha \bar{\sigma} + \int_a^b \frac{2}{r} (T_{\pi} - T_{\infty}) dr \quad (4.47a)$$

where,

$$\Psi(r, t) = \frac{\ddot{B}(t)}{3r} + \frac{\dot{B}(t)^2}{18r^2} \quad (4.47b)$$

By means of Equations (4.44) and (4.45),

$$B(t) = a_0^3 \left[\frac{\alpha_0 - \alpha}{\alpha_0 - 1} \right] \quad (4.48)$$

where a_0 is the initial inner radius and $\alpha_0 = \frac{b_0^3}{b_0^3 - a_0^3}$ the initial void distension.

Substituting Equation (4.48) into (4.47) and rearranging terms,

$$\tau Q(\ddot{\alpha}, \dot{\alpha}, \alpha) = \alpha \bar{\sigma} + \int_a^b \frac{2}{r} (T_{\pi} - T_{\infty}) dr \quad (4.49a)$$

where

$$\tau = \frac{\rho a_0^2}{3(\alpha_0 - 1)^{2/3}} \quad (4.49b)$$

and

$$Q(\ddot{\alpha}, \dot{\alpha}, \alpha) = [(\alpha - 1)^{-1/3} - \alpha^{-1/3}] \ddot{\alpha} - \frac{1}{6} [(\alpha - 1)^{-4/3} - \alpha^{-4/3}] \dot{\alpha}^2. \quad (4.49c)$$

At this point, a constitutive model for the material surrounding the void has to be introduced to completely define Equation (4.49). It can be shown that the elastic and elastic-plastic phases of the deformation of the material surrounding the void produce a very small volume change compared to the plastic deformation contribution. For this reason, as an approximation, void growth is going to be modeled as a fully plastic process (Johnson 1981). In other words, void growth is only going to occur when all the gray area shown on Figure 4.5 has yielded. The yield function Y used for the constitutive model has a form similar to the modified Johnson-Cook model shown in Equation (4.33) but without the damage softening effect and with the strain rate effect as an additive term.

$$Y_r(\epsilon^p, \dot{\epsilon}^p, T, r) = -\frac{1}{\sqrt{3}}(T_r - T_{00}) = \pm [C_1 + C_2(\dot{\epsilon}^p)^n] \left[1 - \left(\frac{T(r) - T_0}{T_m - T_0} \right)^\beta \right] \pm \eta(T(r)) \dot{\epsilon}^p \quad (4.50)$$

where $\eta(T(r))$ is the temperature dependant viscosity at any radius of the material surrounding the spherical void. The negative sign in the difference of stresses term comes from the fact that when the applied mean stress ($\bar{\sigma}$) is positive, the difference between the radial and tangential stresses is negative (Malvern 1969). The \pm sign

indicates that the yield stress is positive when the mean stress is positive and negative when the mean stress is negative.

In applications of the microvoid growth model for description of spall fracture induced by plate impact (Johnson 1981 and Eftis *et al.* 1991) it was found that the numerical simulations would correlate with experimental data only if the viscosity of the solid material surrounding the void has a value of approximately 10 Poise, three to four orders of magnitude smaller than room temperature values. It was suggested that the large shear strains at the pore wall cause temperature increase close to melt temperatures, thereby greatly reducing the viscosity of the surrounding material. The variation of the viscosity with temperature is given by Equation (4.34), with the melt temperature $T_m = T_{m0}$, i.e., the value at zero volume strain (Equation 4.44).

To simplify the integration of Equation (4.50) when substituted into (4.49a), the absolute temperature used in Equation (4.50) is taken at a fixed radius $\bar{r}(t)$ in the vicinity of the inner radius (a).

$$\bar{r}(t) = a + q(b - a), \quad 0 < q < 1. \quad (4.51)$$

If $q=0$ then $\bar{r}(t)$ is the inner radius (a), and if $q=1$ then $\bar{r}(t)$ represents the outer radius (b).

Substitution of Equation (4.51) into (4.50) eliminates the radial dependence of the temperature and implicitly of the viscosity as well. Thus

$$Y(\dot{\epsilon}^p, \dot{\epsilon}^p, \bar{T}) = -\frac{1}{\sqrt{3}}(T_m - T_{\infty}) = \pm \left[C_1 + C_2 (\dot{\epsilon}^p)^p \right] \left[1 - \left(\frac{\bar{T} - T_0}{T_m - T_0} \right)^\beta \right] \pm \eta(\bar{T}) \dot{\epsilon}^p \quad (4.52)$$

where \bar{T} is the temperature at radius \bar{r} .

From Equation (4.44) the radial displacement can be calculated to be

$$u_r = r - r_0 = r - [r^3 + B(t)]^{1/3} \quad (4.53)$$

and for small displacements and strains, the small strain tensor in spherical coordinates and with radial symmetry has the matrix representation

$$E^p = \begin{bmatrix} \frac{\partial u_r}{\partial r} & 0 & 0 \\ 0 & \frac{1}{r} u_r & 0 \\ 0 & 0 & \frac{1}{r} u_r \end{bmatrix}. \quad (4.54)$$

The equivalent plastic strain is given by (Malvern 1969),

$$\epsilon^p = \frac{\sqrt{2}}{3} \left[(E_{rr}^p - E_{\theta\theta}^p)^2 + (E_{rr}^p - E_{\phi\phi}^p)^2 \right]^{1/2} \quad (4.55a)$$

which reduces to

$$\epsilon^p = \frac{2}{3} \left| \frac{u_r}{r} - \frac{\partial u_r}{\partial r} \right|. \quad (4.55b)$$

The equivalent plastic strain rate is

$$\dot{\epsilon}^p = \frac{d}{dt} \left(\frac{2}{3} \left| \frac{u_r}{r} - \frac{\partial u_r}{\partial r} \right| \right). \quad (4.56)$$

The integral that appears on the right hand side of Equation (4.49a), after substitution of Equations (4.55), (4.56) and (4.53) in Equation (4.52), is not developed here because it is a lengthy calculation. Only the final result is shown,

$$\int_{r_0}^r 2(T_{rr} - T_{\theta\theta}) dr = \frac{2\sqrt{3}}{3} \left[C_1 \ln \left(\frac{\alpha}{\alpha-1} \right) - \left(\frac{2}{3} \right)^n C_2 \bar{I}(\alpha) \right] f(\bar{T}) + \frac{4}{3\sqrt{3}} \eta(\bar{T}) \left| \frac{\dot{\alpha}}{\alpha(\alpha-1)} \bar{F}(\alpha) \right| \quad (4.57a)$$

where

$$\bar{I}(\alpha) = \int_{B(t)/a}^{B(t)/b} \frac{1}{\chi} |\chi(1+\chi)^{-2/3}|^n d\chi \quad (4.57b)$$

$$f(\bar{T}) = \left[1 - \left(\frac{\bar{T} - T_0}{T_m - T_0} \right)^\beta \right] \quad (4.57c)$$

and

$$\bar{F} = \alpha \left[\frac{\alpha - 1}{\alpha_0 - 1} \right]^{2/3} - (\alpha - 1) \left[\frac{\alpha}{\alpha_0} \right]^{2/3} \quad (4.57d)$$

The integral in Equation (4.57b) is non-elementary and has to be solved numerically.

The substitution of Equation (4.57) in Equation (4.49) gives,

$$\tau_Q(\ddot{\alpha}, \dot{\alpha}, \alpha) = (\alpha \bar{\sigma}) \mp \frac{2\sqrt{3}}{3} \left[C_1 \ln \left(\frac{\alpha}{\alpha - 1} \right) - \left(\frac{2}{3} \right)^n C_2 \bar{I}(\alpha) \right] f(\bar{T}) \mp \frac{4}{3\sqrt{3}} \eta(\bar{T}) \left| \frac{\dot{\alpha}}{\alpha(\alpha - 1)} \bar{F}(\alpha) \right| \quad (4.58)$$

If we take the limit of Equation (4.58) as $\dot{\alpha}$ and $\ddot{\alpha}$ approach zero,

$$\bar{\sigma}_G = \pm \left(\frac{1}{\alpha} \right) \frac{2\sqrt{3}}{3} \left[C_1 \ln \left(\frac{\alpha}{\alpha - 1} \right) - \left(\frac{2}{3} \right)^n C_2 \bar{I}(\alpha) \right] f(\bar{T}) \quad (4.59)$$

Which represents the threshold mean stress for void growth (+), or void volume reduction (-), and includes the power isotropic hardening and the thermal softening. Once the externally applied mean stress ($\bar{\sigma}$) reaches the threshold ($\bar{\sigma}_G$) the spherical void begins to grow or shrink.

Substituting Equation (4.59) into (4.57),

$$\tau_Q(\ddot{\alpha}, \dot{\alpha}, \alpha) = \alpha (\bar{\sigma} - \bar{\sigma}_G) \mp \frac{4}{3\sqrt{3}} \eta(\bar{T}) \left| \frac{\dot{\alpha}}{\alpha(\alpha - 1)} \bar{F}(\alpha) \right| \quad (4.60)$$

To express Equation (4.60) in terms of the void volume fraction (ξ) instead of void distension (α), the following relation can be derived from the definitions of ξ and α mentioned above,

$$\alpha = \frac{1}{1-\xi} \quad (4.61a)$$

Differentiating,

$$\dot{\alpha} = \frac{\dot{\xi}}{(1-\xi)^2} \quad (4.61b)$$

$$\ddot{\alpha} = \frac{2\dot{\xi}^2}{(1-\xi)^3} + \frac{\ddot{\xi}}{(1-\xi)^2} \quad (4.61c)$$

Then substituting Equations (4.61) into (4.60) and arranging terms,

$$\tau(A_1 \ddot{\xi} + B_1 \dot{\xi}^2) \pm \eta(\bar{T}) \dot{\xi} F(\xi) = (\bar{\sigma} - \bar{\sigma}_G) \quad (4.62)$$

where,

$$A_1 = \left[\frac{(\xi^{-1/3} - 1)}{(1-\xi)^{2/3}} \right] \quad (4.63)$$

$$B_1 = \left[\frac{2(\xi^{-1/3} - 1)}{(1-\xi)^{5/3}} - \frac{1}{6} \frac{(\xi^{-4/3} - 1)}{(1-\xi)^{5/3}} \right] \quad (4.64)$$

$$\tau = \frac{\rho a_0^2}{3} \left(\frac{1-\xi_0}{\xi_0} \right)^{2/3}, \quad a_0 \cong 10^{-4} \text{ cm} \quad (4.65)$$

$$F(\xi) = \left(\frac{1-\xi_0}{1-\xi} \right)^{2/3} \left[\frac{1}{\xi} \left(\frac{\xi}{\xi_0} \right)^{2/3} - 1 \right] \quad (4.66)$$

$$\bar{\sigma}_G = \pm(1-\xi) \frac{2}{\sqrt{3}} \left[C_1 \ln\left(\frac{1}{\xi}\right) - \left(\frac{2}{3}\right)^n C_2 I(\xi) \right] f_T(\bar{T}) \quad (4.67)$$

$$I(\xi) = \int_{B(t)/a^3}^{B(t)/b^3} \frac{1}{\chi} \left| \chi(1+\chi)^{-2/3} \right|^n d\chi \quad (4.68a)$$

$$\frac{B(t)}{a^3} = \frac{1}{\xi} \left(\frac{\xi_0 - \xi}{1 - \xi_0} \right) \quad (4.68b)$$

$$\frac{B(t)}{b^3} = \left(\frac{\xi_0 - \xi}{1 - \xi_0} \right) \quad (4.68c)$$

The term $\tau(A_1 \ddot{\xi} + B_1 \dot{\xi}^2)$ represents the inertial resistance to microvoid volume change, $\eta(\bar{T}) \dot{\xi} F(\xi)$ the viscous material resistance to plastic flow and $(\bar{\sigma} - \bar{\sigma}_G)$ the mean stress difference that drives the void growth.

As voids grow in the material, they initially grow independently. However, in the later stages before fracture, they begin to interact. First, their plastic strain fields intersect and then a stronger interaction takes place (Curran *et al.* 1987). It is this interaction that represents the final stage of failure of the material. Eftis *et al.* (1991) proposed a modification to the void growth Equation that would take void interaction into account as the growth process progresses. This is done by the inclusion of an exponential function in Equation (4.62),

$$\tau(A_1 \ddot{\xi} + B_1 \dot{\xi}^2) \pm \eta(\bar{T}) \dot{\xi} F(\xi) = e^{\alpha \xi} (\bar{\sigma} - \bar{\sigma}_G), \quad \dot{\xi} > 0 \quad (4.69a)$$

$$\tau(A_1 \ddot{\xi} + B_1 \dot{\xi}^2) \pm \eta(\bar{T}) \dot{\xi} F(\xi) = (\bar{\sigma} - \bar{\sigma}_G), \quad \dot{\xi} \leq 0 \quad (4.69b)$$

where ϕ is a material parameter. Equation (4.69b) differs from (4.69a) in that it does not include the coalescence effect since under void volume reduction there is no coalescence effect of the microvoids.

The microvoid nucleation rate $\dot{\xi}_n$ given by Equation. (4.38), when added to the solution of the Equation (4.69) for the void growth rate $\dot{\xi}_g$, provides the total microvoid rate of change,

$$\dot{\xi} = \dot{\xi}_n + \dot{\xi}_g \quad (4.70)$$

Under mean-stress tensile loading microvoid nucleation and growth will continue until it reaches the critical value ξ_F and material fracture occurs ξ_F .

4.4.3 Temperature Near the Wall of a Microvoid

The temperature change in the vicinity of the walls of a microvoid (hollow sphere) is governed by the plastic rate of mechanical work,

$$\rho C_v \dot{T} = \omega \text{tr}(\mathbf{T}' \cdot \mathbf{D}^p) \quad (4.71)$$

where C_v is the specific heat at constant volume, and ω gives the percentage of the rate of plastic work that is not stores as cold work, i.e., that dissipates into heat. For polycrystalline materials $\omega \approx 0.9$. In view of the spherical symmetry only the radial component of \mathbf{T}' and \mathbf{D}^p are non-zero so that

$$\text{tr}(\mathbf{T}' \cdot \mathbf{D}^p) = T'_r \cdot D^p_r \quad (4.72)$$

where

$$T'_n = \frac{2}{3}(T_n - T_{\infty}) \quad (4.73)$$

$$D_n^p = \frac{2}{3} \frac{\dot{B}(t)}{\bar{r}^3} \quad (4.74)$$

and by using the simplification proposed by Equation (4.51) it can be shown that

$$(T_n - T_{\infty}) = \pm \sqrt{3} \left[C_1 + C_2 (\bar{\epsilon}^p)^n \right] \left[1 - \left(\frac{\bar{T} - T_0}{T_m - T_0} \right)^\beta \right] \pm \eta(\bar{T}) \dot{\bar{\epsilon}}^p \quad (4.75)$$

Further omitting the detailed calculations it can be shown that

$$\bar{\epsilon}^p = \frac{2}{3} \left| - \left[1 + \frac{B(t)}{\bar{r}^3} \right]^{1/3} + \left[1 + \frac{B(t)}{\bar{r}^3} \right]^{-2/3} \right| \quad (4.76)$$

$$\dot{\bar{\epsilon}}^p = -\frac{2}{3} \frac{\dot{B}(t)}{\bar{r}^3} \left\{ \frac{1}{3} \left[1 + \frac{B(t)}{\bar{r}^3} \right]^{-2/3} + \frac{2}{3} \left[1 + \frac{B(t)}{\bar{r}^3} \right]^{-5/3} \right\} \quad (4.77)$$

$$\frac{B(t)}{\bar{r}^3} = \frac{(\xi_0 - \xi)}{\xi(1 - \xi_0)} \frac{1}{\varphi(\xi)} \quad (4.78)$$

$$\frac{\dot{B}(t)}{\bar{r}^3} = -\frac{\dot{\xi}}{\xi(1 - \xi)} \frac{1}{\varphi(\xi)} \quad (4.79)$$

and

$$\varphi(\xi) = \left\{ 1 + q \left[\left(\frac{1}{\xi} \right)^{1/3} - 1 \right] \right\}^3 \quad (4.80)$$

From Equations (4.72)-(4.74) expression (4.71) can be reduced to

$$\rho C_n \dot{\bar{T}} = \omega \frac{4}{9} (T_n - T_{\infty}) \frac{\dot{B}(t)}{\bar{r}^3} \quad (4.81)$$

Equation (4.81) represents the temperature rate at any radius that is a fraction (q), between the inner and outer radius of the void. The temperature calculated through the integration of Equation (4.81) gives the temperature used in Equation (4.69a) for the temperature dependant viscosity and in the temperature-softening factor (Equation 4.57c) applied to the growth threshold mean-stress in Equation (4.67). This void temperature calculation provides analytical justification for the reduced temperature-independent viscosity used by Johnson (1981) and Eftis *et al.* (1991), and represents an important improvement over the previous models.

Combining expressions (4.75) to (4.81) the temperature rate at some location in the vicinity of the inner pore wall can be expressed by

$$\dot{T} = \frac{4\omega}{9\rho C_v} \sqrt{3J'_2} \frac{\xi}{\xi(1-\xi) \left\{ 1 + q \left[\left(\frac{1}{\xi} \right)^{1/3} - 1 \right] \right\}^3} \quad (4.82)$$

where

$$J'_2 = \frac{1}{3} (T_n - T_{\infty})^2 \quad (4.83)$$

represents the second invariant of the stress deviator tensor, the equivalent of which can be calculated by using Equations (4.75)-(4.79), and where $0 \leq q \leq 1$. Equation (4.82) makes explicit the fact that the thermal heating near the wall of the microvoid is caused by the shear stress and plastic rate of change of the microvoid volume fraction.

4.5 Equations for Internal Energy and Temperature Rates

Due to the rapidity of the deformation following hypervelocity impact, the deformation and fracture processes develop under adiabatic conditions. In addition, if we

consider that there are no external heat sources, then the local energy rate balance Equation (4.4) simplifies to

$$\rho \dot{E} = \text{tr}(\mathbf{T} \cdot \mathbf{D}) \quad (4.84)$$

This expression can be developed further by decomposing the stress and rate of deformation tensors into deviatoric and mean (or volumetric) components, making use of (4.5) and the relation

$$\text{tr} \mathbf{D}^e = -\frac{\dot{\psi}}{1-\psi}. \quad (4.85)$$

It follows that

$$\rho \dot{E} = -\sigma_m \frac{\dot{\psi}}{1-\psi} + \text{tr}(\mathbf{T} \cdot \mathbf{D}^e) + \text{tr}(\mathbf{T} \cdot \mathbf{D}^p). \quad (4.86)$$

where the mean stress is given by Equations (4.13) and (4.14). If we specifically consider the internal energy as thermal energy, then $\rho \dot{E} = \rho C_v \dot{T}$. Since small elastic shear deformation does not cause temperature change, $\text{tr}(\mathbf{T} \cdot \mathbf{D}^e) = 0$. In as much as elastic volume reduction increases temperature while elastic dilatation causes temperature reduction, consistency requires $-\sigma_m$ to be replaced by $|\sigma_m|$. Taking account of the fact that only a fraction, ω , of the plastic work dissipates into heat. Where $\omega \approx 0.9$ for polycrystalline metals, we have the local temperature rate.

$$\rho C_v \dot{T} = |\sigma_m| \frac{\dot{\psi}}{1-\psi} + \omega \text{tr}(\mathbf{T} \cdot \mathbf{D}^p). \quad (4.87)$$

CHAPTER 5

NUMERICAL IMPLEMENTATION OF THE CONSTITUTIVE MODEL

The set of coupled, highly non linear equations described in chapters two, three and four cannot be solved analytically, unless simplifications of the constitutive model are introduced. For this reason numerical solution of the conservation equations and constitutive model represents the only viable approach.

Historically, the computer programs used in the simulation of shock deformation problems have been called "Hydrocodes". This name was used because in the initial development these computer codes used a hydrodynamic material model to simulate solid materials, i.e., where the stress and strain fields are assumed to have no deviatoric components (Johnson *et al.* 1987). One of the justifications for this type of simplification was the fact that the shock stresses are considerably larger than the dynamic yield stress of the material. After recognition that deviatoric effects were important in the simulation of initiation and expansion of the detonation products of high explosives, Wilkins *et al.* (1974) developed the procedure to incorporate deviatoric stress effects into computer codes. Since then, a great volume of work has been done directed towards the improvement of the numerical schemes used to solve the differential equations that define shock-induced deformation problems.

Currently there are several "Hydrocodes" produced by government and private organizations. The codes most widely used for the simulation of hypervelocity impact problems are, Dyna2D and 3D produced by the Lawrence Livermore National

Laboratory, CTH produced by Sandia National Laboratory, EPIC-2 and 3 and Autodyn2DTM and 3DTM produced by Century Dynamics Inc.

For the purpose of selecting a "Hydrocode" to implement the constitutive model, evaluations of CTH, Dyna2D and Autodyn2DTM were performed based on their capabilities and ease of implementation of new constitutive models. Of the three codes, Autodyn2DTM was selected because it has a user-friendly interface, includes the capability of running simulations with Lagrangian and/or Eulerian grids, and has the built in capability of compiling external functions to implement new constitutive models. Even though the capability to include external functions was an important factor in the selection of the code, in the end, that capability was not used because the constitutive model described in this dissertation is too complicated to be implemented just through external functions. Century Dynamics Inc., the originators of Autodyn, provided access to some of the internal subroutines that needed to be modified to successfully implement the model. Because of copyright restrictions, a thorough description of the subroutines that were modified cannot be published.

Although the equations described in the previous chapters describe a continuum, the computer code has to use a discretized version of the equations. This discretization is applied both in space and in time. The finite element method (FEM) and the finite difference method (FDM) are the methods of discretization in space. In "Hydrocodes" the time integration is done through an explicit central difference scheme in which the time derivatives are replaced by difference equations where the value of the function at the new time step is only a function of the value in the previous time step.

Once the discretized form of the equations is obtained, they have to be structured within the framework of a computer code. Most of the codes available today are based on the work by Wilkins *et al.* (1974), with minor modifications. He described how the discretized form of the equations had to be obtained and the numerical scheme that had to be used to advance the simultaneous solution of the equations in time at every time increment.

5.1 Numerical Simplifications

Because the solution of the set of field and constitutive equations is framed around a pre-established numerical scheme that is the foundation of every computer code, the inclusion of a given set of constitutive equation has to adapt to the established scheme. It would be desirable to be able to implement any constitutive model with no restrictions, but that is not possible.

During the implementation and testing of the constitutive equations in the Autodyn™ code, a series of difficulties were encountered. These difficulties restricted the implementation of the equations and a series of modifications had to be applied to make the simulations feasible.

5.1.1 Modifications to the Viscoplastic Constitutive Model

The viscoplastic constitutive model presented in Section 4.3 of the dissertation was not implemented in the original form because it required modifications of sections of the code to which we did not have access. For this reason, the calculation of the

equivalent plastic strain as described in Equation (4.36) was not used and the calculation already implemented in Autodyn™ was used with some modifications (Autodyn™ Theory Manual).

The viscoplastic constitutive model in Autodyn™ takes the form described by Wilkins *et al.* (1974) with the additional consideration that the model has to take into account the volume compressibility of the material due to the presence of microvoids that can grow or reduce in size.

The constitutive model that describes the deviatoric viscoplastic response of the material is based on the von Mises yield criteria, which can be stated as follows.

$$J_2 = \frac{Y^2}{3} \quad (5.1)$$

where J_2 is the second invariant of the stress deviator tensor and Y is the equivalent yield stress. Thus, when $J_2 \leq Y^2/3$ the material is in an elastic state of stress, and when

$J_2 > Y^2/3$ the material is in a state of plastic yielding.

The definition of the equivalent yield stress (Y) is based on the Johnson-Cook model (Johnson *et al.* 1983), but with the addition of a damage softening term to reflect the deterioration of the yield stress as the void volume fraction increases, i.e.,

$$Y(\epsilon^p, \dot{\epsilon}^p, T, \xi) = \left[C_1 + C_2 (\epsilon^p)^n \right] \left[1 + C_3 \ln \left(\frac{\dot{\epsilon}^p}{\dot{\epsilon}_0} \right) \right] \left[1 - \left(\frac{T - T_0}{T_m - T_0} \right)^b \right] \left[1 - \left(\frac{\xi - \xi_0}{\xi_F - \xi_0} \right) \right] \quad (5.2)$$

which is identical to Equation (4.33).

The equivalent plastic shear strain is defined as,

$$\epsilon'P = \int \frac{\sqrt{3J_2} - Y}{3\mu} dt \quad (5.3)$$

where, μ is the shear modulus as defined in Section 4.2.

It should be noted that the definition of the equivalent plastic strain defined by Equation (5.3) has all the material behavior features (strain hardening, rate effects, thermal softening and material damage softening) that Equation (4.36) presents.

5.1.2 Modifications to the Void Growth Model

After implementation of the void growth model described by Equations (4.62)-(4.68), a series of tests were performed to determine what would be the time increment that would give a converging solution given the explicit integration scheme used. It was discovered that the time step required was two orders of magnitude smaller than the required to do the simulation without the growth model. This implied that a simulation of a hypervelocity impact event as described in Chapter six would require approximately 30 days. This was prohibitive given the time constraints. For this reason, the model presented in Equations (4.62)-(4.68) was simplified. The simplification consists of the elimination of the inertial effects, which reduces the nonlinear second order differential equation to a first order nonlinear differential equation,

$$\dot{\xi} = \frac{e^{\alpha\xi}(\bar{\sigma} - \bar{\sigma}_G)}{\eta(\bar{T})F(\xi)}, \quad \dot{\xi} > 0 \quad (5.4a)$$

$$\dot{\xi} = \frac{(\bar{\sigma} - \bar{\sigma}_G)}{\eta(\bar{T})F(\xi)}, \quad \dot{\xi} < 0 \quad (5.4b)$$

The implications of this simplification in a hypervelocity impact problem are hard to infer and will be material of further research. Nonetheless, the modifications and improvements made to the previous models presented by Johnson and Eftis are still part of the simplified model. The temperature local to the microvoid wall, the temperature dependence of the viscosity and the use of a viscoplastic constitutive equation that includes nonlinear strain hardening, strain-rate hardening and temperature softening, for the behavior of the solid material of the hollow sphere are included in the simplified void growth rate equation given by (5.4).

The question of the importance of maintaining the inertial term of the differential Equation (4.62) in simulations of very high strain-rate dynamic microvoid growth is an open question at this time, with adherents on both sides of the issue (Johnson 1981 and Tong *et al.* 1995).

5.1.3 Modifications to the Temperature Rate Equation

Even though the temperature rate Equation (4.87) was derived through the use of the energy rate balance equation that applies to any material under any loading condition, its implementation presented some difficulties. Under large volume expansion, Equation (4.84) has the tendency to give temperatures that are well below the room temperature and close to absolute zero. This was observed specifically in the ejecta rim produced in the simulation of hypervelocity impacts of spherical projectiles described below. It is suspected that Equation (4.87) may need a time step that is much smaller than the one used for it to converge to a solution. A study of this problem will be material for further

research. Thus, the temperature calculation was done using the model already implemented in AutodynTM (AutodynTM, Theory Manual), which is derived using classical thermodynamics,

$$\dot{T} = \frac{\dot{\psi}}{1-\psi} \gamma \frac{\rho_0}{\rho} T + \omega \frac{\text{tr}(\mathbf{T} \cdot \mathbf{D}^p)}{\rho C_v} \quad (5.5)$$

where γ is the Gruneisen coefficient as defined by Equation (3.20).

CHAPTER 6

NUMERICAL SIMULATIONS

In the literature review presented at the beginning of this dissertation, several papers were cited that employed similar constitutive models to the one presented in this work for the simulation of plate impact problems. Even though those models were simpler than the one described here, the use of those models for the simulation of impact problems were limited to very simple configurations. Most of the simulations were done for one-dimensional shock plate impact problems in the low to medium velocity range (Eftis *et al.* 1991, Cortes *et al.* 1995). Simulations of impact in the hypervelocity range have used a very simple limit strain or stress fracture model that does not model the evolution of material degradation in a realistic form (Quiñones *et al.* 1998). For this reason, the numerical simulation of hypervelocity impact of spherical projectiles with metallic target plates using the microdamage constitutive model shown here constitutes a step forward in the constitutive modeling and simulation of hypervelocity impact.

6.1 A Shock Pressure and Temperature Calculation

Prior to the implementation of the constitutive microdamage model into Autodyn™, a series of simulations of a representative point behind a shock wave were performed. A special program was developed using Delphi™ (Pascal compiler) to time integrate the governing equations, and plots of different variables were generated through a Matlab™ program. The objective of these simulations was to verify that all the

components of the constitutive model were showing the expected trends in terms of the behavior of the field variables. A comparison is shown in Figure 6.1 of the calculated and experimental shock-pressure volume strain curves for Copper. This figure shows a very good agreement between the calculated and experimental curves indicating the suitability of the equation of state presented in Chapter 3 for pressures up to 142 GPa. Figure 6.2 illustrates the calculated temperature rise with increasing pressure, where the solid curve is determined from the temperature rate Equation (4.87), while the open circle curve was calculated by others using the equations of classical thermodynamics (McQueen *et al.* 1960). In addition, Figure 6.2 includes a plot of the corresponding melt temperature (Equation 4.25, dashed line) for the corresponding pressure rise, which indicates that at approximately 155 GPa, the material reaches the melt point according to equation (4.87) (solid line).

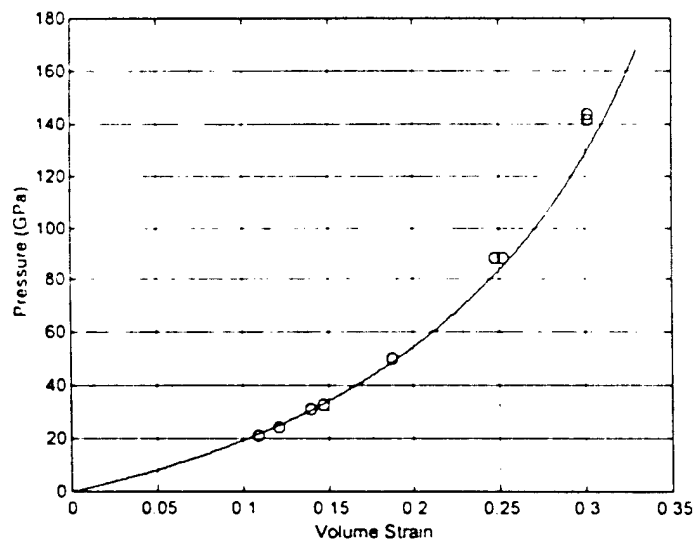


Figure 6.1 Calculated and experimental (open circles) pressure versus volume strain curves for Copper (circles, McQueen *et al.* 1960).

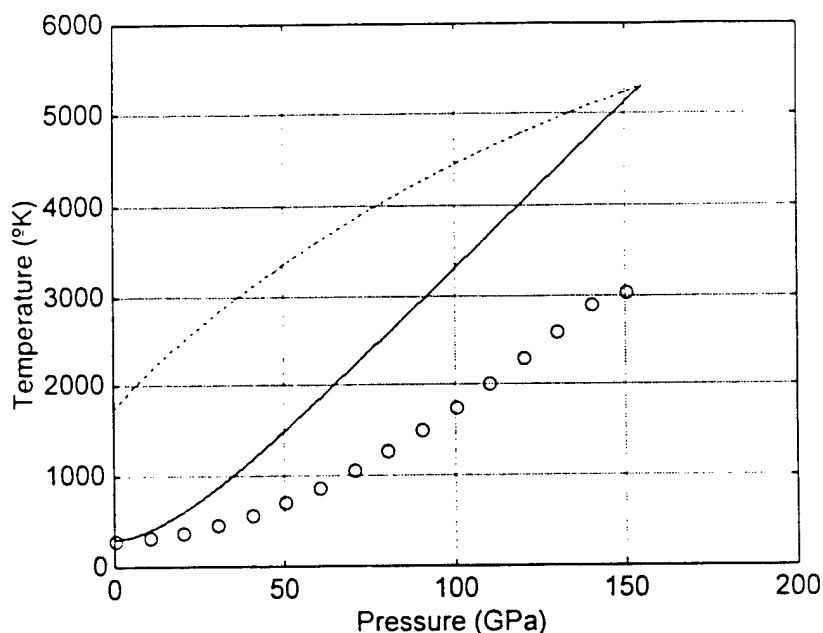


Figure 6.2 Calculations of temperature versus shock pressure for Copper using thermal energy rate balance (solid line) and classical thermodynamics (circles, McQueen *et al.* 1960), and melt temperature (dashed lines).

Because of the great difficulty in obtaining temperature measurements, directly or indirectly, of thermal changes that are of nano-second duration, there is no experimental data available that measures high shock-pressure induced temperature fluctuations. For this reason, a conclusion as to which temperature calculation gives a temperature closer to reality cannot be reached. This topic requires further research.

6.2 Hypervelocity Impact of Soda-Lime Glass Projectiles on Al_{1100} Target Plates

To test the capability of the constitutive model to simulate the deformation process, micro-damage evolution and finally fracture developed under hypervelocity impact, for different projectile diameter to plate thickness ratios a series of experimental

results on 1100 Aluminum plates were selected. Horz *et al.* (1995) presented results from a series of hypervelocity impact experiments of soda-lime glass spherical projectiles of 3.175 mm diameter that impact Al₁₁₀₀ plates of varied thickness at a nominal velocity of 6.0 km/s. In all, ten experiments were presented where the target plate thickness varied from 1.06 to 31.75 mm, while all the other parameters (projectile and target materials, projectile diameter and velocity) were kept fixed. Out of these ten experiments, three were selected to be simulated using the Autodyn™ code that was modified to include the constitutive model presented in this dissertation. Figure 6.3 shows postmortem pictures of the three cases selected from Horz *et al.* 1995. Also, Table 6.1 lists the dimensional characteristics of the three hypervelocity-impact cases. These three hypervelocity experiments were selected because they cover a wide range of plate thickness that result in three widely varied levels of damage.

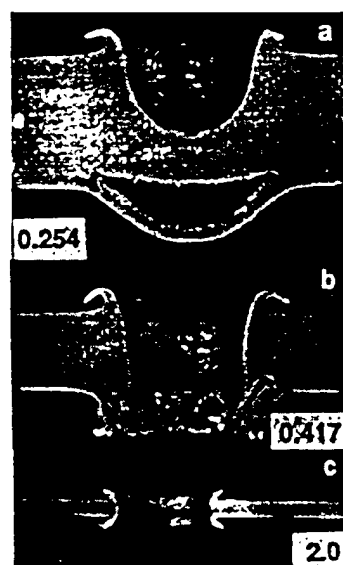


Figure 6.3 Cratering and penetration events in Al₁₁₀₀ targets of three different thickness (a=12.5 mm, b=7.61 mm and c=1.59 mm) using 3.175 mm diameter soda-lime glass projectiles at 6 km/s (Horz *et al.* 1995).

Table 6.1 Dimensional characteristics of hypervelocity impact cases.

Experimental Case	PROJECTILE		TARGET
	Diameter (mm)	Velocity (km/s)	Thickness (mm)
A	3.175	6	12.5
B	3.175	6	7.61
C	3.175	6	1.59

6.2.1 Computer Simulations Description

The simulations in Autodyn™ of the hypervelocity impact events previously described were setup using Lagrangian type grids for both the target and projectile. In all three cases the "Transmit" boundary condition was used to simulate a semi-infinite plate widthwise. The "Transmit" boundary condition allows a shock wave to move through the boundary of the grid without producing any reflection. In addition, advantage was taken of the fact that the impacts were normal to the target plate allowing axial symmetry to be used in the space discretization of the projectile and target. Figures 6.4 to 6.6 depict the grid configuration used for the three simulations corresponding to the experiments previously mentioned (see Figure 6.3 and Table 6.1). In all three simulations, the incremental-geometric-strain "eroding" algorithm was implemented for both the target and projectile with a 2.5 limit strain. This algorithm "erodes" (discards) the cells that reach the limit strain thus eliminating the cell-entangling problem that exists in Lagrangian grids.

Once void volume fraction reaches the critical value ξ_F (integration of Equation 4.70) at any cell within the grid, that cell is "eroded" away to simulate the local fracture

of the material. This has the disadvantage that the internal energy still stored in the eroded cell is eliminated. Autodyn™ does not provide any other way to simulate fracture in Lagrangian grids, and the implications of eroding a cell with high internal energy cannot be determined. The material parameters for Al₁₁₀₀ were obtained from numerous published works of other authors. Table 6.2 shows the material parameters for Al₁₁₀₀ together with a brief description of where they appear in the microdamage constitutive model.

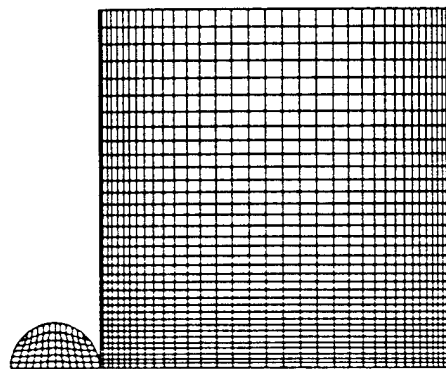


Figure 6.4 Grid configuration for simulation (a) corresponding to a target plate thickness of 12.5mm.

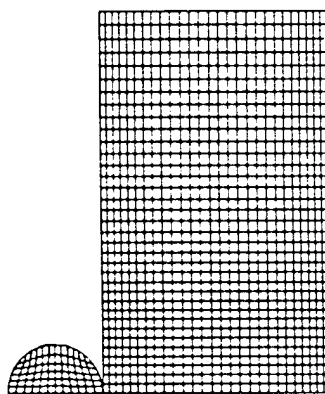


Figure 6.5 Grid configuration for simulation (b) corresponding to a target plate thickness of 7.61mm.

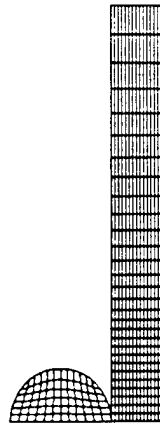


Figure 6.6 Grid configuration for simulation (c) corresponding to a target plate thickness of 1.59mm.

Table 6.2 Material parameters for Al₁₁₀₀.

Parameter	Value	Note
ρ_0	2.77 g/cm ³	Initial density
c_0	5.328 km/s	Bulk sound speed
S	1.338	Slope of the shock to particle speeds
γ_0	2.0	Gruneisen constant
C_v	875 J/Kg·°K	Specific heat
T_0	300 °K	Initial temperature
T_{m0}	923 °K	Initial melt temperature
k	1.38×10^{-23} J/°K	Boltzman constant
w	0.9	Fraction of plastic work dissipated as heat
K_0	78.6 GPa	Initial bulk modulus
μ_0	27.6 GPa	Initial shear modulus
A	-7.245	Constant in the definition of the Gruneisen coefficient
C_1	150 MPa	Yield stress in Johnson-Cook (JC) model
C_2	170 MPa	Strain hardening constant in the JC model
C_3	0.015	Strain rate hardening constant in the JC model
n	0.34	Strain hardening exponent in the JC model
β	1.03	Thermal softening constant
a_1	1.5	Constant in the definition of the melt temperature
a_2	0.004	Elastic coefficient temperature constant
η_0	10^3 Pa·s	Initial material viscosity
η_m	2×10^{-3} Pa·s	Melt temperature viscosity
m_1	2	Exponent in the plastic rate of deformation
ξ_0	10^{-3}	Initial void volume fraction
ξ_f	0.3	Critical void volume fraction
ξ_{nm}	5×10^{-3}	Maximum void volume fraction from nucleation
a_0	10^{-4} cm	Average initial radius of microvoids
h	7.54×10^{-2} s ⁻¹	Constant in the void nucleation model
σ_{n0}	-300 Mpa	Mean stress threshold for nucleation
φ	20	Constant in the void growth model
m_2	10.3×10^{-23}	Constant in the void nucleation model

For the case of the Soda-Lime glass projectile, the microdamage constitutive model presented above cannot be applied since the model is applicable only for ductile polycrystalline materials. For this reason, the Johnson-Holmquist brittle material model already implemented in Autodyn was used with the material parameters available in the materials library for glass, and in the paper by Taylor *et al.* (1999).

6.2.2 Simulation Results

The graphics capability of Autodyn™ allows the generation of contour plots of any field variable that forms part of the constitutive microdamage model. For the purpose of presenting the results of the simulations only pressure, temperature and void volume fraction contour plots will be shown.

Figures 6.8 to 6.10 give contour plots of the pressure, temperature and void volume fraction for the 12.5mm thick target plate (Case A, see Table 6.1) at 0 μ s, 0.5 μ s, 1.0 μ s, 1.5 μ s, 2 μ s, 2.5 μ s, 5 μ s and 20 μ s after impact. Figures 6.8(a), 6.9(a) and 6.10(a) illustrate the initial conditions just before impact. At 0.5 μ s after impact (see Figures 6.8(b), 6.9(b) and 6.10(b)), the maximum pressure at the bottom of the target is 26GPa and the corresponding temperature is 680°K. It should be noted that as the shock-compression wave moves through the target, the void volume fraction is being reduced to zero, which is indicated by the dark blue color in Figure (6.10b). At the moment of impact, the pressure in the target reached a maximum of 58GPa and the corresponding temperature is 900°K, but after 0.5 μ s they have decayed to the values shown in the figures. In these figures, the formation of a target rim is already evident. Figures 6.8(c-

e), 6.9(c-e) and 6.10(c-e), the shock wave continues to move across the target with the corresponding decay of the pressure and temperature and the reduction of the initial void volume fraction. In the pressure plots (see Figure 6.8), it should be noted that a tensile wave, reflected from the rear of the projectile trails the shock-compression wave. Once the shock compression wave reaches the back of the target plate it is reflected as a tensile wave that is superimposed on the trailing tensile wave. This superposition of tensile waves enhances the nucleation and growth of microvoids, which eventually leads to fracture. This effect is shown in Figures 6.8(e-f) and 6.10(f), where the void volume fraction has reached the critical value and spallation (fracture) has begun. Figures 6.8(h), 6.9(h) and 6.10(h) illustrate the state of the target plate at the end of the simulation (20 μ s after impact). At this time in the simulation, the geometrical changes of the target plate are negligible and the change in void volume fraction is zero. The predicted final crater penetration is 7.2mm compared to 7.3mm in the experiment. The predicted crater diameter is 12mm while the experimental is 12.5mm. This gives a depth of penetration to crater diameter (P/D_p) of 0.6 for the simulation and 0.58 for the laboratory experiment. The predicted diameter of the spallation area is 12.5mm and is 19mm for the corresponding laboratory experiment, indicating a thirty three percent error in the prediction of the spallation diameter.

Figures 6.11 to 6.13 give contour plots of the pressure, temperature and void volume fraction for the 7.61mm thick target plate (Case B, see Table 6.1) at 0 μ s, 0.5 μ s, 1.0 μ s, 1.5 μ s, 2 μ s, 2.5 μ s, 5 μ s and 20 μ s after impact. Figures 6.11(a), 6.12(a) and 6.13(a) illustrate the initial conditions just before impact. The evolution of the simulations for

Cases A and B (see Table 6.1) are identical up to approximately $1.0\mu\text{s}$ after impact, corresponding to contour plot (c) of Figures 6.8 to 6.10 and 6.11 to 6.13. Figure 6.11(d) shows the initiation of spallation after the reflection of the compression shock wave and its superposition with the trailing tensile wave. At $2\mu\text{s}$ after impact (Contour plot (e) of Figures 6.11 to 6.13), the projectile has "eroded" enough of the target plate so that the crater reaches the spallation area. In contour plots (f) to (g), the spallation diameter reaches its maximum value and the target back wall continues to bulge, driven by its momentum, while the penetration hole gets wider. Figures 6.11(h), 6.12(h) and 6.13(h) illustrate the state of the target plate at the end of the simulation ($20\mu\text{s}$ after impact). The predicted diameter of the penetration hole is 11mm while for the laboratory experiment is 11.4mm. The most significant difference between the simulation and the laboratory experiment is that in the simulation the spall does not detach at the same point as the laboratory experiment. The fact that in the simulation the spall section that is left attached to the target plate has reached an equivalent plastic strain of 1.2 (120%), indicates the possibility that another fracture mechanism, one that is not taken into account in the simulation and is operating in the laboratory experiment.

Figures 6.14 to 6.16 give contour plots of the pressure, temperature and void volume fraction for the 1.59mm thick target plate (Case C, see Table 6.1) at $0\mu\text{s}$, $0.5\mu\text{s}$, $1.0\mu\text{s}$, $1.5\mu\text{s}$, $2\mu\text{s}$, $2.5\mu\text{s}$, $5\mu\text{s}$ and $20\mu\text{s}$ after impact. Figures 6.14(a), 6.15(a) and 6.16(a) illustrate the initial conditions just before impact. In this last case, the projectile penetrates the target plate at approximately $1.0\mu\text{s}$ as shown in contour plot (c) of Figures 6.14 to 6.16. After initial penetration, the penetration-hole continues to grow and the

rims at the front and back of the target plate continue to develop as shown in contour plots (d) to (g). Figures 6.14(h), 6.15(h) and 6.16(h) illustrate the state of the target plate at the end of the simulation (20 μ s after impact). The predicted diameter of the penetration hole is 8.5mm while for the actual laboratory experiment it is 8.8mm. It is interesting to note the microdamage developed close to the wall of the penetration hole which is apparent in contour plots (c) and (d). It is the opinion of the author that this does not happen in the actual laboratory experiment, but it is not possible to determine if this is true since there are no radiographs at different times of the target plate through the penetration process. The reason for the appearance of microdamage in the numerical simulation may possibly be that there is another fracture process acting that is not being modeled in the simulation. For example, if the target plate fails because of shear banding, the tensile mean stresses needed to create the fracture shown in contour plots (c) and (d) may not be reached. This phenomenon is demonstrated by Figure 6.7, which shows a polished and etched cross section through a rod and a target plate for a case of partial penetration. In this picture, two fracture mechanisms are evident in the target plate. In the upper portion of the penetration hole, as indicated by the arrows, shear banding that runs through the remaining section of the plate has occurred, while in the lower section of the hole, shear banding is not evident and a tensile crack has developed instead. Thus, the fact that formation of shear bands that run through the target plate (plugging) impedes the formation of cracks or microdamage in the plate, indicates that the implementation of a shear band fracture mechanism is needed to accurately simulate

the penetration process and eliminate the unrealistic development of microdamage close to the wall of the penetration hole.

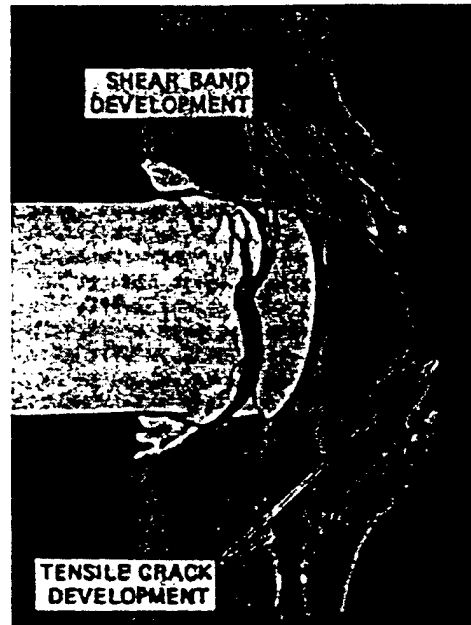


Figure 6.7 Microfailure features observed on a section taken through a steel plate and embedded steel rod after impact (Shockey *et al.* 1979).

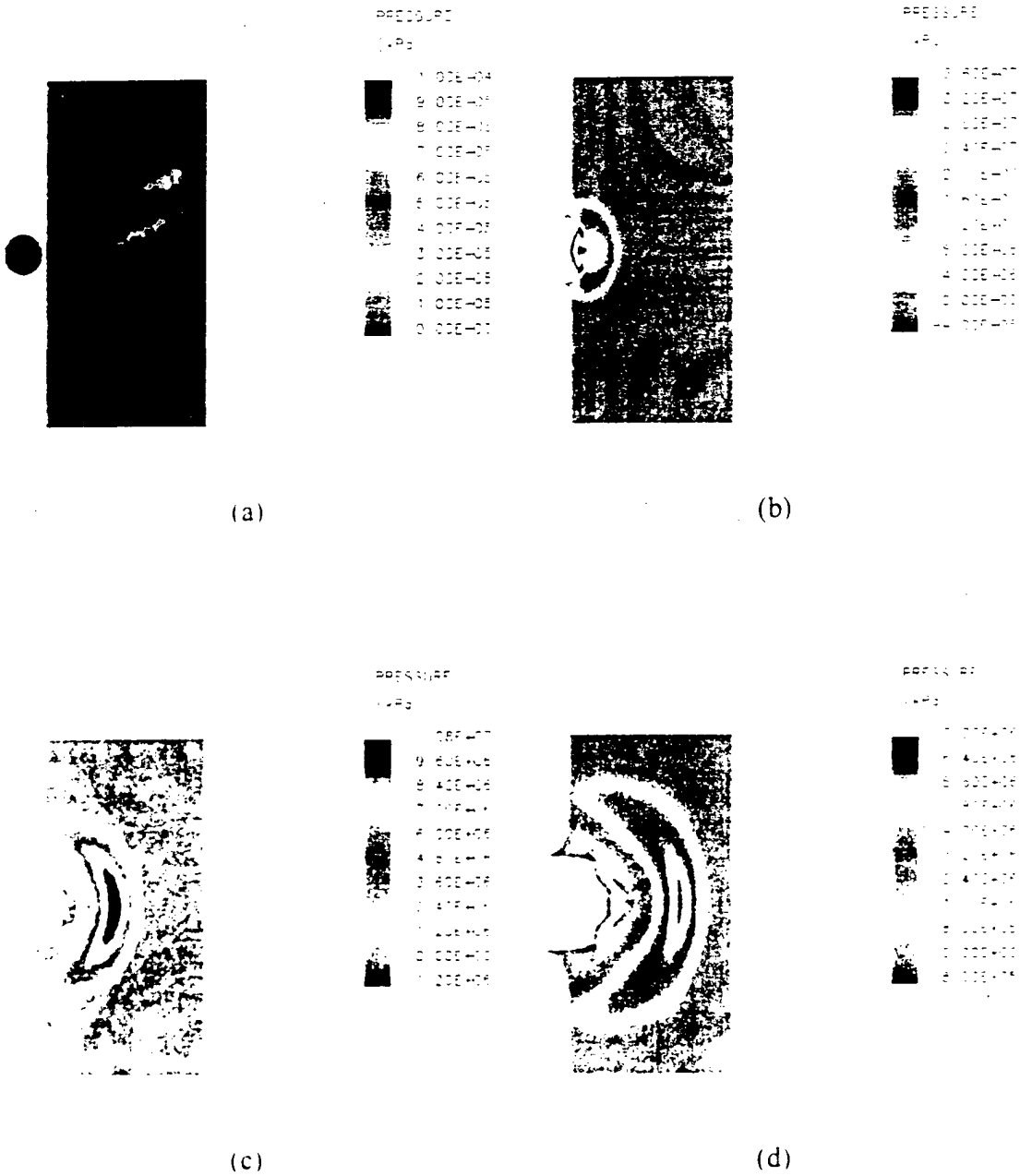


Figure 6.8(1) Pressure contour plots for 12.5mm thick Al₁₁₀₀ target plate at 0μs, 0.5μs, 1.0μs, 1.5μs (a, b, c, d respectively) after impact.

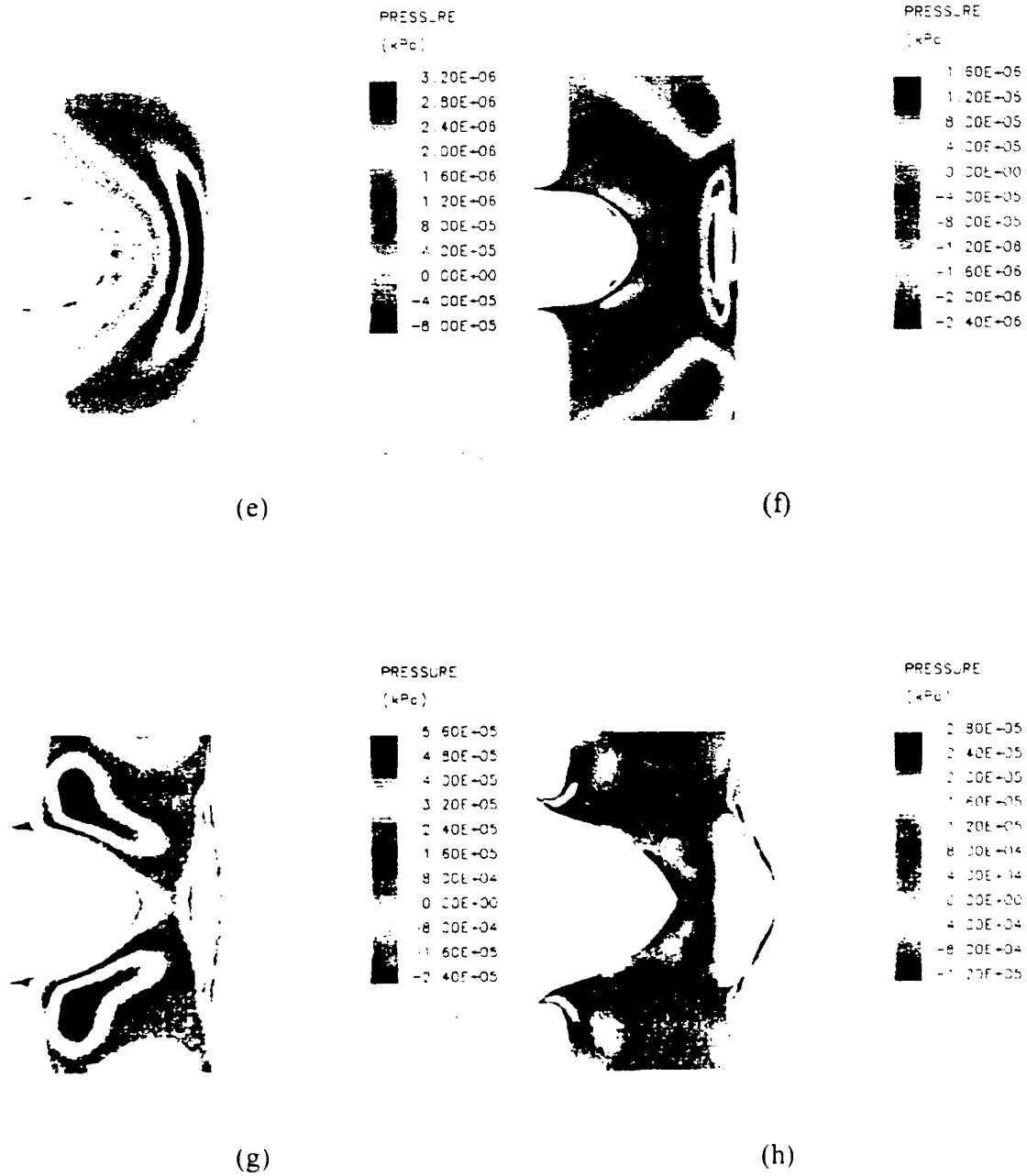


Figure 6.8(2) Pressure contour plots for 12.5mm thick Al₁₁₀₀ target plate at 2μs, 2.5μs, 5μs and 20μs (e, f, g, h respectively) after impact.

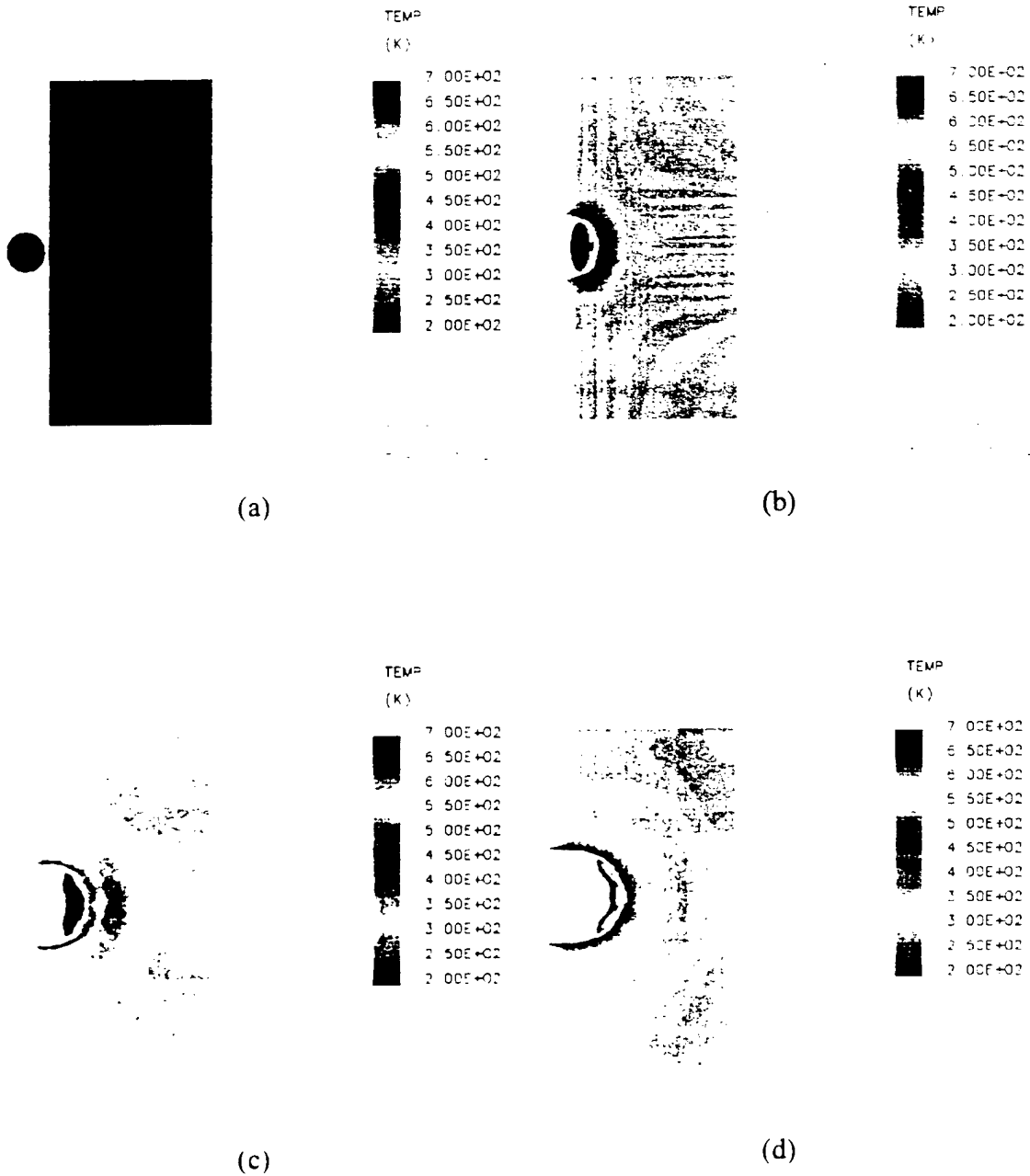


Figure 6.9(1) Temperature contour plots for 12.5mm thick Al_{100} target plate at $0\mu s$, $0.5\mu s$, $1.0\mu s$, $1.5\mu s$ (a, b, c, d respectively) after impact.

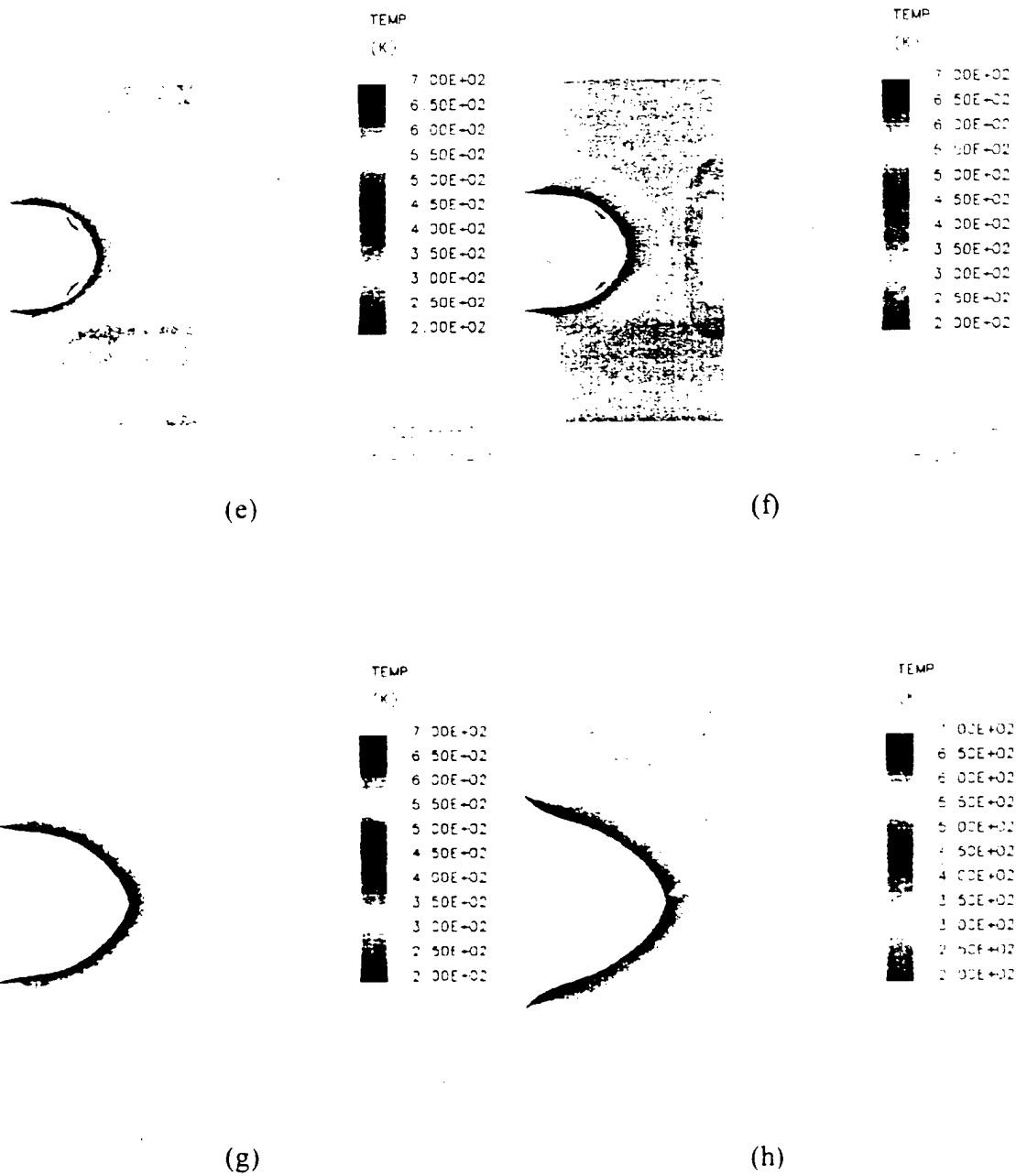


Figure 6.9(2) Temperature contour plots for 12.5mm thick Al_{1100} target plate at 2 μs , 2.5 μs , 5 μs and 20 μs (e, f, g, h respectively) after impact.

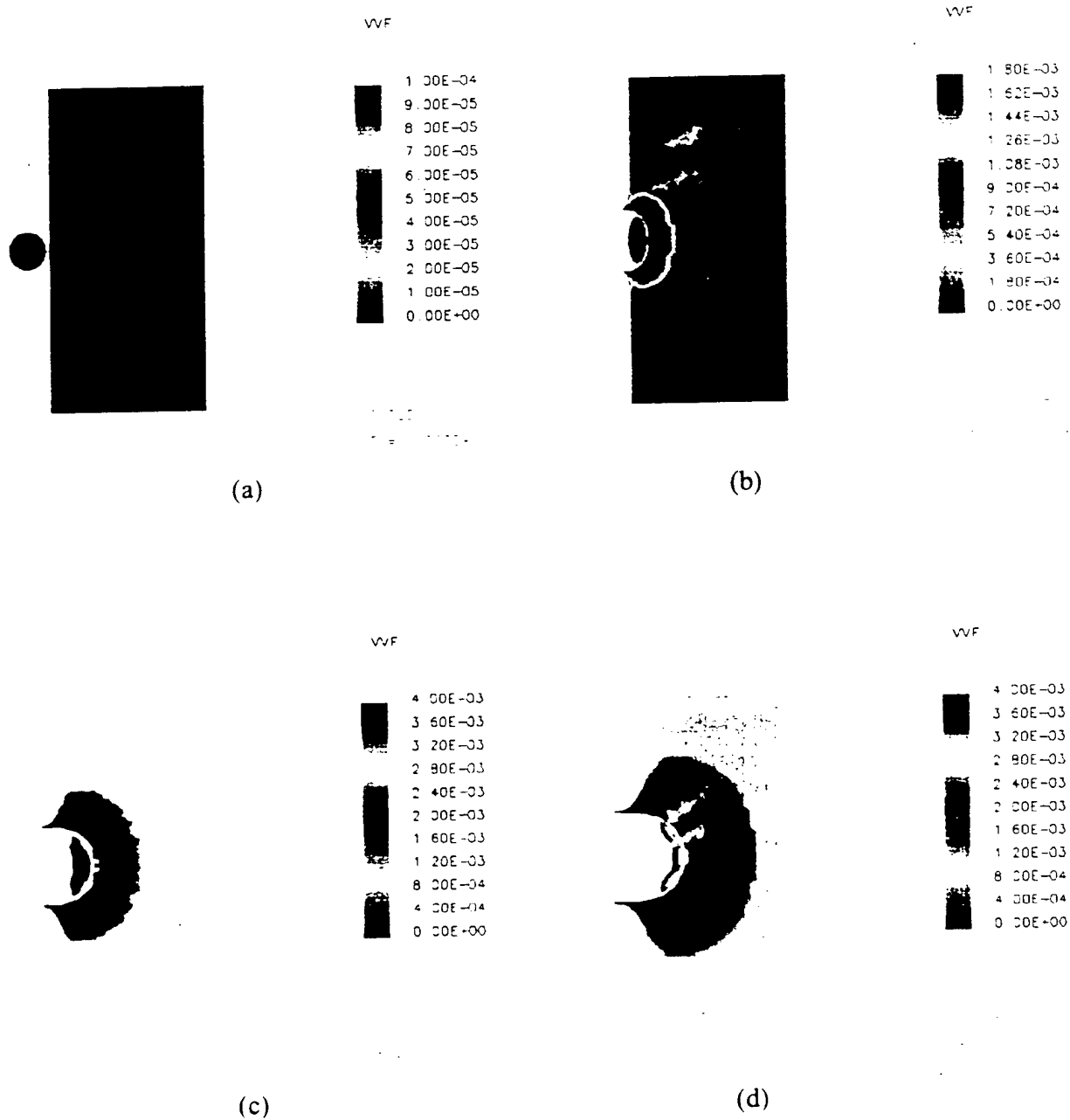


Figure 6.10(1) Void-volume fraction contour plots for 12.5mm thick Al_{100} target plate at $0\mu s$, $0.5\mu s$, $1.0\mu s$, $1.5\mu s$ (a, b, c, d respectively) after impact.

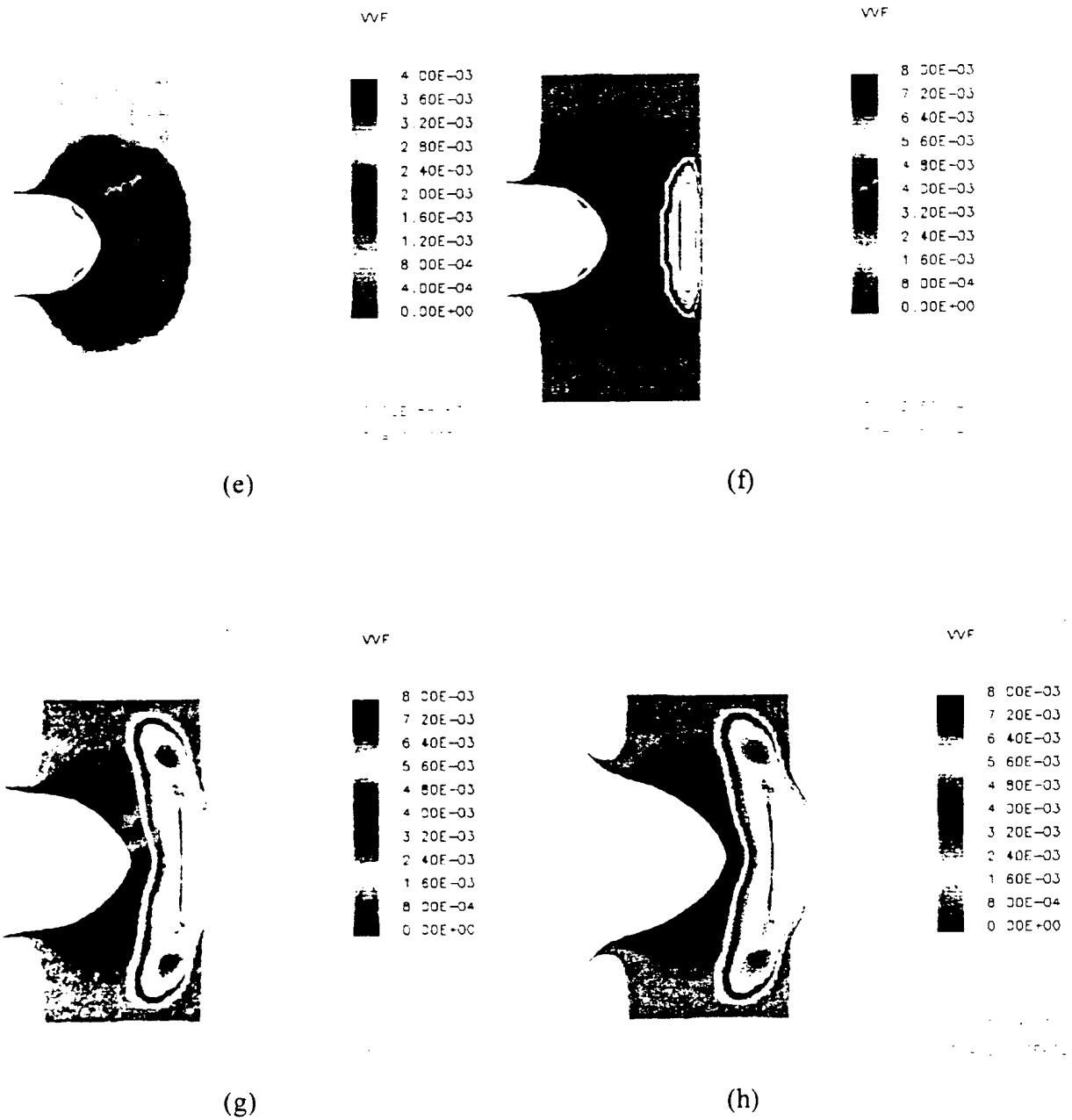


Figure 6.10(2) Void-volume fraction contour plots for 12.5mm thick Al₁₁₀₀ target plate at 2μs, 2.5μs, 5μs and 20μs (e, f, g, h respectively) after impact.

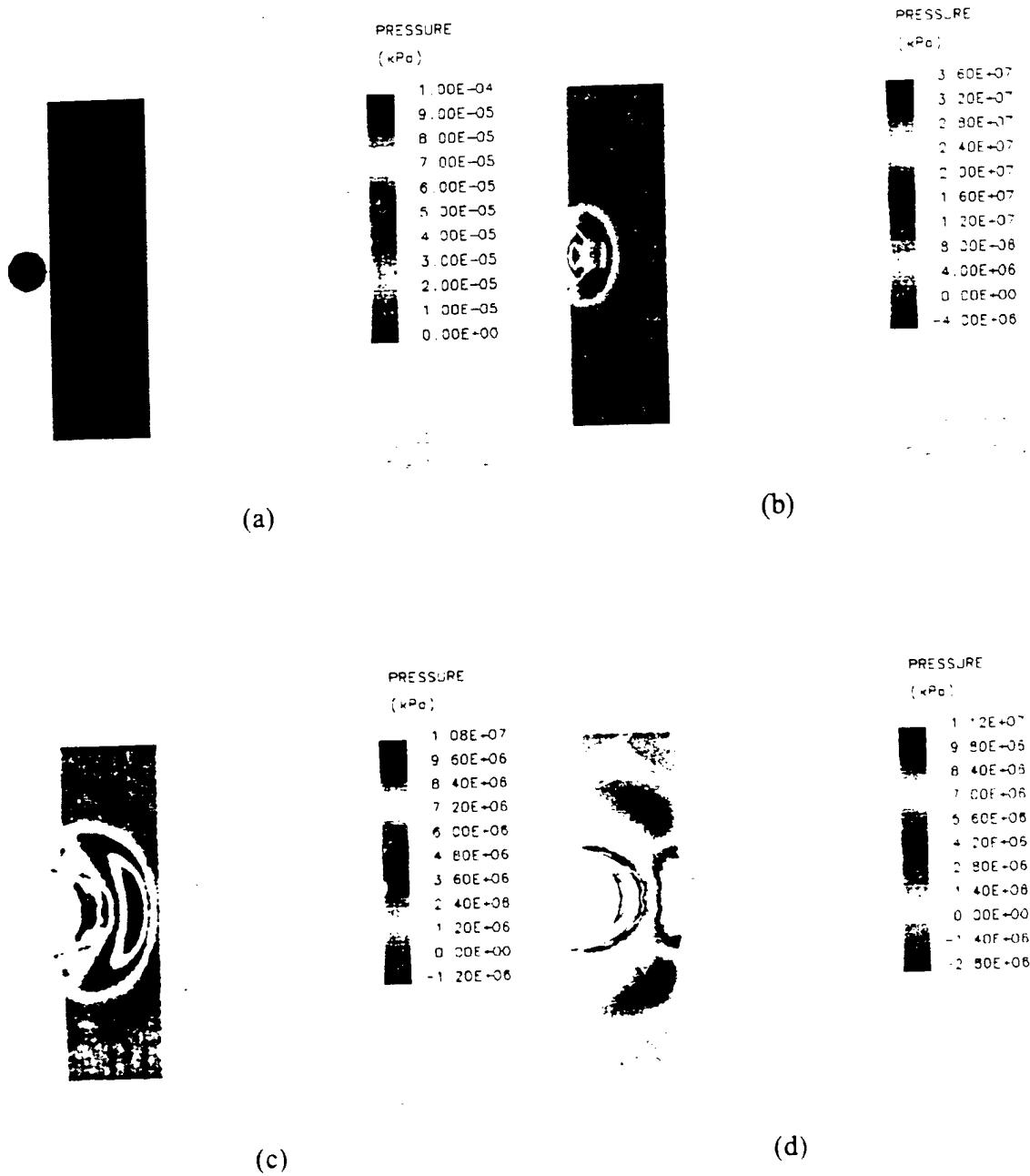
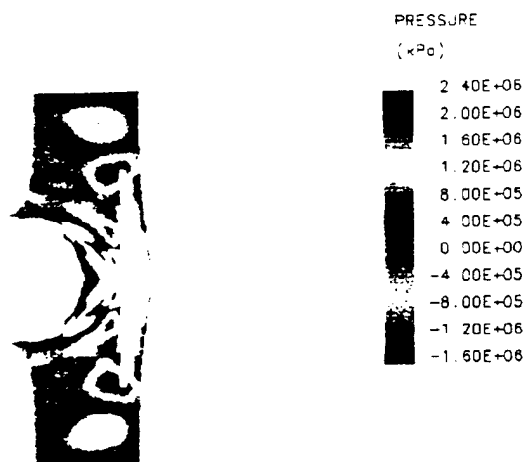
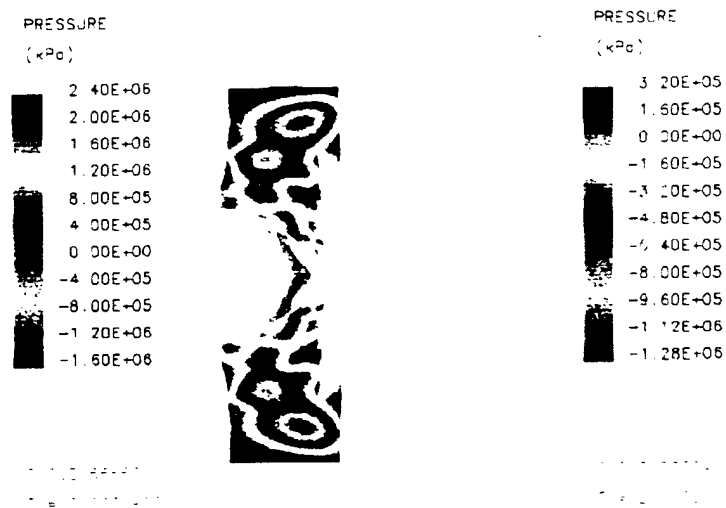


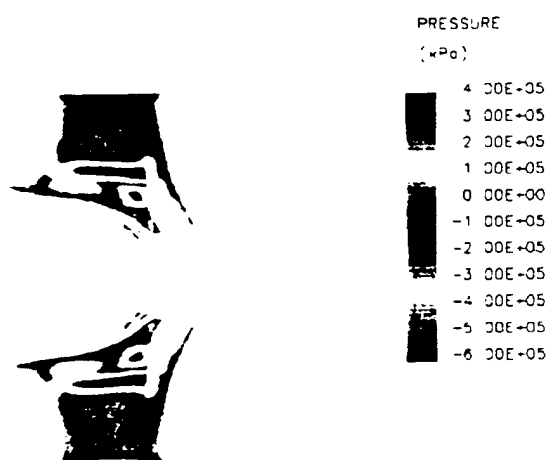
Figure 6.11(1) Pressure contour plots for 7.61mm thick Al₁₁₀₀ target plate at 0μs, 0.5μs, 1.0μs, 1.5μs (a, b, c, d respectively) after impact.



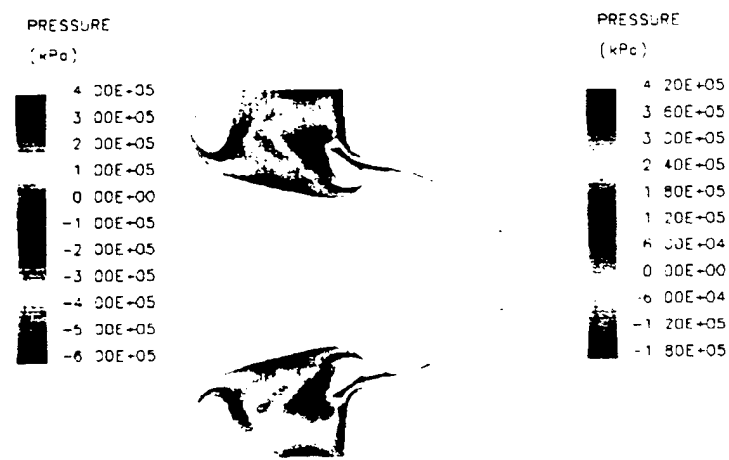
(e)



(f)

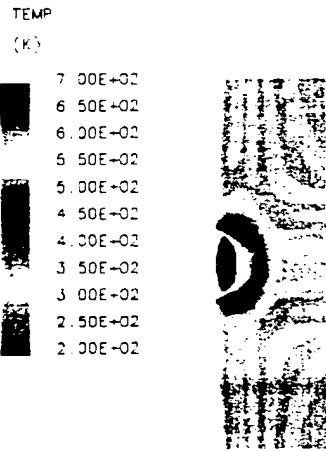


(g)

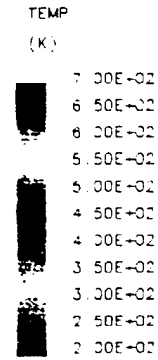


(h)

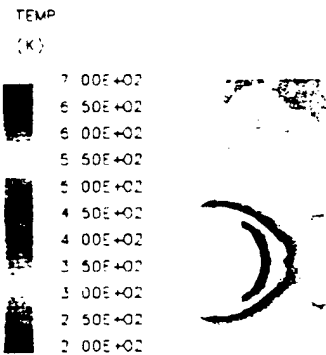
Figure 6.11(2) Pressure contour plots for 7.61mm thick Al_{1100} target plate at $2\mu s$, $2.5\mu s$, $5\mu s$ and $20\mu s$ (e, f, g, h respectively) after impact.



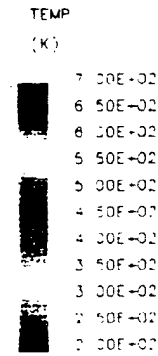
(a)



(b)

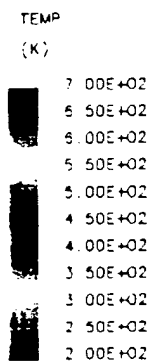
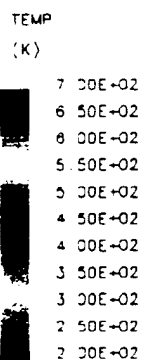


(c)



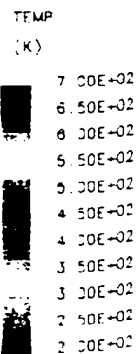
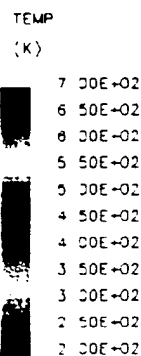
(d)

Figure 6.12(1) Temperature contour plots for 7.61mm thick Al₁₁₀₀ target plate at 0μs, 0.5μs, 1.0μs, 1.5μs (a, b, c, d respectively) after impact.



(e)

(f)



(g)

(h)

Figure 6.12(2) Temperature contour plots for 7.61mm thick Al_{1100} target plate at $2\mu s$, $2.5\mu s$, $5\mu s$ and $20\mu s$ (e, f, g, h respectively) after impact.

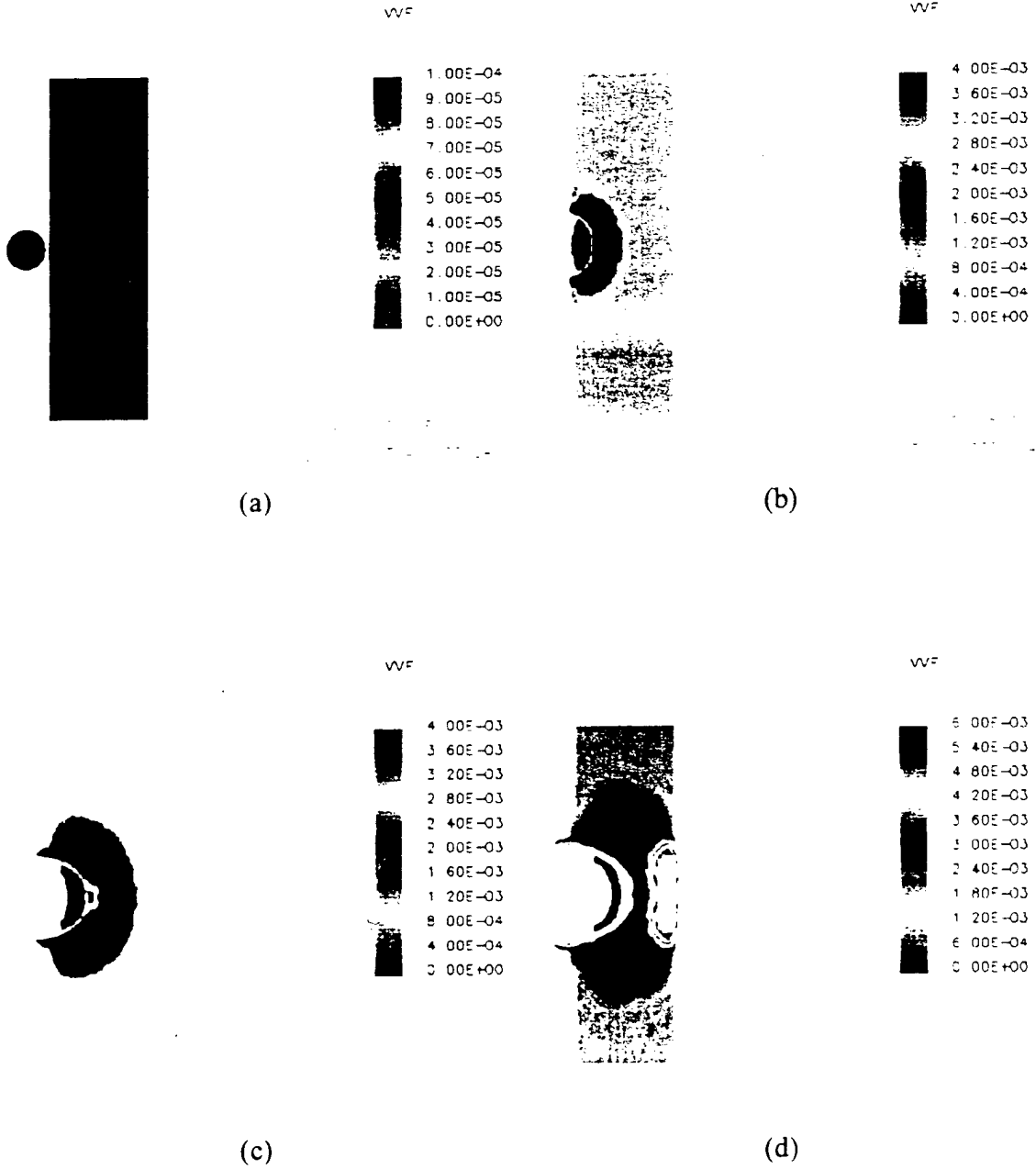


Figure 6.13(1) Void-volume fraction contour plots for 7.61mm thick Al_{1100} target plate at $0\mu s$, $0.5\mu s$, $1.0\mu s$, $1.5\mu s$ (a, b, c, d respectively) after impact.

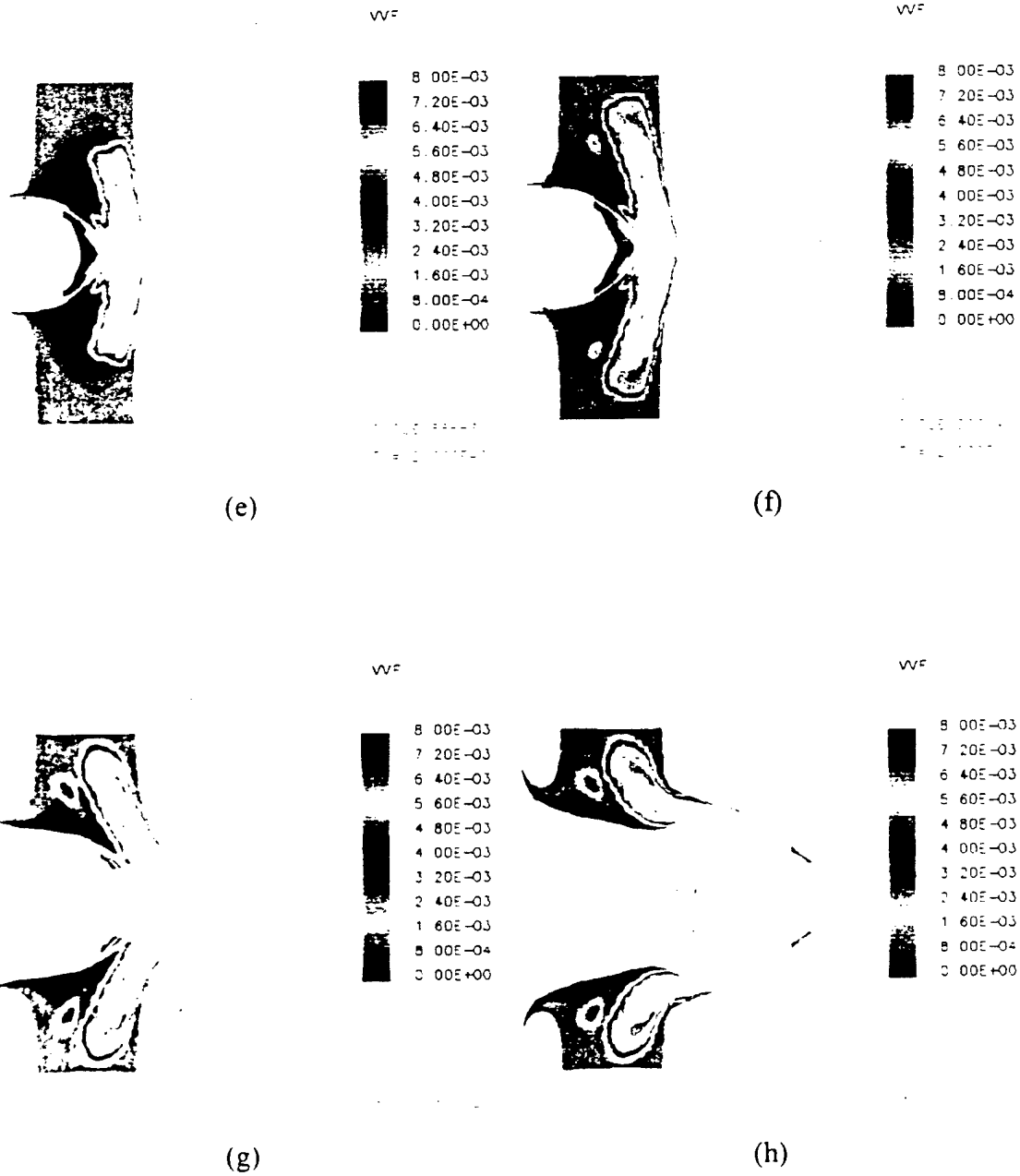
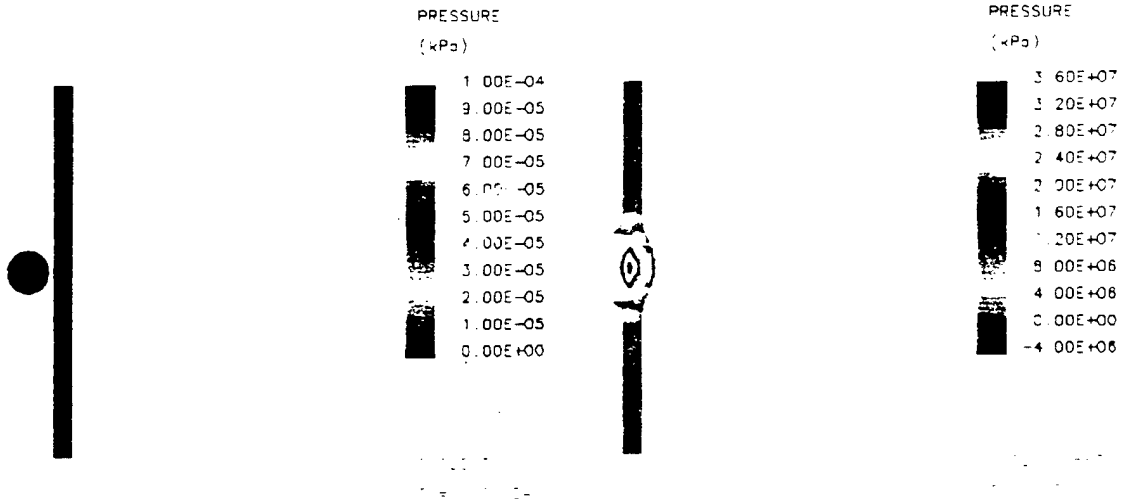
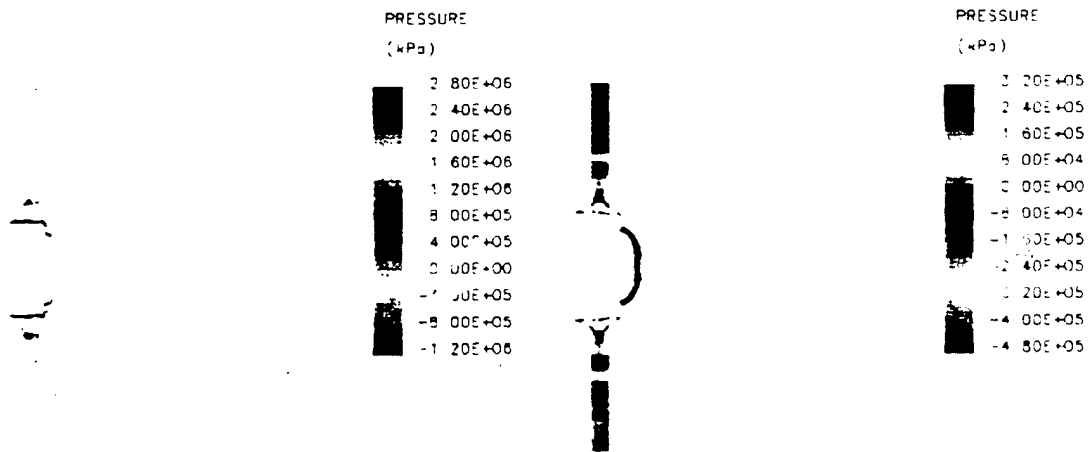


Figure 6.13(2) Void-volume fraction contour plots for 7.61 mm thick Al₁₁₀₀ target plate at 2 μs, 2.5 μs, 5 μs and 20 μs (e, f, g, h respectively) after impact.



(a)

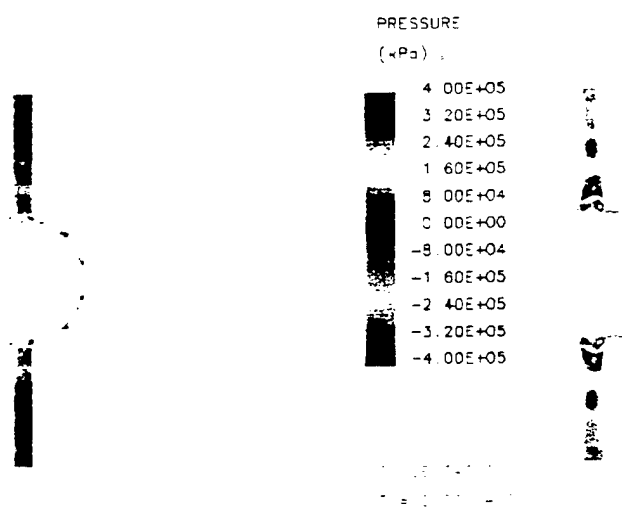
(b)



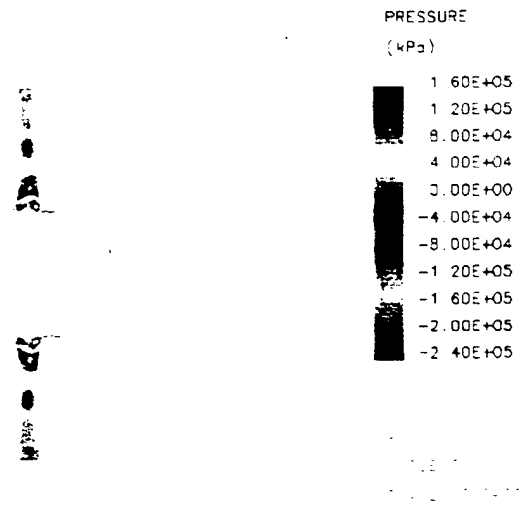
(c)

(d)

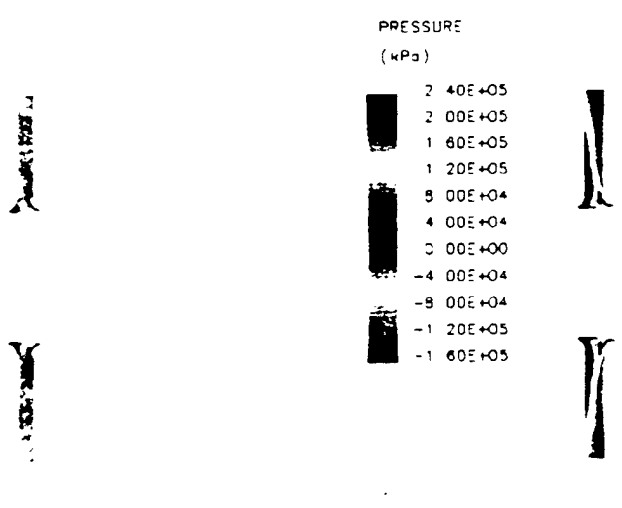
Figure 6.14(1) Pressure contour plots for 1.59mm thick Al₁₁₀₀ target plate at 0µs, 0.5µs, 1.0µs, 1.5µs (a, b, c, d respectively) after impact.



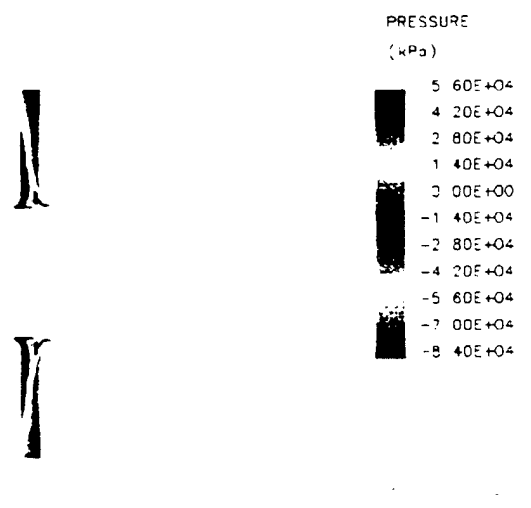
(e)



(f)



(g)



(h)

Figure 6.14(2) Pressure contour plots for 1.59mm thick Al₁₁₀₀ target plate at 2 μ s, 2.5 μ s, 5 μ s and 20 μ s (e, f, g, h respectively) after impact.

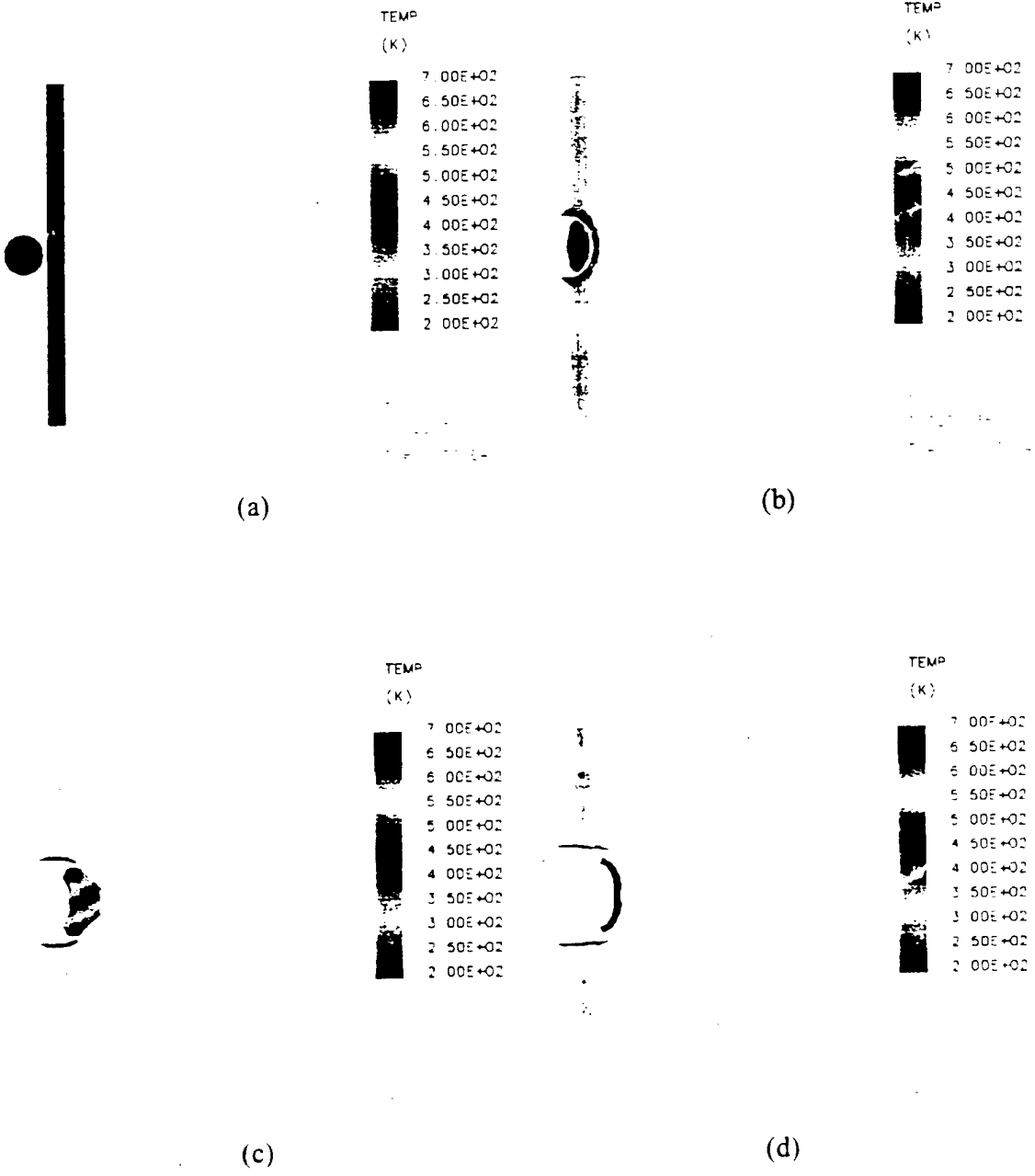


Figure 6.15(1) Temperature contour plots for 1.59mm thick Al₁₁₀₀ target plate at 0μs, 0.5μs, 1.0μs, 1.5μs (a, b, c, d respectively) after impact.

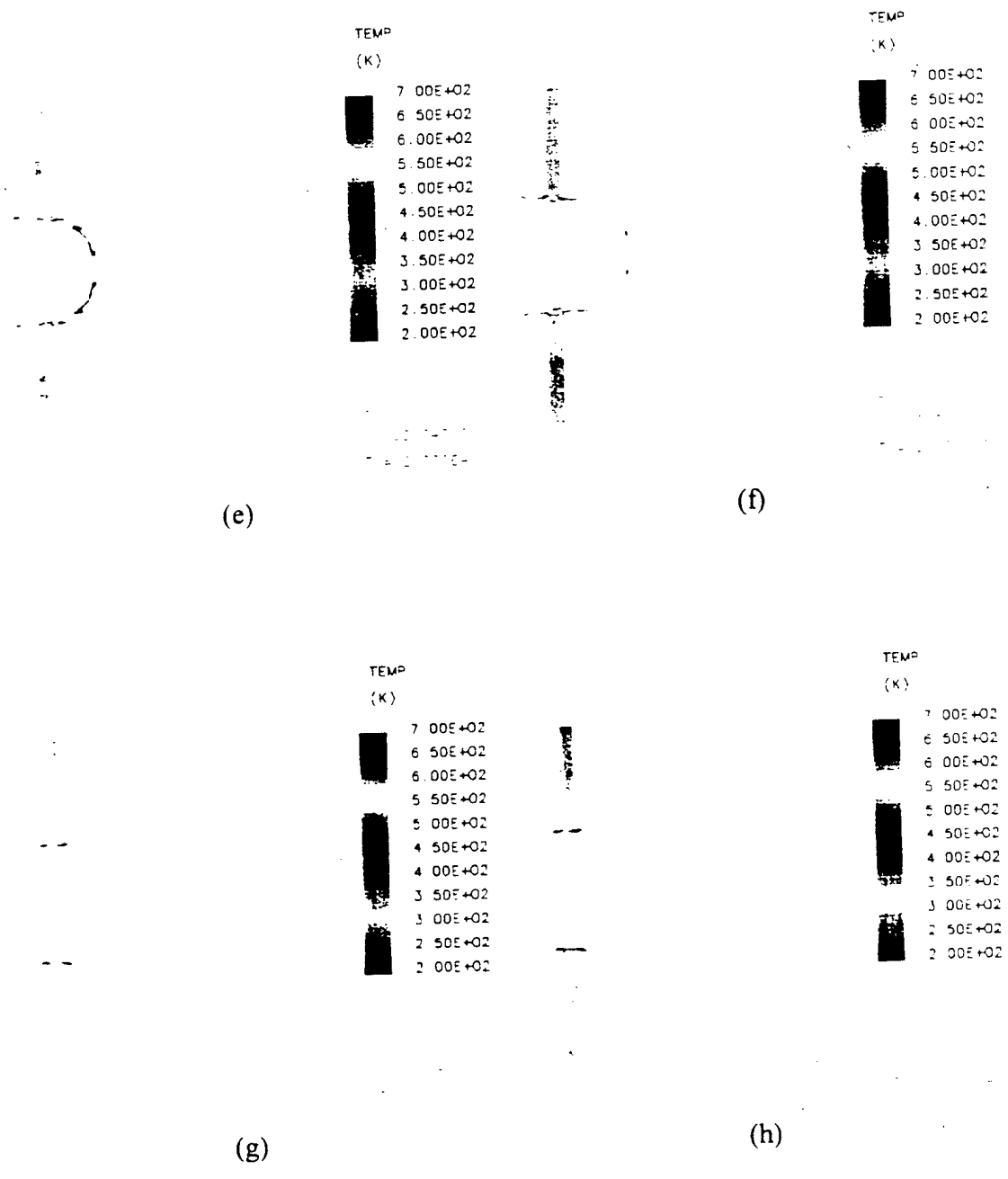


Figure 6.15(2) Temperature contour plots for 1.59mm thick Al₁₁₀₀ target plate at 2μs, 2.5μs, 5μs and 20μs (e, f, g, h respectively) after impact.

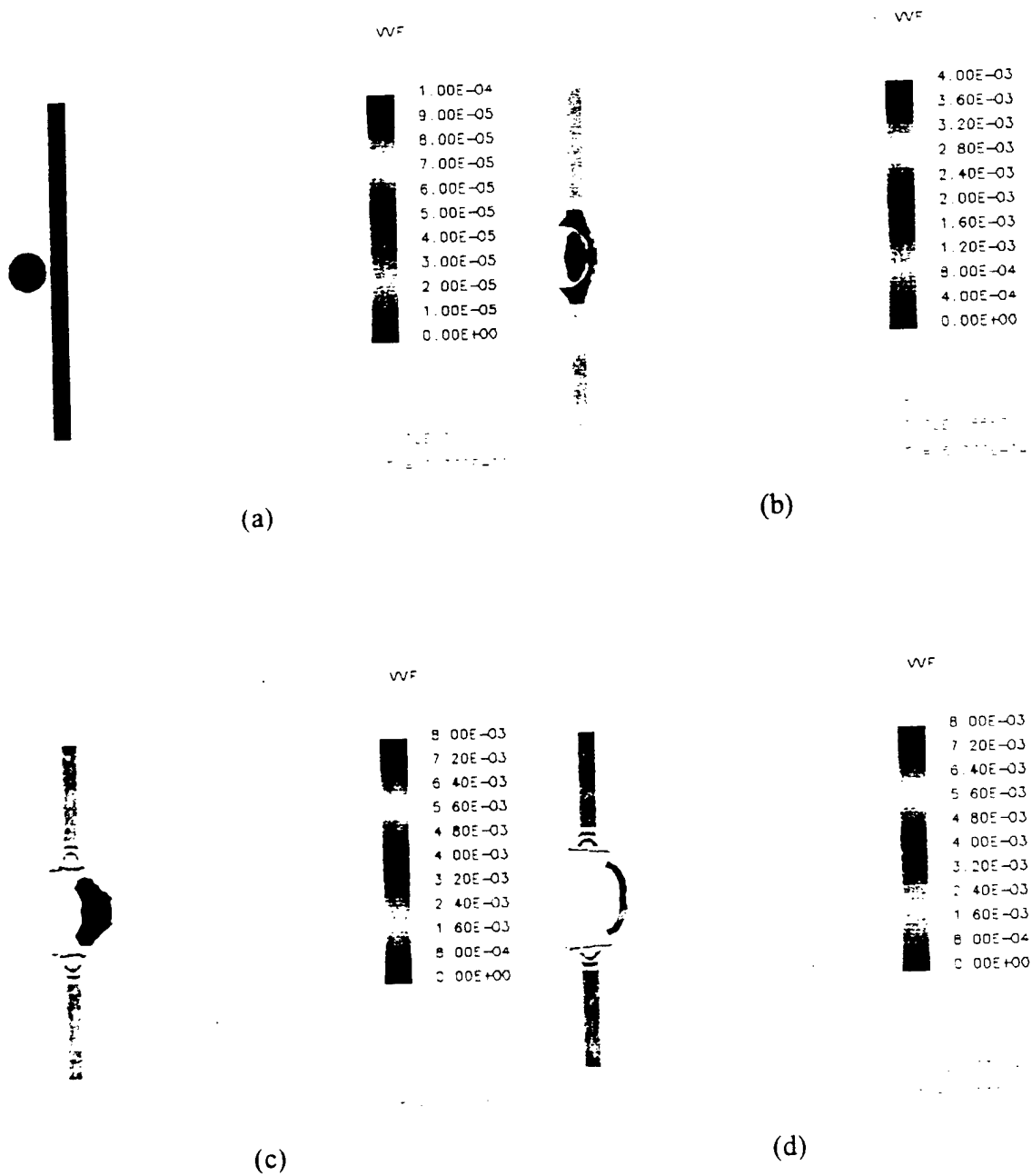
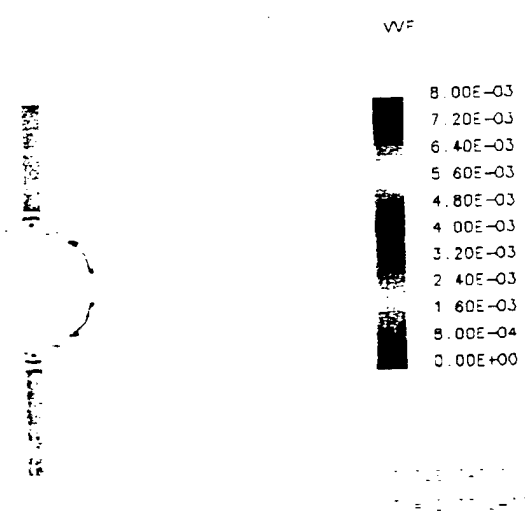
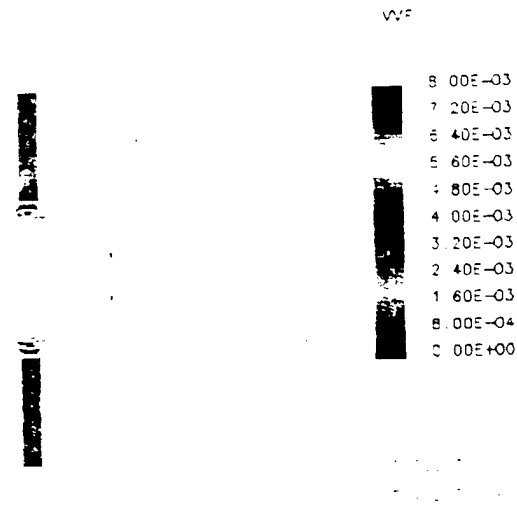


Figure 6.16(1) Void-volume fraction contour plots for 1.59mm thick Al_{1100} target plate at $0\mu s$, $0.5\mu s$, $1.0\mu s$, $1.5\mu s$ (a, b, c, d respectively) after impact.



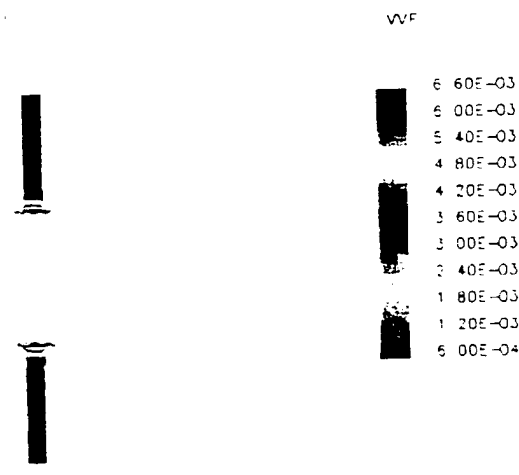
(e)



(f)



(g)



(h)

Figure 6.16(2) Void-volume fraction contour plots for 1.59mm thick Al_{1100} target plate at $2\mu s$, $2.5\mu s$, $5\mu s$ and $20\mu s$ (e, f, g, h respectively) after impact.

CHAPTER 7

CONCLUSIONS AND RECOMMENDATIONS

7.1 Introduction

The literature review presented in Chapter 1 demonstrated the necessity to improve upon the constitutive models used for the simulation of high shock loading problems, especially in relation to hypervelocity impact. As was stated earlier, the development of advanced constitutive models for the simulation of hypervelocity impacts is of primary importance to the Aerospace and Defense industry. For this reason, the goal of the research work presented in this dissertation was to develop a constitutive-microdamage model that can describe thermo-mechanical deformation associated with high shock compression, release, dilatation and shear, and the progressive microdamage that leads to fracture of ductile polycrystalline materials.

7.2 Summary

At the beginning of this dissertation, a review of appropriate literature was conducted and a brief description of the most relevant papers was presented in Chapter 1.

The first stage in the development of the constitutive model was the formulation of the Rankine-Hugoniot relations presented in Chapter 2, which were derived from the "jump conditions" across a shock wave and coupled with the U_S-U_P (shock speed to particle speed) empirical linear relation. The Rankine-Hugoniot relations were used to

give the final form of the Mie-Gruneisen Equation of State, which was developed with detail in Chapter 3.

The focal point of the work presented in this dissertation is the development of the microdamage constitutive model that describes the thermo-elastic and thermo-viscoplastic behavior of polycrystalline materials, as well as microdamage evolution in the form of microvoid nucleation growth and coalescence. The development of the microdamage constitutive models is presented in Chapter 4.

Due to the limitations imposed by the numerical framework upon which the Autodyn code is built, a series of simplifications had to be imposed on the implementation of the microdamage constitutive model. These simplifications affected the plastic rate of deformation equation, the microvoid growth rate equation and the temperature rate equation in the manner described in Chapter 5.

To test the performance of the microdamage constitutive model, a series of three hypervelocity impact laboratory experiments were selected for simulation. These three experiments covered a wide range of projectile diameter-target thickness ratios. In the three impact simulations Al₁₀₀ target plates were impacted with soda-lime glass spherical projectiles at 6.0 km/s. A detailed description of the laboratory experiments, simulation parameters and simulation results were given in Chapter 6.

7.3 Conclusions

The following conclusions can be reached from the research work discussed in the previous chapters:

- a) The microdamage constitutive model as implemented in the AutodynTM code successfully simulated the depth of penetration and crater diameter for the 12.5mm thick target plate (Case A) with an error below five percent.
- b) The diameter of the spall for the 12.5mm thick target plate (Case A) was under predicted by thirty three percent. It is the view of the author that this error could be reduced if some of the material parameters presented in Table 6.2 were modified. However, the decision was made to keep the material parameters within the ranges listed in the literature.
- c) The constitutive model successfully predicted the diameter of the penetration hole in the 7.61mm thick plate (Case B) to within a four percent error.
- d) There is a discrepancy in the extent of spall detachment for the 7.61mm thick plate (Case B) between the numerical simulation and the laboratory experiment, but in general, the main deformation and fracture features are reasonably simulated.
- e) The constitutive model successfully predicted the diameter of the penetration hole in the 1.59mm thick plate (Case C) to within a four percent error.
- f) The existence of microdamage developed close to the wall of the penetration hole in the 1.59mm thick plate (Case C) cannot be corroborated, since there are no radiographs available of the state of the target plate at approximately

1.0 μ s after impact for the actual laboratory experiment. Even though it is not possible to corroborate the existence of microvoid damage, the fact that the numerical simulation shows rough surfaces on the wall of the penetration hole, while the experiment does not, seems to indicate that the micro damage process might not be present in the actual laboratory experiment.

- g) The discrepancies between the numerical simulations and experimental results described in conclusions (d) and (f) seem to indicate that there is the possibility that another failure mechanism, such as shear band formation; that is not taken into account in the model simulation, is present in the laboratory experiment.

7.4 Recommendations

Because of the discrepancies mentioned previously, it is recommended that the microdamage evolution model be complemented by a shear or shear band failure model. This would improve the constitutive model presented here and would extend its successful applicability to a wider range of projectile diameter to target plate thickness ratios.

It is also recommended that the microdamage constitutive model be implemented for a Eulerian type grid. This would eliminate the necessity to implement an "eroding" algorithm to eliminate highly deformed cells, and to simulate fracture in the form described in Chapter 6. Furthermore, the possibility of doing simulations in a three-dimensional configuration should be considered. This should be done because in the

actual laboratory experiment, the axial symmetry is only present until the spall detaches and petal shape fracture begins to develop. This could be the reason for the discrepancies in the detached spall fracture mentioned in conclusion (d).

The microvoid nucleation model is considered by the author to be one of the least developed components of the microdamage constitutive model presented here. In the literature review conducted as part of the research program, there are no reports of studies of the nucleation process under mean stresses that are at least one order of magnitude greater than the nucleation threshold, and at strain rates of the order of 10^8 s^{-1} , as is the case in the hypervelocity impact experiments discussed in the simulations part of this dissertation. Even though the microvoid nucleation model was improved here by incorporating a strain and strain rate dependent nucleation threshold, it is the view of the author that further research has to be conducted on this subject.

As already mentioned, the energy rate equation (4.86) was derived through the use of the energy rate balance equation that applies to any material under any loading condition, but it presented difficulties in its numerical implementation as described in Section 5.1.3, and the model already implemented in Autodyn™ had to be used instead. Furthermore, it was demonstrated in Section 6.4 that there is a significant difference in the temperatures calculated with the energy rate balance equation (4.86) and the calculation with classical thermodynamics, upon which the Autodyn™ model is based in part. For this reason, further research has to be conducted to determine which calculation predicts the actual experimental temperature under hypervelocity impact more

accurately. This is a challenging problem because of the difficulties in measuring temperature fluctuations, in laboratory experiments, that last only a few nanoseconds.

Lastly, it is recommended that the model be tested for different projectile and target materials. This would give more confidence in the implementation of the microdamage constitutive model presented in this dissertation.

REFERENCES

- Addressio F. L., Johnson J. N. and Maudlin P. J., (1993), "The Effect Of Void Growth On Taylor Cylinder Impact Experiments," *Journal of Applied Physics*, Vol.73/11, pp. 7288-7297.
- Anderson C. E. Jr., (1987), "An Overview of the Theory of Hydrocodes," *International Journal of Impact Engineering*, Vol.5, pp. 33-59.
- Anderson C. E. Jr., Littlefield D. L. and Walker J. D., (1993a), "Long-Rod Penetration, Target Resistance, and Hypervelocity Impact," *International Journal of Impact Engineering*, Vol.14, pp. 1-12.
- Anderson C. E. Jr., Mullin S. A. and Kuhlman C. J., (1993b), "Computer Simulations of Strain-Rate Effects in Replica Scale Model Penetration Experiments," *International Journal of Impact Engineering*, Vol. 13/1, pp. 35-52.
- Anderson C. E. Jr., Hohler V., Walker J. D. and Stilp A. J., "Time-Resolved Penetration of Long Rods Into Steel Targets," *International Journal of Impact Engineering*.
- Argyris J. H., Vaz L. E. and Willam K. J., (1981), "Integrated Finite Element Analysis of Coupled Thermoviscoplasticity Problems," *Journal of Thermal Stress*, Vol.4, pp. 121-153.
- Asay J. R. and Kerley G. I., (1987), "The Response of Materials to Dynamic Loading," *International Journal of Impact Engineering*, Vol.5, pp. 69-99.
- Autodyn, "Theory Manual," Interactive Non-Linear Dynamic Analysis Software.
- Becker R., Needleman A., Richmond O. and Tvergaard V., (1988), "Void Growth and Failure in Notched Bars," *Journal of Mechanical Physics in Solids*, Vol.36/3, pp. 317-351.
- Benson D. J., (1989), "An efficient, Accurate, Simple ALE Method for Nonlinear Finite Element Programs," *Computer Methods in Applied Mechanics and Engineering*, 72, pp.305-350, North-Holland.
- Benson D. J., (1993), "An Analysis of Void Distribution Effects on the Dynamic Growth and Coalescence of Voids in Ductile Metals," *Journal of Mechanical Physics of Solids*, Vol.41/8, pp. 1285-1308.

- Boslough M. B. and Asay J. R., (1993), "Basic Principles of Shock Compression," *High-Pressure Shock Compression of Solids (Chapter 2)*, James R. Asay and Mohsen Shahinpoor (Editors), Springer-Verlag.
- Butcher B. M., Carroll M. M. and Holt A. C., (1974), "Shock-wave compaction of porous aluminum," *Journal of Applied Physics*, Vol.45/9, pp. 3864-3875.
- Carroll M. M. and Holt A. C., (1972), "Static and Dynamic Pore-Collapse Relations for Ductile Porous Materials", *Journal of Applied Physics*, Vol.43/4, pp. 1626-1635.
- Carroll M. M., Kim K. T. and Nesterenko V. F., (1986), "The Effect Of Temperature On Viscoplastic Pore Collapse," *Journal of Applied Physics*, Vol.59/6, pp. 1962-1967.
- Carroll M. M., (1985), "Radial Expansion of Hollow Spheres of Elastic-Plastic Hardening Material," *International Journal of Solids Structures*, Vol.21/7, pp. 645-670.
- Carroll M. M., (1986), "Micromodeling of Void Growth and Collapse," *Homogenization and Effective Moduli of Materials and Media*, Ericksen J., Kinderlehrer D., Kohn R., Lions J. Editors, Springer Verlag, New York, pp. 78-96.
- Chakrabarty J., (1987), "Theory of Plasticity," McGraw-Hill, New York.
- Chhabildas L.C., and Asay J.R., (1979), "Rise-Time Measurements Of Shock Transitions In Aluminum, Copper, And Steel," *Journal of Applied Physics*, Vol.40/4, pp. 2749-2756.
- Cortes R., (1992a), "Dynamic Growth of Microvoids under Combined Hydrostatic and Deviatoric Stress," *International Journal of Structures*, Vol.29/13, pp. 1637-1645.
- Cortes R., (1992b), "The Growth of Microvoids Under Intense Dynamic Loading," *International Journal of Structures*, Vol.29/11, pp. 1339-1350.
- Cortes R. and Elices M., (1995), "Numerical Modeling of Ductile Spall Fracture," *International Journal of Impact Engineering*, Vol.16/2, pp. 237-251.
- Curran D. R. and Seaman L., (1987), "Dynamic Failure of Solids," *Physics Reports (Review Section of Physics Letters)*, Vol.147/5 & 6, pp. 253-388, 1987.
- Davison L. and Graham R. A., (1979), "Shock Compression of Solids," *Physics Reports (Review Section of Physics Letters)*, Vol.55/4, pp. 256-379.

Doraivelu S. M., Gegel H. L., Gunasekera J. S., Malas J. C., Morgan J. T. and Thomas J. F. Jr., (1984), "A New Yield Function for Compressible P/M Materials," *International Journal of Mechanical Science*, Vol.26/9-10, pp. 527-535.

Eftis J. and Nemes J. A., (1991a), "Constitutive Modeling of Spall Fracture," *Archives of Mechanics, (Warszawa)*, Vol. 43/2-3, pp. 399-435.

Eftis J. and Nemes J. A., (1991b), "Evolution Equation for the Void Volume Growth Rate in a Viscoplastic-Damage Constitutive Model," *International Journal of Plasticity*, Vol. 7, pp. 275-293.

Eftis J. and Nemes J. A., (1991c), "Evolution Equation for the Void Volume Growth Rate for a Viscoplastic-Damage Constitutive Model," *International Journal of Plasticity*, Vol.7.

Eftis J., Nemes J. A. and Randles P. W., (1991d), "Viscoplastic Analysis of Plate-Impact Spallation," *International Journal of Plasticity*, Vol.7, pp. 15-39.

Eftis J. and Nemes J. A., (1992), "Modeling Of Impact-Induced Spall Fracture And Post Spall Behavior Of A Circular Plate," *International Journal of Fracture*, Vol.53, pp. 301-324.

Eftis J. and Nemes J. A., (1994), "Viscoplastic-Microdamage Constitutive Modeling of Dynamic Fracture," in *Localized Damage III*, pp. 589-597, Eds., Aliabadi M. H. *et al.*, Computational Mechanics Publications, Boston.

Eftis J. and Nemes J. A., (1995), "Modeling Dynamic Fracture of Plates and Tension Bars," in *Computational mechanics '95*, Vol. 1, pp. 1176-1181, Eds. Alturi S. N. *et al.*, Springer, New York.

Eftis J. and Nemes J. A., (1996), "On the propagation of Elastic-Viscoplastic Waves in Damaged-Softened Polycrystalline Materials," *International Journal of Plasticity*, Vol. 10/9, pp. 1005-1022.

Eftis J., (1996), "Constitutive Modeling of Spall Fracture," *High-Pressure Shock Compression of Solids II (Chapter 15)*, Davison L., Grady D. E. and Mohsen Shahinpoor (Editors), Springer-Verlag, pp. 399-451.

Ferreyra E., Murr L. E. and Horz F., (1995), "A Preliminary Study of the Effect of Target Microstructure on High-Velocity Impact Cratering in Thick Copper Plates," *Matallurgical and Materials Applications of Shock-Wave and High-Strain-Rate Phenomena (37)*, Murr L. E., Staudhammer K. P. and Meyers M. A. (Editors), Elsevier Science, pp. 303-312.

Ferreyra E., Murr L. E., Garcia E. P. and Horz F., (1997), "Effect Of Initial Microstructure On High Velocity And Hypervelocity Impact Cratering And Crater-Related Microstructures In Thick Copper Targets: Part I Soda Lime Glass Projectiles," *Journal of Materials Science*, Vol.32, pp. 2573-2585.

Follansbee P. S. and Kocks U. F., (1988), "A Constitutive Description of the Deformation of Copper Based on the Use of the Mechanical Threshold Stress as an Internal State Variable," *Acta Metallica*, Vol.36/1, pp. 81-93.

Froeschner K. E., (1989), "Spall Due To Short High-Intensity Impulses," *Journal of Applied Physics*, Vol.65/8, pp. 2964-2973.

Ghosh S. and Kikuchi N., (1991), "An Arbitrary Lagrangian-Eulerian Finite Element Method for Large Deformation Analysis of Elastic-Viscoplastic Solids," *Computer Methods in Applied Mechanics and Engineering*, 86, pp.127-188, North-Holland.

Gilath I., Eliezer S. and Gazit Y., (1991), "Fracture Modes In Alumina At Hypervelocity Impact Conditions," *Journal of Materials Science*, Vol. 26, pp. 2023-2025.

Godwal B. K., Sikka S. K. and Chidambaram R., (1983), "Equation of State Theories of Condensed Matter up to About 10 TPa," *Physics Reports (Review Section of Physics Letters)*, Vol.102/3, pp.122-197.

Grady D. E. and Asay J. R., (1982), "Calculation Of Thermal Trapping In Shock Deformation Of Aluminum," *Journal of Applied Physics*, Vol.53/11, pp. 7350-7354.

Grady D. E. and Kipp M. E., (1993), "Dynamic Fracture and Fragmentation," *High-Pressure Shock Compression of Solids (Chapter 8)*, James R. Asay and Mohsen Shahinpoor (Editors), Springer-Verlag.

Grady D. E. and Passman S. L., (1990), "Stability and Fragmentation of Ejecta in Hypervelocity Impact," *International Journal of Impact Engineering*, Vol.10, pp. 197-212.

Grady D. E., (1985), "Mechanisms of Dynamic Fragmentation: Factors Governing Fragment Size," *Mechanics of Materials*, Vol.4, pp. 311-320.

Grady D. E., (1988), "The Spall Strength of Condensed Matter," *Journal of Mechanical Physics in Solids*, Vol. 36/3, pp. 353-384.

Gray III G. T., (1993), "Influence of Shock-Wave Deformation on the Structure/Property Behavior of Materials," *High-Pressure Shock Compression of Solids (Chapter 6)*, James R. Asay and Mohsen Shahinpoor (Editors), Springer-Verlag.

- Gurson A. L., (1977), "Continuum Theory of Ductile Fracture by Void Nucleation and Growth: Part I - Yield Criteria and Flow Rules for Porous Ductile Media," *Transactions ASME* 2.
- Hancock J. W. and Thomson R. D., (1985), "Strain And Stress Concentration In Ductile Fracture Of Void Nucleation Growth And Coalescence," *Materials Science and Technology*, Vol.1, pp. 684-670.
- Herrmann W., (1969a), "Nonlinear Stress Waves in Metals," in *Wave Propagation in Solids*, Ed. Miklowitz J., ASME, pp. 129-183, New York.
- Herrmann W., (1969b), "Constitutive Equation for the Dynamic Compaction of Ductile Porous Materials," *Journal of Applied Physics*, Vol.40/6, pp. 2490-2499.
- Herrmann W. and Wilbeck J. S., (1987), "Review of Hypervelocity Penetration Theories," *International Journal of Impact Engineering*, Vol. 5, pp. 307-322.
- Holian K. S. and Burkett M. W., (1987), "Sensitivity of Hypervelocity Impact Simulations to Equation of State," *International Journal of Impact Engineering*, Vol.5, pp. 333-341.
- Horz F., Bernhard R. P. and See T. H., (1995), "Hypervelocity Penetration In Aluminum 6061 And 1100 Alloys," *Matallurgical and Materials Applications of Shock-Wave and High-Strain-Rate Phenomena (34)*, Murr L. E., Staudhammer K. P. and Meyers M. A. (Editors), Elsevier Science, pp. 273-283.
- Huntington H. B., (1958), "The Elastic Constants of Crystals," Academic Press, New York.
- Johnson G. R. and Cook W. H., (1983), "A Constitutive Model for Metals Subjected to Large Strain, High Strain Rates and High Temperatures," Presented at the *Seventh International Symposium on Ballistics*, The Hague, The Netherlands.
- Johnson G. R. and Holmquist T. J., (1988), "Evaluation Of Cylinder-Impact Test Data For Constitutive Model Constants," *Journal of Applied Physics*, Vol.64/8, pp. 3901-3910.
- Johnson G. R. and Stryk R. A., (1987), "Eroding Interface and Improved Tetrahedral Element Algorithms for High-Velocity Impact Computations in Three Dimensions," *International Journal of Impact Engineering*, Vol. 5, pp. 411-421.
- Johnson G. R., Stryk R. A., Holmquist T. J. and Souka O. A., (1990), "Recent EPIC Code Developments for High Velocity Impact: 3D Element Arrangements and 2D Fragment Distribution," *International Journal of Impact Engineering*, Vol.10, pp. 281-294.

- Johnson J. N., (1981), "Dynamic Fracture And Spallation In Ductile Solids," *Journal of Applied Physics*, Vol.52/4, pp. 2812-2825.
- Johnson J. N., Lomdahl P. S. and Wills J. M., (1991), "Analysis of Internal Stress and Anelasticity in the Shock Compressed State from Unloading Wave Data," *Acta Metallurgica et Materialia*, Vol. 39/12, pp. 3015-3026.
- Johnson W. E. and Anderson C. E., (1987), "History and Application of Hydrocodes in Hypervelocity Impact," *International Journal of Impact Engineering*, Vol.5, pp. 423-439.
- Kanel G. I., Razorenov S. V., Bogatch A., Utkin V., Fortov V. E. and Grady D. E., (1996), "Spall Fracture Properties Of Aluminum And Magnesium At High Temperatures," *Journal of Applied Physics*, Vol.79/11, pp. 8310-8317.
- Kanel G. I., Razorenov S. V., Bogatch A., Utkin V. and Grady D. E., (1997), "Simulation of Spall Fracture of Aluminum and Magnesium Over a Wide Range of Load Duration and Temperature," *International Journal of Impact Engineering*, Vol.20, pp. 467-478.
- Kim K. T. and Carroll M. M., (1987), "Compaction Equations for Strain Hardening Porous Materials," *International Journal of Plasticity*, Vol.3, pp.63-73.
- Kim K. T., (1988), "Elastic-Plastic Response of Porous Metals Under Triaxial Loading," *International Journal of Structures*, Vol.24/9, pp. 937-945.
- Kipp M. E. and Grady D. E., (1985), "Dynamic Fracture and Interaction in One Dimension," *Journal of Mechanical Physics in Solids*, Vol. 33/4, pp. 399-415.
- Kipp M. E., Grady D. E. and Swegle J. W., (1993), "Experimental and Numerical Studies of High Velocity Impact Fragmentation," *Sandia Report*, SAND93-0773.
- Koplink J. and Needleman A., (1988), "Void Growth and Coalescence in Porous Plastic Solids," *International Journal of Solids Structures*, Vol. 24/8, pp. 835-853.
- Kratochvil J. and Dillon O. W. Jr., (1969), "Thermodynamics of Elastic-Plastic Materials as a Theory with Internal State Variables," *Journal of Applied Physics*, Vol.40/8, pp. 3207-3218.
- Kratochvil J. and Dillon O. W. Jr., (1970), "Thermodynamics of Crystalline Elastic-Visco-Plastic Materials," *Journal of Applied Physics*, Vol.41/4, pp. 1470-1479.
- Lakkad S. C., (1971), "Temperature Dependence of the Elastic Constants," *Journal of Applied Physics*, Vol. 42/11, pp. 4277-4281.

Lee J. H. and Zhang Y., (1994), "A Finite-Element Work-Hardening Plasticity Model of the Uniaxial Compression and Subsequent Failure of Porous Cylinders Including Effects of Void Nucleation and Growth-Part I: Plastic Flow and Damage," *Journal of Engineering Materials and Technology*, Vol.116, pp. 69-79.

Lee J. H. and Zhang Y., (1996), "A Finite-Element Work-Hardening Plasticity Model of the Uniaxial Compression and Subsequent Failure of Porous Cylinders Including Effects of Void Nucleation and Growth-Part II: Localization and Fracture Criteria." *Journal of Engineering Materials and Technology*, Vol.118, pp. 169-178.

Lipkin J. and Asay J. R., (1977), "Reshock and Release of Shocked Compressed 6061-T6 Aluminum," *Journal of Applied Physics*, Vol. 48/1, pp. 182-189.

Liu W. K., Belytschko T. and Chang H., (1986), "An Arbitrary Lagrangian-Eulerian Finite Element Method for Path-Dependent Materials," *Computer Methods in Applied Mechanics and Engineering*, Vol.58, pp.227-245, North-Holland.

Mackenzie J. K., (1950), "The Elastic Constants of a Solid Containing Spherical Holes", *Proceedings of the Physical Society*, 63B, pp. 2-11.

Malvern L. E., (1969), "Introduction to the Mechanics of a Continuous Medium," *Series in Engineering of Physical Science*, Prentice-Hall.

McClintock F. A., (1968), "A Criterion for Ductile Fracture by the Growth of Holes." *Journal of Applied Mechanics*, pp. 363-371.

McGlaun J. M. and Yarrington P., (1993), "Large Deformation Wave Codes", *High-Pressure Shock Compression of Solids (Chapter 9)*, James R. Asay and Mohsen Shahinpoor (Editors), Springer-Verlag.

McGlaun J. M., Thompson S. L. and Elrick M. G., (1990), "CTH: A Three-Dimensional Shock Wave Physics Code," *International Journal of Impact Engineering*, Vol.10, pp. 351-360.

McQueen R. G. and Marsh S. P., (1960), "Equations Of State For Nineteen Metallic Elements From Shock-Wave Measurements To Two Megabars," *Journal of Applied Physics*, Vol. 31, pp. 1253-1268.

Meyers M. A. and Murr L. E., (1981), "Defect Generation in Shock-Wave Deformation (30)", *Shock Waves and High-Strain-Rate Phenomena in Metals*, Plenum Publishing Co., New York, pp. 487-530.

Meyers M. A., (1994), "Dynamic Behavior of Materials," John Wiley & Sons, Inc., New York.

Mineev V. N. and Mineev A. V., (1997), "Viscosity of Metals under Shock-Loading Conditions," *J. Phys IV France* 7, pp. c3-583-585.

Murr L. E. and Rivas J. M., (1994), "Measuring Hypervelocity Impact from Micrometeoroid Crater Geometry," *International Journal of Impact Engineering*, Vol.15/6, pp. 785-795.

Murr L. E., Ferreyra E., Pappu S., Garcia E. P., Sanchez J. C., Huang W., Rivas J. M., Kennedy C., Ayala A. and Niou C. S., (1996), "Novel Deformation Processes and Microstructures Involving Ballistic Penetrator Formation and Hypervelocity Impact and Penetration Phenomena," *Materials Characterization*, Vol.37, pp. 245-276.

Murr L. E., Niou C. S., Ferreyra E., Garcia E. P., Liu G., Horz F. and Bernhard R. P., (1997), "Effect Of Initial Microstructure On High Velocity And Hypervelocity Impact Cratering And Crater-Related Microstructures In Thick Copper Targets: Part II Stainless Steel Projectiles," *Journal of Materials Science*, Vol.32, pp. 3143-3156.

Nemat-Nasser S. and Hori M., (1987), "Void Collapse And Void Growth In Crystalline Solids," *Journal of Applied Physics*, Vol.62/7, pp. 2746-2756.

Nemes J. A. and Eftis J., (1989), "Low Angle Oblique Impact Spall Fracture Using Viscoplastic Constitutive Theory," *Advances in Constitutive Laws for Engineering materials*, Vol. II, pp. 633-639, Eds. Jinghong F. and Murakami S., International Academic Publishers, Beijing.

Nemes J. A. and Eftis J., (1990), "Use of Viscoplastic Constitutive Theory for Simulating Spallation Thresholds," *Shock Compression of Condensed Matter*, Schmidt S. S., Johnson J. N. and Davison L. (Editors), Elsevier Science Publications.

Nemes J. A. and Eftis J., (1991), "Several Features of a Viscoplastic Study of Plate-Impact Spallation with Multidimensional Strain," *Computers and Structures*, Vol. 38, pp. 317-328.

Nemes J. A. and Eftis J., (1992a), "Pressure-Shear Waves and Spall Fracture Described by a Viscoplastic-Damage Constitutive Model," *International Journal of Plasticity*, Vol.8, pp. 185-207.

Nemes J. A. and Eftis J., (1992b), "Rate Dependence of Multidimensional Plate Impact and Post Spall Behavior," in *Shock-Wave and High Strain-Rate Phenomena in Materials*, pp. 723-731, Eds. Meyers M., et al., Marcel Dekker, New York.

Nemes J. A. and Eftis J., (1993), "Constitutive Modeling of the Dynamic Fracture of Smooth Tensile Bars," *International Journal of Plasticity*, Vol. 9, pp. 243-270.

Nemes J. A., Eftis J. and Randles P. W., (1990), "Viscoplastic Constitutive Modeling of High Strain-Rate Deformation, Material Damage, and Spall Fracture," *Journal of Applied Mechanics*, Vol. 57/2, pp. 282-291.

Norris Jr. D. M., Reaugh J. E., Moran B. and Quiñones D. F., (1978), "A Plastic-Strain, Mean-Stress Criterion for Ductile Fracture," *Journal of Engineering Materials and Technology*, Vol. 100, pp. 279-286.

Oden J. T., Bhandari D. R., Yagawa G. and Chung T. J., (1973), "A New Approach to the Finite-Element Formulation and Solution of a Class of Problems in Coupled Thermoelastoviscoplasticity of Crystalline Solids," *Nuclear Engineering and Design*, Vol.24, pp. 420-430.

Ortiz M. and Molinari A., (1992), "Effect of Strain Hardening and Rate Sensitivity on the Dynamic Growth of a Void in a Plastic Material," *Journal of Applied Mechanics*, Vol.59, pp. 48-53.

Pardoen T. and Delannay F., (1998), "Assessment of Void Growth Models from Porosity Measurements in Cold-Drawn Copper Bars," *Metallurgical and Materials Transactions*, Vol.29A, pp. 1895-1909.

Perzyna P., (1986), "Internal State Variable Description of Dynamic Fracture of Ductile Solids," *International Journal of Solids Structures*, Vol.22/7, pp. 797-818.

Predebon W. W., Anderson Jr. C. E. and Walker J. D., (1991), "Inclusion Of Evolutionary Damage Measures In Eulerian Wavecodes", *Computational Mechanics*, vol.7.

Quiñones S. A., (1996), "Microstructural Characterization of Low-Velocity and Hypervelocity Impact Crater Cross-Sections in OFHC Copper Targets," Dissertation, Materials Science and Engineering Department, University of Texas at El Paso.

Quiñones S. A. and Murr L. E., (1998), "Correlation of Computed Simulations with Residual Hardness Mappings and Microstructural Observations of High Velocity and Hypervelocity Impact Craters in Copper," *Phys. Stat. Sol.*, Vol 166, pp. 763-789.

Rajendran A. M., Dietenberger M. A. and Grove D. J., (1989), "A Void Growth-Based Failure Model To Describe Spallation," *Journal of Applied Physics*, Vol.65/4, pp. 1521-1527.

- Rivas J. M., Quiñones S. A., Garcia E. P. and Murr L. E., (1995), "Microstructural Evolution Associated with Hypervelocity Impact Crater Formation in Metallic Targets." *Matallurgical and Materials Applications of Shock-Wave and High-Strain-Rate Phenomena*, (38) Murr L. E., Staudhammer K. P. and Meyers M. A. (Editors), Elsevier Science, pp. 313-323.
- Rubin, M. B., (1987), "An Elastic-Viscoplastic Model for Metals Subjected to High Compression," *Trans. ASME, Journal of Applied Mechanics*, Vol. 54, pp. 532-538.
- Rule W. K. and Jones S. E., (1998), "A Revised form for the Johnson-Cook Strength Model," *International Journal of Impact Engineering*, Vol. 21/8, pp. 609-624.
- Seaman L., Curran D. R. and Shockey D. A., (1976), "Computational Models For Ductile And Brittle Fracture," *Journal of Applied Physics*, Vol.47/11, pp. 4814-4826.
- Shima S. and Oyane M., (1976), "Plasticity Theory for Porous Metals," *International Journal of Mechanical Science*, Vol.18, pp. 285-291.
- Shockey D. A., Seaman L. and Curran D. R., (1979), "Microfailure Models and Their Application to Nonlinear Dynamic Fracture Problems," *Nonlinear and Dynamic Fracture Mechanics, ASME, AMD*, Vol. 35, pp. 79-104.
- Steinberg D. J. and Lund C. M., (1989), "A Constitutive Model For Strain Rates From 10⁻⁴ To 10⁶ S⁻¹," *Journal of Applied Physics*, Vol.65/4, pp. 1528-1533.
- Steinberg D. J., Cochran S. G. and Guinan M. W., (1980), "A Constitutive Model For Metals Applicable At High-Strain Rate", *Journal of Applied Physics*, Vol.51/3, pp. 1498-1504.
- Swegle J. W. and Grady D. E., (1985), "Shock Viscosity And The Prediction Of Shock Wave Rise Times", *Journal of Applied Physics*, Vol.58/2, pp. 692-701.
- Taylor E. A., Tsembelis K., Hayhurst C. J., Kay L. and Burchell M. J., (1999), "Hydrocode Modeling of Hypervelocity Impact on Brittle Materials: Depth of Penetration and Conchoidal Diameter," *International Journal of Impact Engineering*, Vol. 23, pp.895-904.
- Tongs W. and Ravichandran, (1993), "Dynamic Pore Collapse in Viscoplastic Materials," *Journal of Applied Physics*, Vol. 74/4, pp. 2425-2435.
- Tong W. and Ravichandran G., (1995), "Inertial Effects on Void Growth in Porous Viscoplastic Materials," *Journal of Applied Mechanics*, Vol.62, pp. 633-639.

Tonks D. L., (1989), "Rate-Dependent Plasticity Of Copper And Stainless Steel Under Shock Compression," *Journal of Applied Physics*, Vol.66/5, pp. 1951-1989.

Tonks D. L., (1991), "Model For The Relation Between Shock Velocity And Particle Velocity In Weak Shock Waves In Metals," *Journal of Applied Physics*, Vol.70/8. pp. 4238-4247.

Trucano T. G. and McGlaun J. K., (1990), "Hypervelocity Impact Calculations Using CTH: Case Studies," *International Journal of Impact Engineering*, Vol.10, pp. 601-613.

Tvergaard V. and Needleman A., (1984), "Analysis of the Cup-Cone Fracture in a Round Tensile Bar," *Acta Metallica*, Vol32/1, pp. 157-169.

Tvergaard V. and Needleman A., (1986), "Effect of Material Rate Sensitivity on Failure Modes in the Charpy V-Notch Test," *Journal of Mechanical Physics in Solids*, Vol.34/3, pp. 213-241.

Tvergaard V., (1982), "Ductile Fracture by Cavity Nucleation Between Larger Voids," *Journal of Mechanical Physics in Solids*, Vol.30/4, pp. 265-286.

Tvergaard V., (1987), "Effect of Yield Surface Curvature and Void Nucleation on Plastic Flow Localization," *Journal of Mechanical Physics in Solids*, Vol.35/1, pp. 43-60.

Tvergaard V., (1996), "Effect of Void Size Difference on Growth and Cavitation Instabilities," *Journal of Mechanical Physics of Solids*, Vol.44/8, pp. 1237-1253.

Walsh J. M., Rice M. H., McQueen R. G. and Yarger F. L., (1957), "Shock-Wave Compressions of Twenty-Seven Metals. Equation of State of Metals," *Physical Review*, Vol.108/2, pp. 196-216.

Wang W. M., Sluys L. J. and Borst R. D., (1997), "Viscoplasticity for Instabilities Due to Strain Softening and Strain-Rate Softening," *International Journal for Numerical Methods in Engineering*, Vol.40, pp. 3839-3864.

Wilkins M. L. and Guinan M. W., (1973), "Impact Of Cylinders On A Rigid Boundary," *Journal of Applied Physics*, Vol.44/3, pp. 1200-1206.

Wilkins M. L., Blum R. E., Cronshagen E. and Grantham P., (1974), "A Method for Computer Simulation of Problems in Solid Mechanics and Gas Dynamics in Three Dimensions and Time," Lawrence Livermore Laboratory, Report UCRL-51574.

Wilkins M. L., Streit R. D. and Reaugh J. E., (1980), "Cumulative-Strain-Damage Model of Ductile Fracture: Simulation and Prediction of Engineering Fracture Tests," Lawrence Livermore Laboratory, Report UCRL-53058.

Wilkinson D. S. and Caceres C. H., (1986), "Mechanism Of Plastic Void Growth During Superplastic Flow", *Materials Science and Technology*, Vol 2, pp. 1086-1092.

Worswick M. J. and Pick R. J., (1991), "Void Growth in Plastically Deformed Free-Cutting Brass," *Journal of Applied Mechanics*, Vol. 58, pp. 631-638.

Zerilli F. J. and Armstrong R. W., (1987), "Dislocation-Mechanics-Based Constitutive Relations For Material Dynamic Calculations," *Journal of Applied Physics*, Vol.61/5, pp. 1816-1825.

Zhou M. and Clode M. P., (1998), "Constitutive Equations For Modeling Flow Softening Due To Dynamic Recovery And Heat Generation During Plastic Deformation," *Mechanics of Materials*, Vol. 27, pp. 63-76.

Zurek A. K., Meyers M. A., (1996), "Microstructural Aspects of Dynamic Failure," *High-Pressure Shock Compression of Solids II (Chapter 2)*, Davison L., Grady D. E. and Mohsen Shahinpoor (Editors), Springer-Verlag, pp. 25-70.

CURRICULUM VITAE

Cesar Carrasco was born on October 11, 1966 in Cd. Juárez, México. The fifth son of Ariel Carrasco Almaraz and Socorro Trejo Acosta, he graduated from Colegio de Bachilleres, Plantel No. 5, Cd. Juárez, México in 1985 and entered the Instituto Tecnológico y de Estudios Superiores de Monterrey, México in the fall of 1985. In the Fall of 1989 he received his Bachelor of Science in Civil Engineering. In the summer of 1990 he entered the Graduate School at the University of Texas at El Paso receiving his Master of Science in Civil Engineering in the summer of 1992. In the summer of 1995 he entered the Graduate School at the University of Texas at El Paso. While pursuing a Doctoral degree in Materials Science and Engineering he worked at the FAST Center for Structural Integrity of Aerospace Systems at the University of Texas at El Paso as a full time research assistant. He is a member of the Golden Key National Honor Society. He was a guest speaker at the following conferences:

1. EXPLOMET 2000 International Conference on Fundamental Issues and Applications of Shock -Wave and High-Strain-Rate Phenomena, Albuquerque, NM, June 19-22, 2000.
2. SPIE's 1997 Smart Structures and Materials Symposium, San Diego, CA, March 3-6, 1997, and at the 15th International Modal Analysis Conference, Orlando Fl, Feb. 3-6, 1997.
3. 5th ASCE International Conference on Engineering, Construction, and Operations in Space - Space '96, Albuquerque, NM, Jun 1-6, 1996.
4. Meeting of the Working Group "Health Monitoring of Space Structures" NASA JSC, VAF, July 18, 1995.

5. 1991 Fall Meeting of the Texas Section ASCE, South Padre Island, Texas, Oct. 2-6, 1991.

With the following publications:

1. C. Carrasco, J. Eftis, and R. Osegueda, "Constitutive Modeling Of Spall-Fracture On 1100 Aluminum After Hypervelocity Impact," to be published in EXPLOMET 2000 International Conference on Fundamental Issues and Applications of Shock -Wave and High-Strain-Rate Phenomena, July 2000.
3. J. Eftis, C. Carrasco and R. Osegueda, "Modeling Dynamic Fracture Following High Shock Compression," to be published in Damage and Fracture Mechanics 2000, May 2000.
4. J. Eftis, C. Carrasco and R. Osegueda, "Elastic-Viscoplastic-Microdamage Modeling To Simulate Hypervelocity Projectile-Target Impact And Damage," to be published in IMPLAST 2000, Oct. 2000.
5. J. Eftis, C. Carrasco and R. Osegueda, "Constitutive Model Simulation of High Shock Compression, Micro-Damage Evolution and Fracture Associated with Hypervelocity Impact," MESO Mechanics 2000, Editor Sih G.C., Vol.1, pp.279-290, Tsinghua University Press, China, 2000.
6. L. R. Pereyra, R. A. Osegueda, C. Carrasco and C. Ferregut, "Detection of Damage in a Stiffened Plate from Fusion of Modal Strain Energy Differences," to be published in IMAC 2000, Feb. 2000.
7. R. A. Osegueda, G. Andre, C. Carrasco, C. M. Ferregut and L. Pereyra , "Effects of Mode Pairing in Strain Energy-Based Damage Detection Methods Applied to an Aerospace Structure," to be published in IMAC 2000, Feb. 2000.
8. Warke, R. W., Wang, Y.-Y., Ferregut, C. M., Carrasco, C. J. and Horsley, D. J., "A FAD-Based Method for Probabilistic Flaw Assessment of Strength-Mismatched Girth Welds," Proceedings of the 1999 Pressure Vessels and Piping Conference, PVP-Vol. 386, Probabilistic and Environmental Aspects of Fracture and Fatigue, ASME, 1999
9. R.A. Osegueda, A. Garcia-Diaz, S. Ashur, O. Melchor, S.-H. Chang, C. Carrasco, A. Kuyumcu, "GIS-Based Network Routing Procedures for Overweight Oversized Vehicles," Journal of Transportation Engineering, Vol. 125, No. 4, July/August 1999, pp. 324-331.

10. Pereyra, L.R., Osegueda, R.A., Carrasco, C. and Ferregut, C., "Damage Detection in a Stiffened-Plate Using Modal Strain Energy Differences," in *Nondestructive Evaluation of Aging Aircraft, Airports and Aerospace Hardware III*, Ed. A. K. Mal, Proceedings of SPIE, Vol. 3586, Paper 3586-29, March 1999.
11. Pereyra, L.R., Osegueda, R.A., Carrasco, C., Ferregut, C. M., "Structural Defects Detection Using Low Frequency Modal Testing with a Laser Vibrometer," In *Proc. ASNT Fall 1998 Conference, The American Society of Nondestructive Testing*, Columbus, OH, Oct. 1998, pp 63-66.
12. Ashur, S., Melchor-Lucero, O., Osegueda, R., Carrasco, C., Garcia-Diaz, A., and Chang, S-H., "A GIS Approach to Manage Routing of Oversize and Overweight Vehicles in Texas," in *Proc. of First Int. Conf. on New Information Technologies for Decision Making in Civil Engineering*, Montreal, Canada, Oct. 11-13, 1998, pp. 613-624.
13. Andre, G.C., Carrasco C.J., Osegueda, R.A., Ferregut, C. M., James III, G.H. and Grygier, M., "Comparison of Accelerometer and Laser Modal Tests of a Vertical Stabilizer Assembly," *SPACE 98, ASCE*, April 1998, pp.132-139.
14. Carrasco, C., Osegueda, R., and Ferregut, C. "Localización y Cuantificación de Daños en una Estructura Tridimensional Usando la Energía de Deformación Modal," *Memoria del XI Congreso Nacional de Ingeniería Sísmica, Volumen II*, Veracruz, México, Noviembre 26-29, 1997, pp. 851-860. (In Spanish)
15. Meza, Jr., R., Carrasco, C. J., Osegueda, R. A., James III, G. and Robinson, N. A., "Damage Detection in a DC-9 Fuselage Using Laser Doppler Velocimetry Measurements," *Proceedings of the SPIE's 1997 Smart Structures and Materials Symposium*, San Diego, CA, March 3-6, 1997.
16. Perez, L. E., Ferregut, C. M., Carrasco, C. J., Paez, T. L., Barney, P. and Hunter, N. F., "Statistical Validation of a Plate Finite-Element Model for Damage Detection," *Proceedings of the SPIE's 1997 Smart Structures and Materials Symposium*, San Diego, CA, March 3-6, 1997.
17. Carrasco, C. J., Osegueda, R. A., Ferregut, C. M. and Grygier, M., "Damage Localization in a Space Truss Model Using Modal Strain Energy," *Proceedings of the 15th International Modal Analysis Conference*, Orlando FL, Feb. 3-6, 1997. Pg. 1786-1792

18. Osegueda, R. A., Carrasco, C. J., and Meza, Jr., R., "A Modal Strain Energy Distribution Method to Localize and Quantify Damage," Proceedings of the 15th International Modal Analysis Conference, Orlando Fl, Feb. 3-6, 1997. Pg. 1298-1304
19. Meza, Jr., R., Carrasco, C. J., Osegueda, R. A., James III, G. and Robinson, N. A., "Damage Detection in a DC-9 Fuselage Using Laser Doppler Velocimetry," Proceedings of the 15th International Modal Analysis Conference, Orlando, Fl, Feb. 3-6, 1997. Pg. 1779-1785
20. Carrasco, C. J., Osegueda, R. A. and Ferregut, C. M., "Modal Tests of a Space Truss Model and Damage Localization Using Modal Strain Energy," Report FAST 96-01, Jul. 1996, FAST Center for Structural Integrity of Aerospace Systems, The University of Texas at El Paso, El Paso, Texas 79968.
21. Meza, Jr. R., Carrasco, C. J., Osegueda, James III, G. and Robinson, N. A., "Modal Tests of Composite Honeycomb Panels Using Laser Doppler Velocimetry for Damage Assessment," Report FAST 96-02, Sep. 1996, FAST Center for Structural Integrity of Aerospace Systems, The University of Texas at El Paso, El Paso, Texas 79968.
22. Carrasco, C. J., Osegueda, R. A., Ferregut, C. M., Harms, B., Meza, D. and Grygier, M., "Comprehensive Modal Tests of a Space Truss Model for Damage Assessment," Proceedings of the 5th ASCE International Conference on Engineering, Construction, and Operations in Space - Space '96, Albuquerque, NM, Jun 1-6, 1996, pg. 1141-1147
23. Osegueda, R.A., Carrasco, C. J., Sanchez, A. and Siddappa, N., "Effects of Structural Damage on the Vibrational Mode Shapes Measured with Laser Interferometry," Texas Civil Engineer, Texas Section ASCE, Aug/Sept 1991.

Permanent address: 12070 Village Gate Dr.
El Paso, Texas, 79936

This dissertation was typed by Cesar Carrasco.